Optical Properties and Optoelectronic Applications of Nano-size Metallic Films and Metamaterials

by

Cheng Zhang

A dissertation submitted in partial fulfillment
of the requirements for the degree of
Doctor of Philosophy
(Electrical Engineering)
in the University of Michigan
2016

Doctoral Committee:

Professor L. Jay Guo, Chair
Associate Professor Anthony Grbic
Assistant Professor Xiaogan Liang
Professor Theodore B. Norris

To my father Cantao Zhang, and my mother Jing Zhou

For their love, support, and dedication

ACKNOWLEDGEMENTS

First of all, I would like to express my sincere gratitude to my PhD advisor: Professor L. Jay Guo, who I started to work with since the summer of 2011. His passion for research and positive attitude are extremely contagious. Professor Guo has been providing me invaluable guidance and support along my PhD study, and have taught me various things, including research methodologies, effective writing, presentation skills, etc. He has always been willing to give me great freedom to explore new ideas, and offer plenty of opportunities for both internal and external collaborations. I am indebted to him for training me as an independent researcher.

I would like to express my sincere gratitude to my other committee members: Professor Anthony Grbic, Professor Ted Norris, and Professor Xiaogan Liang. I appreciate the close collaboration with Professor Grbic on metasurfaces and metamaterials. Also, I would like to thank Professor Norris for the collaboration on real-time THz sensing. Besides, I would like to thank Professor Liang for stimulating discussions on various research topics. In addition, I have taken several courses from them, which provided the foundation that made this thesis possible. What is more, they have kindly helped me write reference letters for several scholarship and job applications.

I would like to thank my colleagues and friends in my research group, Center for Photonic and Multiscale Nanomaterials (CPHOM), Center for Ultrafast Optical Science (CUOS),

The Optical Society at the University of Michigan (OSUM), and Department of Electrical Engineering and Computer Science (EECS) for their support and insightful discussions. I would like to give sincere gratitude to my mentors in Professor Guo's lab: Dr. Tao Ling, Dr. Sung-Liang Chen, and Dr. Yi-Kuei Wu for kindly passing on their research expertise without any reservation. I would like to express my sincere gratitude to various collaborators within my group: I would like to thank Dr. Tao Ling, Dr. Sung-Liang Chen, and Mr. Qiaochu Li for the collaboration on optical ultrasound detectors and photoacoustic imaging; I would like to thank Dr. Yi-Kuei Wu and Mr. Andrew Hollowell for the collaboration on structural color filters; I would like to thank Dr. Dewei Zhao, Dr. Deen Gu, Mr. Hyunsoo kim, Mr. Chengang Ji, Ms. Qingyu Huang, Mr. Zhan Liu, and Mr. Tom George for the collaboration on thin doped Ag films; I would like to thank Mr. Long Chen for the collaboration on hyperbolic metamaterials; I would like to thank Ms. Xi Chen for the collaboration on plasmonic lithography; I would like to thank Dr. Taehee Jang for the collaboration on the stretchable antennas. In addition, I would also like to express my gratitude to other former and current lab-mates: Dr. Ting Xu, Dr. Jing Zhou, Dr. Jinbao Guo, Dr. Yang Yang, Dr. Fan Yang, Dr. Hui Joon Park, Dr. Moon Kyu Kwak, Dr. Hongseok Youn, Dr. Jong G. Ok, Dr. Hyoung Won Baac, Dr. Young Jae Shin, Dr. Alex Kaplan, Dr. Jae Yong Lee, Dr. Kyu-Tae Lee, Dr. Taehwa Lee, Dr. Ashwin Panday, Dr. Wei Luo, Mr. Sangeon Lee, Mr. Suneel Joglekar, Mr. Qingyu Cui, Mr. Zhong Zhang, Mr. Lei Jin, Mr. Zheyang Zheng, Mr. Lei Wan, Mr. Gaofeng Liang for sharing their experiences and time with me.

I would like to express my sincere gratitude to my collaborators at the University of Michigan: I would like to thank Dr. Carl Pfeiffer and Dr. Vishva Ray for the fruitful collaboration on metasurfaces; I would like to thank Dr. You-Chia Chang and Dr. Momchil Mihnev for the collaboration on real-time THz sensing; I would like to thank Professor Xudong Fan, Mr. Kyu Hyun Kim, and Dr. Wei Luo for the collaboration on air-coupled ultrasound detectors; I would like to thank Professor Xueding Wang, Dr. Guan Xu, Dr. Zhixing Xie, and Dr. Chao Tian for the collaboration on photoacoustic imaging; I would like to thank the talented engineers at the Lurie Nanofabrication Facility (LNF) for their tremendous support.

Besides, I would like to express my sincere gratitude to collaborators in other universities and research institutes: I would like to thank Professor Ray Chen, Dr. Harish Subbaraman, and Mr. Zeyu Pan at the University of Texas-Austin for the collaboration on printed optical devices; I would like to thank Professor Vladimir Shalaev, Professor Alexandra Boltasseva, and Mr. Nathaniel Kinsey at Purdue University for the collaboration on plasmonic waveguides; I would like to thank Professor Nikolas Podraza, Mr. Junda Maxwell, and Mr. Prakash Uprety at the University of Toledo for metasurface measurements; I would like to thank Dr. Nina Hong at J.A. Woollam Co. for helpful ellipsometry discussions and measurements.

Last, but most importantly, I would like to express my deep appreciation to my parents and grandma for their constant encouragement, unconditional love, and unfailing support. I am truly blessed to have them in my life.

TABLE OF CONTENTS

DEDICATION ..... **ii**

ACKNOWLEDGEMENTS ..... **iii**

LIST OF FIGURES ..... **x**

LIST OF TABLES ..... **xx**

ABSTRACT ..... **xxi**

Chapter 1: Introduction **1**

1.1 Background 1

1.2 Thesis outline 3

Chapter 2: Ultra-thin, Smooth, Low-loss and Stable Al-doped Ag Films **9**

2.1 Introduction 9

2.2 Ultra-thin and smooth Ag films by Al doping 11

2.3 Optical properties of Al-doped Ag films 16

2.4 Significantly improved stabilities of Al-doped Ag films 18

2.5 Mechanism of ultra-thin Ag film formation 23

2.6 Alternative ultra-thin, smooth and low-loss doped Ag films 25

2.7 Conclusions 29

Chapter 3: Organic Solar Cells Using Al-doped Ag Films as Transparent Conductors **30**

3.1 Introduction 30

3.2 Optical and electrical characterizations of Al-doped Ag films 31

3.3 Organic Solar cells with Al-doped Ag films as transparent conductors 36

3.4 Conclusions 44

Chapter 4: Organic Solar Cells Using Al-doped Ag Films as Transparent Conductors: Improved Designs 45

4.1 Introduction 45

4.2 Ultra-thin Al-doped Ag films with Ta_2O_5 wetting layers 46

4.3 Resonant light harvesting with Ta_2O_5/Al-doped Ag electrodes 50

4.4 Highly transparent TiO_2/Al-doped Ag/TiO_2/MgF_2 electrode 62

4.5 Conclusions 65

Chapter 5: Organic Light Emitting Diodes Using Al-doped Ag Films as Transparent Conductors 67

5.1 Introduction 67

5.2 ITO-based devices 68

5.3 Ultra-thin doped Ag-based devices 71

5.4 Conclusions 73

Chapter 6: Nanophotonic Framework Enabled by Ultra-thin, Low-loss, and Stable Al-doped Ag Films 75

6.1 Introduction 75

6.2 Hyperbolic metamaterials based on Al-doped Ag films 77

6.3 Plasmonic interconnects based on Al-doped Ag films 84

6.4 Conclusions 88

Chapter 7: Highly Efficient, Broadband, and Angular Robust Asymmetric Light Transmitting Metasurface 89

7.1 Introduction 89

7.2 Design 91

7.3 Fabrication and characterization 99

7.4 Angular robustness and design tolerance 104

7.5 Conclusions 111

Chapter 8: Printed Metasurface 112

8.1 Introduction 112

8.2 Design 115

8.3 Fabrication and characterization 118

8.4 Conclusions 120

Chapter 9: Ultra-broadband and Highly Sensitive Opitcal Ultrasound Detector for Photoacoustic Imaging 122

9.1 Introduction 122

9.2 Device fabrication and characterization 125

9.3 Ultrahigh axial resolution 131

9.4 Theoretical analysis of the frequency response 134

9.5 Real time THz pulse detection 137

9.6 Conclusions 139

Chapter 10: Ultrasound Detectors Based on Polymer Filled Silicon Metasurfaces on Fiber Tips 141

10.1 Introduction 141

10.2 Design 142

10.3 Fabrication 146

10.4 Preliminary test 148

10.5 Conclusions 150

Chapter 11: Summary and Future Directions 151

11.1 Summary 151

11.2 Future directions 153

11.3 Contributions 155

Bibliography 157

LIST OF FIGURES

Figure 2.1: Schematic drawing of the Al and Ag co-sputter set-up..... 12

Figure 2.2: An annular bright field (ABF) cross-sectional transmission electron micrograph (TEM) of a 6 nm Al-doped Ag film. 13

Figure 2.3: SEM and AFM images of pure Ag and Al-doped Ag films..... 14

Figure 2.4: Transmission spectrum of a 9 nm (nominal thickness) pure Ag film.. 15

Figure 2.5: 3D tapping-mode AFM images of Al-doped Ag films. 16

Figure 2.6: (a) Schematic of ellipsometry measurement procedure using the interference enhancement method. (b) Thickness fitting uniqueness of a 6 nm Al-doped Ag film. 18

Figure 2.7: Stability of thin pure Ag and Al-doped Ag films at room temperature.. 19

Figure 2.8: Long-term stability of Al-doped Ag films.. 20

Figure 2.9: Thermal stability of pure Ag and Al-doped Ag films.. 21

Figure 2.10: Measured real and imaginary parts of permittivity of as-deposited Al-doped Ag films and films underwent an annealing treatment.. 22

Figure 2.11: XPS spectrum of Al-doped Ag films… 23

Figure 2.12: The 2D AFM images of (a) 3 nm pure Ag films and (b) 3 nm Al-doped Ag films.. 25

Figure 2.13: Permittivities of different doped Ag films with lower, optimized, and higher sputter powers of the doping metals.. 27

Figure 2.14: SEM pictures of a ~8 nm (a) Al-doped Ag film; (b) Ti-doped Ag film; (c) Cr-doped Ag film; (d) Cu-doped Ag film..... 28

Figure 2.15: XRD scans of a (a) 50 nm pure Ag film; (b) 50 nm Cr-doped Ag film; (c) 50 nm Cu-doped Ag film.. 29

Figure 3.1: Transmission spectra of (a) Al-doped Ag films and (b) Al-doped Ag/ZnO films with different thickness (6, 7, 9, and 11 nm), in which ITO and ITO/ZnO films are shown as well. Photos of (c) ITO/ZnO and (d) 7 nm Al-doped Ag/ZnO transparent conductors in front of a colored logo. (e) Sheet resistance versus the Al-doped Ag film thickness (black: Al-doped Ag film; red: Al-doped Ag/ZnO film; blue: Al-doped Ag film after annealing in N_2 environment). 34

Figure 3.2: (a) Reflection spectra of Al-doped Ag films and Al-doped Ag/ZnO films with different thicknesses (6, 7, 9, and 11 nm). (b) Comparison of optical transmittance (at 550 nm) versus sheet resistance for the Al-doped Ag/ZnO electrodes and other reported works. 35

Figure 3.3: The solar cell geometry using either an ITO or ultra-thin Al-doped Ag electrode. 36

Figure 3.4: (a) J-V characteristics of ITO based and ultra-thin Al-doped Ag based OPVs. (b) EQEs of ITO based and ultra-thin Al-doped Ag based OPVs. 39

Figure 3.5: (a) TAEs and EQEs of ITO and 7 nm Al-doped Ag based devices. (b) EQE and TAE enhancements of 7 nm Al-doped Ag based devices over ITO based ones, as well as the normalized absorption spectrum of the PBDTTT-C-T:PC70BM active layer and normalized photon density of the AM1.5G solar light. Simulation of the optical field intensity ($|E|^2$) distribution versus position and wavelength in (c) an ITO based device and (d) a 7 nm Al-doped Ag based device. 42

Figure 3.6: (a) Bendability test of the devices with PET/ITO and PET/Al-doped Ag as electrodes. (b) Sheet resistance of the Al-doped Ag film versus bending times. The inset shows a photo of Al-doped Ag film on a PET substrate..... 43

Figure 3.7: Dependence of the PCE of the device with an Al-doped Ag film as the electrode on the storage time. 44

Figure 4.1: SEM images of (a) Ta_2O_5/Al-doped Ag (4 nm), (b) Ta_2O_5/Al-doped Ag (5 nm), (c) Ta_2O_5/pure Ag (7 nm), and (d) AFM image of Ta_2O_5/Al-doped Ag (4 nm) with an RMS roughness of 0.76 nm..... 47

Figure 4.2: Tapping mode AFM images of (a) Ta_2O_5/Al-doped Ag (4 nm), (b) Ta_2O_5/Al-doped Ag (5 nm), (c) Ta_2O_5/Al-doped Ag (6 nm), and (d) Ta_2O_5/Al-doped Ag (7 nm), which all exhibit RMS roughness values less than 1 nm..... 48

Figure 4.3: Transmission spectra of (a) Ta_2O_5/Al-doped Ag (4, 5, 6, and 7 nm), (b) Ta_2O_5/Al-doped Ag (4, 5, 6, and 7 nm)/ZnO (40 nm).. 49

Figure 4.4: (a) J-V characteristic and (b) EQE spectrum of solar cells based on electrodes with Ta_2O_5/Al-doped Ag (4 nm).. 50

Figure 4.5: Transmission spectra of (a) Ta_2O_5 (x nm)/Al-doped Ag (7 nm) and (b) Ta_2O_5 (x nm)/Al-doped Ag (7 nm)/ZnO (40 nm) with varying thicknesses of the Ta_2O_5 layer. (c) Comparison of optical transmittance (at 550 nm) versus sheet resistance of Ta_2O_5/Al-doped Ag/ZnO electrode with other reported results based on Ag planar films/nanostructures. (d) Schematic of the OSC devices with Ta_2O_5/Al-doped Ag as the electrode. 52

Figure 4.6: (a) J-V characteristics and (b) EQE spectra of ITO and Ta_2O_5 (x nm)/Al-doped Ag (7 nm) electrode based OPVs. (c) EQE enhancement of Ta_2O_5 (5, 15, 20, 25,

30, and 50 nm)/Al-doped Ag (7 nm) based OPVs over ITO based ones. (d) Bendability test of the devices with PET/ITO and PET/Ta_2O_5 (15 nm)/Al-doped Ag (7 nm) as electrodes. 55

Figure 4.7: Simulation of the optical field intensity ($|E|^2$) distribution versus position and wavelength in (a) ITO based device, (b) Ta_2O_5 (15 nm)/Al-doped Ag (7 nm) based device, (c) Ta_2O_5 (5 nm)/Al-doped Ag (7 nm) based device, and (d) Ta_2O_5 (50 nm)/Al-doped Ag (7 nm) based device..... 58

Figure 4.8: (a) J-V characteristics and (b) EQE spectra of ITO and Ta_2O_5 (x nm)/Al-doped Ag (7 nm) electrode based OPVs with a thin PBDTTT-C-T:$PC_{70}BM$ layer (50 nm) 59

Figure 4.9: Simulation of the optical field intensity ($|E|^2$) distribution versus position and wavelength with varying Al-doped Ag electrode thicknesses at 4 nm (a), 7 nm (b), 10 nm (c), and 14 nm (d)..... 60

Figure 4.10: Simulated J_{sc} of OSC devices with varying thicknesses of the Al-doped Ag layer from 3 nm to 14 nm and fixed other layer thicknesses. 61

Figure 4.11: Transparent conductor based on Al-doped Ag films..... 64

Figure 4.12: The net phase accumulation of each dielectric layer in the DMD transparent conductor consisting of 50 nm TiO_2/7 nm Al-doped Ag/40 nm TiO_2/100 nm MgF_2..... 65

Figure 5.1: Schematic drawing of the OLED structure. 69

Figure 5.2: (a) Out-coupling efficiency of the ITO-based device with different thicknesses of the ZnO and PEDOT layers. (b) Energy distribution in all layers in the ITO-based device with an optimized out-coupling efficiency..... 70

Figure 5.3: (a) Out-coupling efficiency of the 10 nm Al-doped Ag-based device with different thicknesses of the ZnO and PEDOT layers. (b) Energy distribution in all layers in the Al-doped Ag-based device with an optimized out-coupling efficiency. 71
Figure 5.4: (a) Out-coupling efficiency of the 10 nm Cu-doped Ag-based device with different thicknesses of the ZnO and PEDOT layers. (b) Energy distribution in all layers in the Cu-doped Ag-based device with an optimized out-coupling efficiency..... 72
Figure 5.5: Optimized out-coupling efficiencies with different thin doped Ag film thicknesses for the Al-doped Ag- and Cu-doped Ag-based OLEDs 73
Figure 6.1: (a) Measured transmission efficiency from the fabricated HMM consisting of 4 period of 7 nm Al-doped Ag and 20 nm Ta_2O_5. (b) Dispersion curve of HMM at 700 nm. The HMM supports the propagation of modes with transverse wave-vectors larger than k_c. 78
Figure 6.2: Measured permittivities of the fabricated HMM..... 80
Figure 6.3: (a) Calculated transmission amplitude of an electromagnetic wave with different transverse wave-vectors (k_x) through a HMM made of 8 periods of 7 nm Al-doped Ag and 20 nm Ta_2O_5. (b) Calculated transmission amplitude of an electromagnetic wave with different transverse wave-vectors (k_x) through a HMM made of 4 periods of 14 nm Al-doped Ag and 40 nm Ta_2O_5..... 82
Figure 6.4: Calculated Purcell factor of a dipole emitter located 10 nm above two HMMs studied in figure 6.3a and 6.3b..... 82
Figure 6.5: LR-SPP waveguide based on Al-doped Ag.. 85
Figure 6.6: Measurement set-up to characterize the mode profile and propagation loss of the waveguide. 86

Figure 6.7: (a) Experimentally measured modal profile from the output facet of the Al-doped Ag LRSP waveguide. (b) Fitting of the vertical intensity with an exponential decay of the plasmonic mode. 86

Figure 6.8: Simulated mode size and propagation loss of 10 nm thick, Al-doped Ag strip waveguides with different strip widths (solid lines).. 87

Figure 7.1: Artistic rendering of the metasurface, consisting of three layers of cascaded Au nano-gratings. 92

Figure 7.2: Simulated transmission intensity through three layers of Au nano-gratings based on the Malus' law. 94

Figure 7.3: Simulated transmission intensity through the metasurface in the linear (a) and logarithmic (b) scale. 95

Figure 7.4: Calculated transmittance of the metasurface based on full-wave simulation of the structure (solid curves) and simulation of cascaded equivalent sheets. 96

Figure 7.5: Calculated transmittance of two orthogonal grating layers separated a SU8 spacer.. 97

Figure 7.6: (a) Metasurface fabrication flow chart; (b-d) SEM pictures of the bottom (b), middle (c) and top (d) layer. 100

Figure 7.7: (a-b) Measured transmission intensity from the metasurface in the linear (a) and logarithmic (b) scale; (c) Bright transmitted light pattern from one direction; (d) Blocked transmitted light pattern from the reverse direction.. 103

Figure 7.8: Measured T_{xy} and T_{yx} components with a broadband ellipsometer and large beam size..... 104

Figure 7.9: (a-b) Simulated transmittance at 1.5 µm with different values of angle of incidence in the XZ (a) and YZ (b) plane; (c-d) Measured transmittance with a 30° angle of incidence in the XZ (c) and YZ (d) plane. 105
Figure 7.10: Normal transmission and angular transmission intensity from a single grating layer, which shows good angular tolerance behavior. 106
Figure 7.11: (a) Simulated transmittance when the grating width is reduced by 10 nm (60 nm, 90 nm, and 60 nm for the bottom, middle, and top layers, respectively). (b) Simulated transmittance when the grating width is reduced by 20 nm (50 nm, 80 nm, and 50 nm for the bottom, middle, and top layers, respectively). (c) Simulated transmittance when the grating width is increased by 10 nm (80 nm, 110 nm, and 80 nm for the bottom, middle, and top layers, respectively). (d) Simulated transmittance when the grating width is increased by 20 nm (90 nm, 120 nm, and 90 nm for the bottom, middle, and top layers, respectively). 108
Figure 7.12: (a) Generalized model of the metasurface as coupled metallic sheets. (b) Simulated transmittance of metasurface with three layers of identical Au nano-gratings. 109
Figure 7.13: Adjusted transmittance of the metasurface by varying the nano-grating layer spacing. 110
Figure 7.14: (a) Simulated transmittance of the metasurface with a 70 nm spacer layer thickness. (b) Simulated transmittance of the metasurface with a 260 nm spacer layer thickness. 110

Figure 8.1: (a) Schematic drawing of the cross-sectional view of the Si metasurface. (b) Schematic drawing of a rotated Si nano-bar with a rotation angle according to its azimuthal position. 117
Figure 8.2: Schematic of the layout of the nano-antennas whose orientations are rotated gradually over the plane. 117
Figure 8.3: (a) Transmission intensities of the two modes through the 1D Si grating. (b) Transmission intensity difference of the two modes through the 1D Si grating. (c) Transmission phases of the two modes through the 1D Si grating. (d) Transmission phase difference of the two modes through the 1D Si grating 118
Figure 8.4: (a) a SEM picture of the imprinted Si metasurface. (b) An optical microscope picture of the device with a 1 mm x 1 mm area. 119
Figure 8.5: Measured transmission intensity through the metasurface with respect to different orientations of the polarizer transmission axis. 120
Figure 9.1: (a) Schematics of the polymer microring fabrication by the nano-imprinting lithography. (b) Optical transmission spectrum of the polymer microring resonator. (c) Angle view scanning electron microscope (SEM) of the microring with a diameter of 60μm. (d) Side view SEM picture of the ring with a height of 1.4μm. 127
Figure 9.2: (a) Experimental set-up to determine the bandwidth of the ring resonator. (b) Experimentally measured laser signal (FWHM=1.5 ns) and photoacoustic signal (FWHM=1.8 ns) in the time domain. (c) The microring response spectrum in the frequency domain. 130

Figure 9.3: (a) Contrast to noise ratio (CNR) as a function of the delay distance. (b) Photoacoustic signals of two closely spaced Cr films with 1.9 ns separation in time domain, which is a direct experimental demonstration of the super high axial resolution (2.85 um). 133
Figure 9.4: Ring frequency response spectrum and its Gaussian functional extrapolation, showing the detector -6 dB response at 470 MHz, and the detector FWHM bandwidth as 940 MHz. 133
Figure 9.5: (a) Simulated transverse electric (TE) mode distribution; (b) Comparison of simulated and measured frequency response. 136
Figure 9.6: (a) Experimental set-up of the PADTH system; (b) Detected photoacoustic signal from a signal THz pulse, signifying the system real-time response capability. (c) A THz image by PADTH system. 138
Figure 10.1: (a) Schematic drawing of the polymer filled silicon metasurface. (b) Reflection spectrum of the metasurface with a sharp resonance. 143
Figure 10.2: (a) Optical field distribution of a unit cell of the metasurface at resonance, and there is a significant optical field inside the SU8 polymer layer. The rectangular box denotes the position of the 1D Si grating. (b) Shift of the resonance wavelength with respect to the refractive index change of SU8. 144
Figure 10.3: (a) Reflection resonances for gratings with different widths. The grating period and height are fixed as 660 nm and 1035 nm, respectively. (b) Reflection resonances for gratings with different heights. The grating period and width are fixed as 660 nm and 365 nm, respectively. 145

Figure 10.4: Reflection resonance with different angles of incidence. The polarization of the incident light is fixed along the 1D grating direction. 146
Figure 10.5: Fabrication process of the metasurface membrane. 147
Figure 10.6: (a) SEM of the HCG after BHF etching. (b) SEM of the HCG after SU8 polymer filling. (c) Optical microscope picture of the SU8 filled HCG. 147
Figure 10.7: Fabrication process of transferring the metasurface membrane onto the tip of an optical fiber. 148
Figure 10.8: (a) An optical microscope picture of the metasurface membrane on the tip of an optical fiber. (b) Measured reflection spectrum of the device with a Q factor around 3000..... 149
Figure 10.9: (a) Schematic of ultrasound wave detection using the metasurface probe. (b) Measured acoustic waves..... 149

LIST OF TABLES

Table 3.1: Summary of the main photovoltaic parameters of the devices with ITO and Al-doped Ag films with different thicknesses as electrode..... 39

Table 4.1: Summary of performance metrics of the devices with ITO and Ta_2O_5/Al-doped Ag (7 nm) with varying thicknesses of Ta_2O_5 layer, which are obatined from 6 devices for each condition. 56

ABSTRACT

Optical Properties and Optoelectronic Applications of Nano-size Metallic Films and Metamaterials

Future optical and optoelectronic devices are desired to have compact sizes, high efficiencies, robust performance, and low manufacturing costs. All these advances demand developments both in their constituent materials and design concepts. Silver (Ag) is one of the most widely used materials for optoelectronic devices and metamaterials, due to its low optical loss in the visible and near infrared (NIR) range, as well as good electrical conductivity. However, Ag is well known to have several issues, including difficulty to form high-quality thin films, poor stability in an ambient environment and under elevated temperatures, and inferior adhesion with substrates. These issues constrain Ag's applications in various devices. In light of this, a new kind of silver: doped silver is developed. With the aid of a small amount of doping elements (e.g., Aluminum, Titanium, Chromium, and Copper) during the Ag deposition, ultra-thin (down to 6 nm), smooth (sub-ns roughness), and low-loss Ag films are obtained. Compared to pure Ag films, doped Ag films have a significantly improved long-term and thermal stability, as well as good adhesion to various substrates. For example, Al-doped Ag films have an improved thermal stability up to 500 ˚C, and are stable in ambient environment for over half a year. Doped Ag films have facilitated diverse high-performance optical and optoelectronic devices,

such as organic solar cells, organic light emitting diodes, optical metamaterials, and plasmonic devices.

Metamaterials are artificially designed materials with extraordinary optical properties, and have the potential to replace conventional bulky optical systems. Nano-size metamaterials (metasurfaces) are demonstrated for controlling various properties of light. An asymmetric light transmitting metasurface consisting of coupled metallic sheets is demonstrated. It has a measured transmission efficiency of 80%, extinction ratio of 13.8 dB around 1.5 μm, and a full width half maximum bandwidth of 1.7 μm. It is as thin as 290 nm, has a good performance tolerance against the angle of incidence and constituent nano-structure geometry variations. In addition, a large-area, printed metasurface is designed and fabricated. It is made of lossless dielectric (silicon) materials and offers the functionality of converting a linearly polarized incident light into a radially polarized transmitted light.

These optical and optoelectronic devices also provide valuable solutions to problems in other fields, such as acoustic wave detection. It is shown that optical resonant structures provide a unique approach for acoustic wave detection. Nanoimprinted polymer microring resonators are investigated as high-performance ultrasound detectors. They have a good detection sensitivity (noise equivalent detectable pressure of 105 Pa from 1 to 350 MHz), broad response bandwidth (DC to 350 MHz at -3dB), and immunity to electromagnetic interferences. These advantages have facilitated their various applications, such as photoacoustic imaging and real-time terahertz (THz) pulse detection. To further reduce the

detector size, polymer filled silicon metasurfaces on fiber tips are also designed and fabricated.

Chapter 1

Introduction

1.1 Background

Future optical and optoelectronic devices are desired to have compact sizes, high efficiencies, robust performance, and low manufacturing costs. All these advances call for developments both in their constituent materials and design concepts. This PhD thesis presents some of the recent developments of the above aspects.

Silver (Ag) is one of the most widely used materials for optoelectronic devices and metamaterials, due to its low optical loss in the visible and near infrared (NIR) range, as well as good electrical conductivity. However, Ag is well known to have several issues, including difficulty to form high-quality thin films, rough surface morphologies, poor stability in an ambient environment and under elevated temperatures, and inferior adhesion with substrates. These issues constrain Ag's applications in various devices. In light of this, a new kind of "improved" silver: doped silver is developed. With the aid of a small amount of doping elements (e.g., Aluminum, Titanium, Chromium, and Copper) during the Ag deposition, ultra-thin (down to 6 nm), smooth (sub-nm roughness), and low-loss Ag films are obtained. Compared to pure Ag films, doped Ag films have a significantly improved long-term and thermal stability, as well as good adhesion to various substrates. Doped Ag films have facilitated diverse high-performance optical and optoelectronic devices, such as

organic solar cells, organic light emitting diodes, optical metamaterials, and plasmonic devices. Organic solar cells using thin doped Ag films as transparent conductors have enhanced power conversion efficiencies (PCEs) thanks to the resonant light harvesting effect; Organic light emitting diodes based on thin doped Ag films have enhanced out-coupling efficiencies and improved mechanical flexibilities; Optical metamaterials consisting of doped Ag films have both a low-loss and homogeneous response; Plasmonic waveguides made of doped Ag films exhibit record-high propagation lengths.

Metamaterials are artificially designed materials with extraordinary optical properties, and have the potential to replace conventional bulky optical systems. Nano-size metamaterials (metasurfaces) are demonstrated for controlling the propagation direction and polarization of light. A 290 nm thick metasurface, which provides asymmetric light transmission, is designed and fabricated. It has a measured transmission efficiency of 80%, an extinction ratio of 13.8 dB around 1.5 μm, and a full width half maximum bandwidth of 1.7 μm. Also, the metasurface has a good performance tolerance against the angle of incidence and constituent nano-structure geometry variations, and is compatible with large-scale manufacturing techniques. In addition, a large-area, printed metasurface is designed and fabricated. It is made of lossless dielectric (silicon) materials and offers the functionality of converting a linearly polarized incident light into a radially polarized light in transmission.

These optical and optoelectronic devices also provide valuable solutions to problems in other fields, such as acoustic wave detection. It is shown that optical resonant structures provide a unique method for acoustic wave detection. Nanoimprinted polymer microring resonators are investigated as high-performance ultrasound detectors. They have a good detection sensitivity (noise equivalent detectable pressure of 105 Pa from 1 to 350 MHz), broad response bandwidth (DC to 350 MHz at -3dB), and immunity to electromagnetic interferences. These advantages have facilitated various applications in photoacoustic imaging and real-time terahertz (THz) pulse detection. To further reduce the detector size, polymer filled silicon metasurfaces on fiber tips are studied. Such metasurfaces are designed to have sharp reflection resonances, which are prone to be modulated by external ultrasound waves. Direct integrating them on the tips of optical fibers further shrink their footprint, and provides viable solutions to applications, such as intravascular photoacoustic imaging, remote strain monitoring, and point-of-interest ultrasound inspection.

1.2 Thesis outline

The thesis can be categorized into three parts: Doped Ag films and their optoelectronic applications; Metasurfaces for light property manipulations; Ultrasound detectors based on optical resonant structures. These parts are closely correlated with each other.

Doped Ag films and their optoelectronic applications

Chapter 2 presents an ultra-thin, smooth and low-loss Al-doped Ag film. With the help of a small amount of Al during Ag deposition, the Ag atoms' Vomer-Webber growth (3D growth) mode is greatly suppressed, and therefore, ultra-thin, smooth and low-loss Ag films are obtained. Ultra-thin and smooth Ag film is achieved down to a 6 nm thickness with a sub-nm roughness, and the doped Ag maintains the good optical properties of pure Ag. Compared to pure Ag, Al-doped Ag also has a significantly improved long-term and thermal stability (up to 500°C), as well as good adhesion to various substrates. Various techniques have been utilized to characterize the optical, structural, and electrical properties of Al-doped Ag films. In the end, preliminary studies of alternative doped Ag films are also discussed. These films include Ti-doped Ag, Cr-doped Ag, and Cu-doped Ag. Their optical, structural, and electrical properties are characterized and compared.

Chapter 3 presents the application of Al-doped Ag films as transparent conductors in organic solar cells (OSCs). Compared to one of the most widely used transparent conductors: indium tin oxide (ITO), thin Al-doped Ag film has the advantages of mechanical flexibility and sufficient conductivity over large areas. In additional, the reflection from the thin metal film can be utilized for resonant light harvesting inside organic solar cells in order to enhance the power conversion efficiencies (PCEs).

Chapter 4 extends the investigations of the resonant light harvesting effect in chapter 3 by inserting an additional dielectric layer (Ta_2O_5) between the fused silica substrate and the thin Al-doped Ag film. On one hand, the Ta_2O_5 layer works as a wetting layer to promote an ultra-thin Ag film formation down to a 4 nm thickness, and such a thin Ag film can work as a transparent conductor in organic solar cells. On the other hand, varying the thickness of the Ta_2O_5 layer will dynamically tune the optical field distribution inside the solar cells, which contributes to optimizations of the resonant light harvesting effect in organic solar cells. In the end, a four-layer, hybrid transparent conductor based on Al-doped Ag is designed and fabricated, which provides a high transmittance over the visible and near-IR range (an averaged transmittance of 92.4% from 400 nm to 1000nm).

Chapter 5 presents the application of doped Ag films as transparent conductors in organic light emitting diodes (OLEDs). OLEDs based on ITO have limited out-coupling efficiencies due to the confined light emission in the ITO layer, as well as poor mechanical flexibilities. Thin doped Ag film provides an effective solution to the above issues. OLEDs based on thin Al-doped Ag and Cu-doped Ag films are designed and compared. An OLED based on a 10 nm thick Al-doped Ag electrode has an out-coupling efficiency of 39.09% in simulation, an 18.4% out-coupling efficiency enhancement compared to that of the optimized 150 nm ITO-based device. The out-coupling efficiency is further improved by replacing Al-doped Ag with a less lossy Cu-doped Ag film (Out-coupling efficiency of 41.61% for a 10 nm Cu-doped Ag based OLED).

Chapter 6 presents a nanophotonic framework enabled by Al-doped Ag films. Two representative nanophotonic devices are investigated: hyperbolic metamaterials (HMMs) and long range surface plasmon polariton (LR-SPP) waveguides. HMMs consisting of thin constituent layers of Al-doped Ag films have both a low-loss and homogenous response. Also, they support a broader bandwidth of high-k modes compared to HMMs made of thicker layers. LR-SPP waveguides based on thin Al-doped Ag films demonstrate an order of improvement in terms of the propagation length (a few centimeters) compared to similar structures made of other plasmonic materials.

Metasurfaces for light property manipulations

Chapter 7 presents a few-layer, asymmetric light transmitting metasurface that have the advantages of high efficiency, broad bandwidth, and robust angular tolerance. The metasurface consists of coupled metallic sheets. It has a measured transmission efficiency of 80%, extinction ratio of 13.8 dB around 1.5 μm, and a full width half maximum bandwidth of 1.7 μm. It is as thin as 290 nm, has a good performance tolerance against the angle of incidence and constituent nano-structure geometry variations, and is compatible with various large-scale manufacturing techniques.

Chapter 8 presents a printed dielectric metasurface for converting a linearly polarized incident light into a radially polarized light in transmission. The metasurface consists of silicon based nano-antennas whose orientations are gradually rotated over the plane. The

two dimensional (2D) nature of metasurfaces corresponds well with the nanoimprint lithography (NIL), which patterns nanostructures over a plane. NIL has the advantages of simplified fabrication, high resolution, great fidelity, and increased throughput, thus providing an efficient and cost-effective method to fabricate metasurfaces. The design methodology and fabrication technique developed in this work are applicable to various metasurfaces.

Ultrasound detectors based on optical resonating structures

Chapter 9 presents high-performance ultrasound detectors based on nanoimprinted polymer microring resonators. They have a good detection sensitivity (noise equivalent detectable pressure of 105 Pa from 1 to 350 MHz), broad response bandwidth (DC to 350 MHz at -3dB), and immunity to electromagnetic interferences. These advantages have facilitated microring's various applications, including photoacoustic imaging and real-time terahertz (THz) pulse detection.

Chapter 10 presents another type of ultrasound detectors based on polymer filled silicon metasurfaces on optical fiber tips. The metasurfaces are designed to have sharp reflection resonances, which are prone to be modulated by external ultrasound waves. Direct integrating these devices on the tips of optical fibers further shrink their footprint, and provides viable solutions to applications, such as intravascular photoacoustic imaging, remote strain monitoring, and point-of-interest ultrasound inspection.

Chapter 11 summaries the work in this thesis and list future directions.

Chapter 2

Ultra-thin, Smooth, Low-loss and Stable Al-doped Ag Films

2.1 Introduction

Thin metal films have many applications in optoelectronic and nanophotonic devices. Among them, silver (Ag) is widely used due to its excellent conductivity (the highest among all metals) and low optical loss in the visible and near-IR band. The low optical loss in the visible and NIR regime partially results from the small free electron damping rate and the location of optical inter-band transitions in the UV range, which also makes Ag one of the most favorable plasmonic materials in the visible and NIR. Thin Ag film has various important applications, e.g., in optical metamaterials [1-5] and transparent conductors [6, 7]. Metamaterials based on thin Ag have enabled promising applications in super resolution imaging [8, 9], negative refractive index metamaterials [10, 11], hyperbolic metamaterials [5, 12], structural color filters [13, 14]. The performance of these devices depends critically on the surface morphology and thickness of the Ag layers [15, 16].

However, it is difficult to obtain a thin and smooth Ag film due to its 3D island formation during the film growth (Vomer-Webber growth mode) [17]. A rough surface morphology will impair the film conductivity and cause additional optical loss, even leading to non-

conductive films when the islands cannot form percolation paths. Though increasing film thickness could alleviate the film continuity issue, the low loss and homogeneity of the metamaterials are inevitably compromised [18]. Also, Ag has poor chemical and thermal stability, and inferior adhesion to popular substrates like silicon and fused silica [19]. In fact, spontaneous de-wetting for a thin Ag film occurs even at room temperature [20] (such degradation is greatly accelerated even for modest temperatures ~100°C [21, 22]), whilst the entirety of Ag films can removed by ultrasonic vibrations or even Scotch tape [23].

To address the above issues, one commonly used method is to deposit a thin adhesion layer (e.g., Germanium [19], Nickel [24], or Molly Oxide [6]) before the Ag deposition, which can significantly reduce the Ag film roughness and promote a thin film formation. However, these adhesion layers generally induce additional optical loss (as they are poor plasmonic materials), which is especially damaging for plasmonic structures since the optical field is enhanced at the metal-dielectric interface. Consequently, even a 1 or 2 nm thick wetting layer will cause a significant plasmonic mode damping [25-27].

Mechanical pressing method is also demonstrated to generate smooth surfaces on a 100 nm Ag film, but it requires both a high working pressure and ultra-smooth mold. Also, it has potential issues of damaging structures underneath the Ag layer [28]. Recently, atomically smooth Ag films have been achieved using a low-temperature epitaxial deposition followed by a room-temperature annealing treatment [29]. However, this approach is complicated

and limited to grow high quality Ag films on silicon substrates. Also, its applicability in fabricating various nanophotonic devices need to be further evaluated.

2.2 Ultra-thin and smooth Ag films by Al doping

Remarkably, just by introducing a small amount of Al into Ag via a simple co-sputtering process (Figure 2.1), the percolation threshold of the resultant film can be reduced down to 6 nm. The Al-doped Ag films were co-sputtered by a DC magnetron sputter tool (Lab18, Kurt J. Lesker Co.) with Argon (Ar) gas at room temperature. The chamber base pressure was pumped down to about 1×10^{-6} Torr before the film deposition. During deposition, the Argon gas pressure was 4.5 mTorr and the substrate holder was rotated at a rate of 10 rpm. Two pure Ag and Al targets were co-sputtered to create Al-doped Ag films. Varying the source powers of Al and Ag targets will adjust the composition of sputtered films. The sputtering rates of Ag at 0.9 nm/s and Al at 0.06 nm/s produced Al-doped Ag films with optimized optical properties.

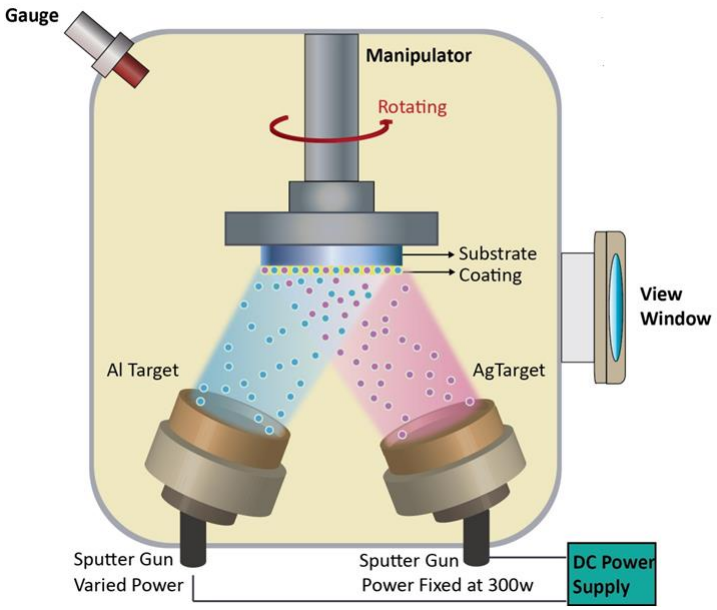

Figure 2.1: Schematic drawing of the Al and Ag co-sputter set-up.

To confirm the ultra-thin thickness of Al-doped Ag films, an annular bright field (ABF) cross-sectional transmission electron micrograph (TEM) of a 6 nm film was taken, which confirmed the film's 6 nm thickness and showed its poly-crystalline structure (figure 2.2). The Al-doped Ag sample with a protective M-bond resin was prepared by hand polishing and a PIPSII ion polishing system. The specimen was studied under STEM mode on a JEOL 3100R05 Cs-Corrected Analytical Electron Microscope.

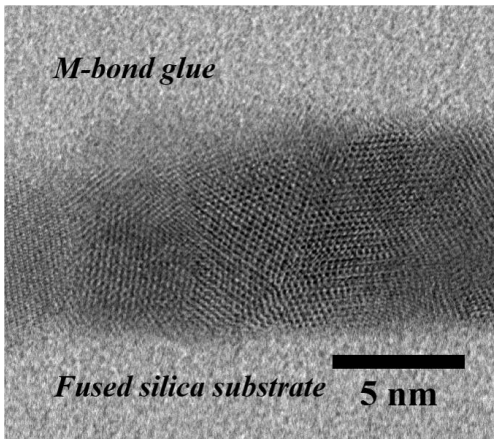

Figure 2.2: An annular bright field (ABF) cross-sectional transmission electron micrograph (TEM) of a 6 nm Al-doped Ag film.

Besides the early onset of a continuous film formation, the Al-doped Ag film has a smooth surface morphology with a significantly reduced root-mean-square (RMS) roughness less than 1 nm. The scanning electron microscopy (SEM) characterization shows drastically different film morphologies between a 9 nm (nominal thickness) pure Ag film by sputtering (Figure 2.3a) and a 9 nm doped Ag film (Figure 2.3b) by Ag and Al co-sputtering. The grain or island-like morphology in Figure 2.3a is typical of a pure thin Ag film. The islands are connected at some local regions, but are lacking of long-range connections. Consequently, the 9 nm pure Ag film is non-conductive. The localized surface plasmon resonance excitations of these islands lead to an extra optical scattering loss of the thin film [30], and its corresponding transmittance spectrum is shown in Figure 2.4. In sharp contrast, the 9 nm Al-doped Ag film is very uniform and smooth. The insets in Figure 2.3a and b show the atomic force microscope (AFM) images of a 9 nm pure Ag and Al-doped Ag films, respectively. The RMS roughness of 9 nm pure Ag film is 10.8 nm. In sharp contrast, the Al-doped Ag films has an over one order lower RMS value of 0.86 nm.

Indeed, the smooth surface morphology of Al-doped Ag films persists to a large film thickness as well. As shown in the insets of Figures 2.3c and d, the Al-doped Ag film has a lower roughness than the pure Ag film (1.1 nm vs. 3.6 nm) for a 100nm thick film. This is also demonstrated by SEM images taken at a 20 degree tilted angle shown in Figure 2.3c and d. The pure Ag film has an orange-peel-like topography and Al-doped Ag film has a sand-like one instead.

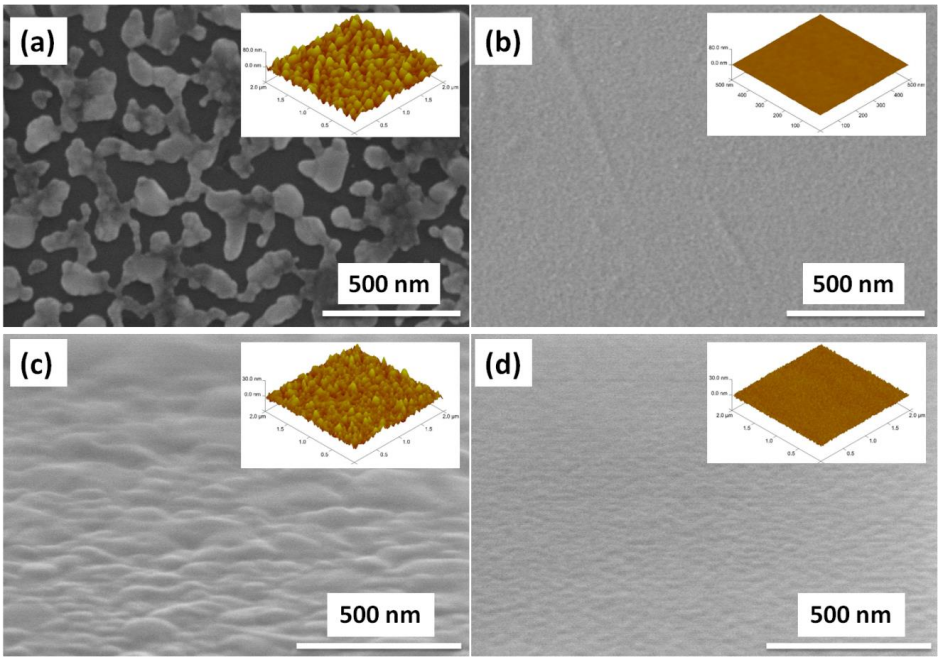

Figure 2.3: SEM and AFM images of pure Ag and Al-doped Ag film. SEM images of (a) 9 nm pure Ag film, (b) 9 nm Al-doped Ag film, (c) 100 nm pure Ag film, and (d) 100 nm Al-doped Ag film. The insets in each figure are their corresponding tapping mode AFM images. All films are deposited on fused silica substrates. The scale bar for AFM images in (a) and (b) is 80 nm and the scale bar in (c) and (d) is 30 nm. The scale bar for SEM images is 500 nm. The 9 nm pure Ag film has an RMS roughness of 10.8 nm, 12 times higher than 9 nm Al-doped Ag film (0.86 nm). The 100 nm pure Ag film has an RMS roughness of 3.38 nm and R_{max} of 28.3 nm, 3 times as those of 100 nm Al-doped Ag film (1.10 nm and 9.95 nm).

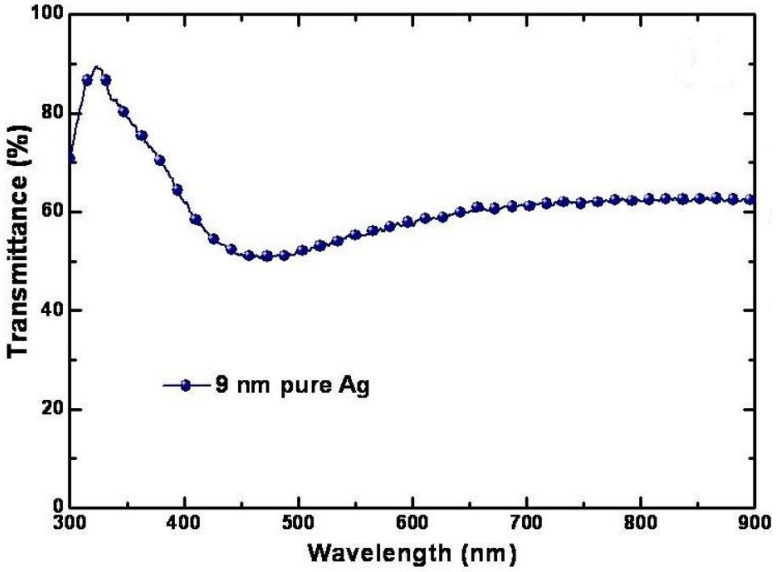

Figure 2.4: Transmission spectrum of a 9 nm (nominal thickness) pure Ag film. The dip corresponds to the excitations of localized surface plasmons in this island-like discontinuous film.

For the Al-doped Ag films, the one with 6 nm thickness has a slightly higher roughness (0.82 nm) than that with 7 nm one (0.78 nm). This is anticipated since 6 nm is a percolation threshold for the formation of a continuous thin film. A film at the initial stage could be more defective in its morphology as compared to a thicker one, leading to its slightly higher roughness. Beyond the 6 nm percolation threshold, the roughness of the Al-doped Ag film decreases slightly when approaching 7 nm. Afterwards, the roughness increases gradually when the film thickness increases to 9 nm (0.86 nm) and 11 nm (1.00 nm). Detailed AFM images of Al-doped Ag films with different thickness are shown in Figure 2.5.

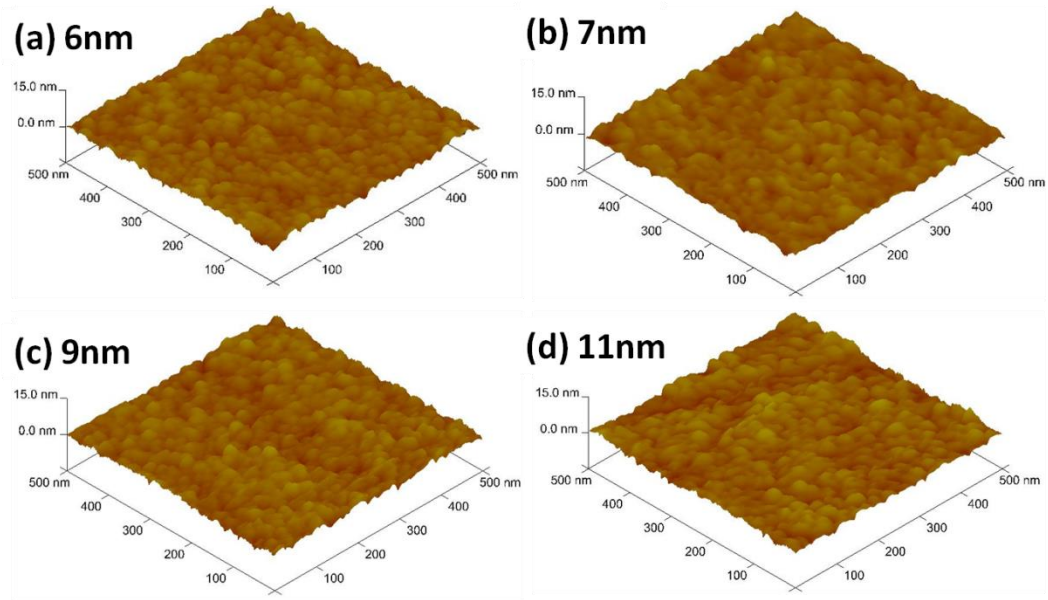

Figure 2.5: 3D tapping-mode AFM images of Al-doped Ag films (a) 6 nm, (b) 7 nm, (c) 9 nm, and (d) 11 nm, showing the RMS roughness of 0.815 nm, 0.782 nm, 0.859 nm, and 1.00 nm, respectively. All films are deposited on fused silica substrates. The scan size is 500 nm × 500 nm.

2.3 Optical properties of Al-doped Ag films

Spectroscopic ellipsometry measurement was utilized as a reliable technique to accurately determine the thickness of ultra-thin films and their corresponding optical properties. In general ellipsometry measurement, there is a correlation between the thickness and the optical constants in thin absorbing films, as the reflection and absorption depend on both the film thickness and its optical coefficients. To break this correlation and precisely determine both the film thickness and its optical constants, “interference enhancement” method was used by depositing the metal film on the silicon substrate with a 300 nm thermal oxide layer on top [31, 32].

The measurement procedure is elaborated in Figure 2.6a. In ellipsometer measurement, $\Psi(\lambda)$ and $\Delta(\lambda)$ are measured at three different angles. They are related to the intensity and phase change of the S and P polarized light after reflection upon the sample. Afterwards, $\Psi(\lambda)$ and $\Delta(\lambda)$ are used to fit the optical constants (n and k) and the thickness of the film. In the case of a thin absorbing film, the fitting is not unique, as the change of reflection intensity and phase of the S and P polarized light can come from either the film absorption or the film thickness variation. To break such a correlation, a thin transparent layer (SiO_2 in our measurement) is put underneath the absorbing film. It provides extra reflected light and thus additional information for the subsequent data fitting. Using this "interference enhancement" method, both the film's optical constants and thickness can be uniquely determined. Figure 2.6b shows the normalized fitting error as a function of different Al-doped Ag thicknesses for a 6 nm film. There is a minimum fitting error at 6 nm, a direct evidence of the ultra-thin feature of the Al-doped Ag film. The measured permittivities of Al-doped Ag films are plotted in figures 2.8 and 2.10.

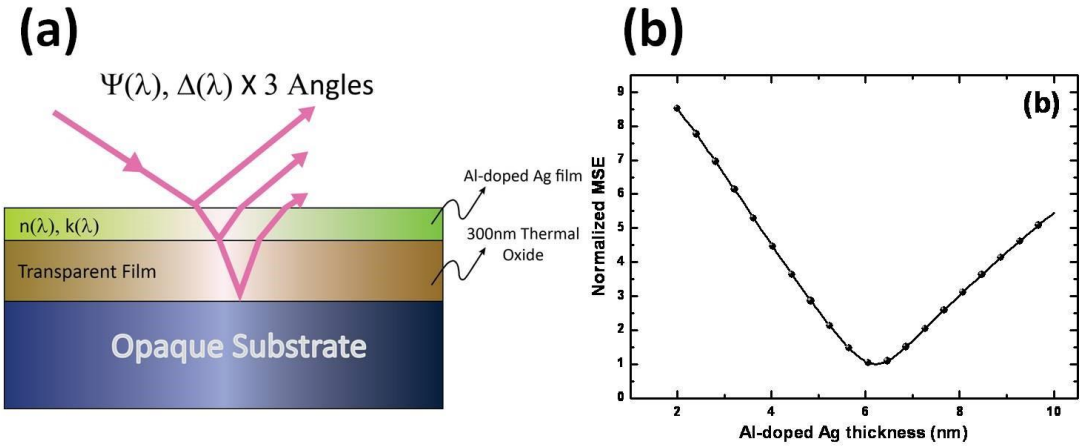

Figure 2.6: (a) Schematic of ellipsometry measurement procedure using the interference enhancement method. (b) Thickness fitting uniqueness of a 6 nm Al-doped Ag film.

2.4 Significantly improved stabilities of Al-doped Ag films

Pure Ag films are known to have poor stabilities both at room temperature and under elevated temperatures. In contrast, Al-doped Ag films are radically less susceptible to de-wetting and degradation. The upper part of figure 2.7a shows the image of a 15 nm pure Ag film and a 7 nm Al-doped Ag film on fused silica substrates right after their deposition, where both exhibit uniform and similar appearances. However, pure Ag thin films are not stable in air, even at room temperature, and this 15 nm film degrades rapidly (spontaneous de-wetting occurs) after being taken out of the deposition chamber for only 30 minutes (lower part, figure 2.7a). This is due to the aggregation of Ag atoms, which is shown in its SEM picture taken 30 minutes after the sample being taken out of the deposition chamber (figure 2.7b).

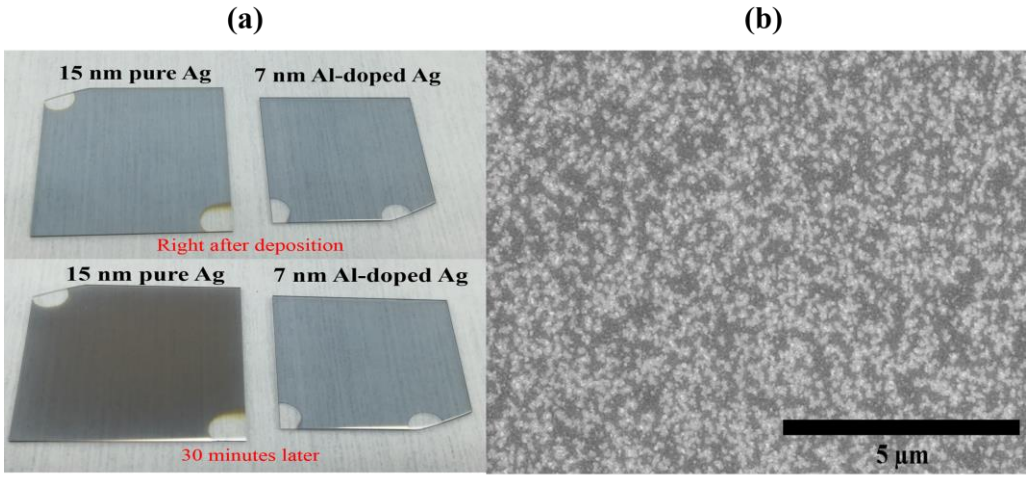

Figure 2.7: Stability of thin pure Ag and Al-doped Ag films at room temperature. (a) Upper side: pictures of 15 nm pure Ag and 7 nm Al-doped Ag on fused silica substrates right after deposition, where both exhibit clean and similar appearances. Lower side: pictures of 15 nm pure Ag and 7 nm Al-doped Ag on fused silica substrates 30 minutes after deposition, where the pure Ag film has already degraded. In contrast, Al-doped Ag films have good stability in ambient environment. (b) SEM of a 15 nm pure Ag film on fused silica substrate 30 minutes after the deposition, and the Ag atoms have aggregated to form islands.

In contrast, Al-doped Ag films have a significantly improved stability in air compared with pure thin Ag films. Figure 2.8a shows the pictures of a freshly deposited Al-doped Ag film on fused silica substrate (left), and another sample which has been 6 months after deposition (right). Both films show uniform and similar appearances. Also, the permittivities of the two samples are measured, which show close values (figure 2.8b).

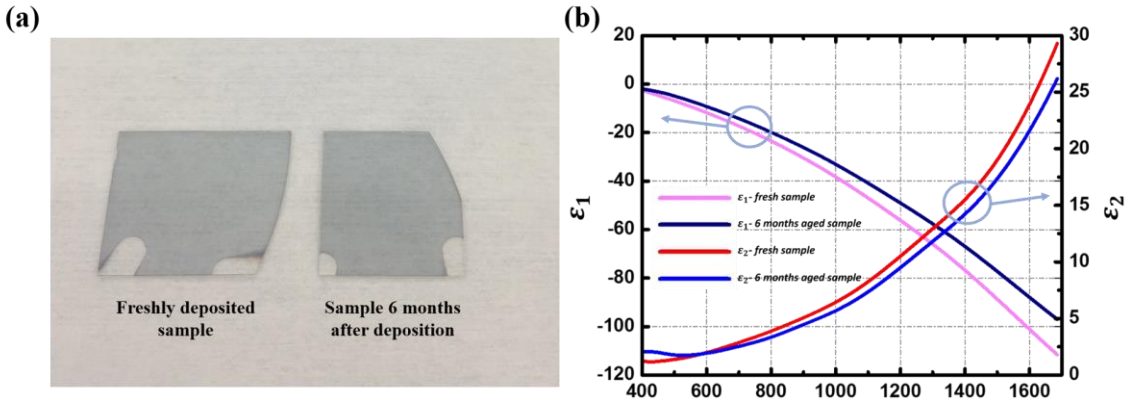

Figure 2.8: Long-term stability of Al-doped Ag films. (a) pictures of a freshly deposited Al-doped Ag film on fused silica substrate (left), and another sample which has been 6 months after deposition (right). Both films show uniform and similar appearances. (b) Measured permittvities of a fresh sample and a sample deposited 6 months ago, which show close values.

The thermal stability of Al-doped Ag is also significantly improved compared to pure Ag. Figure 2.9a shows the SEM of a 30 nm pure Ag film after being heated in a nitrogen (N_2) environment for 3 minutes, and the Ag film has totally de-wetted from the fused silica substrate. In contrast, a 7 nm Al-doped Ag film can withstand thermal treatments at 500°C in a N_2 environment and still maintains its smooth surface morphology. Figure 2.9b shows the SEM of a 7 nm Al-doped Ag film which underwent annealing treatment in a N_2 environment at 500 °C for 3 minutes (RMS roughness changes from 0.773 nm to 0.836 nm after heating, inset of figure 2.9 b).

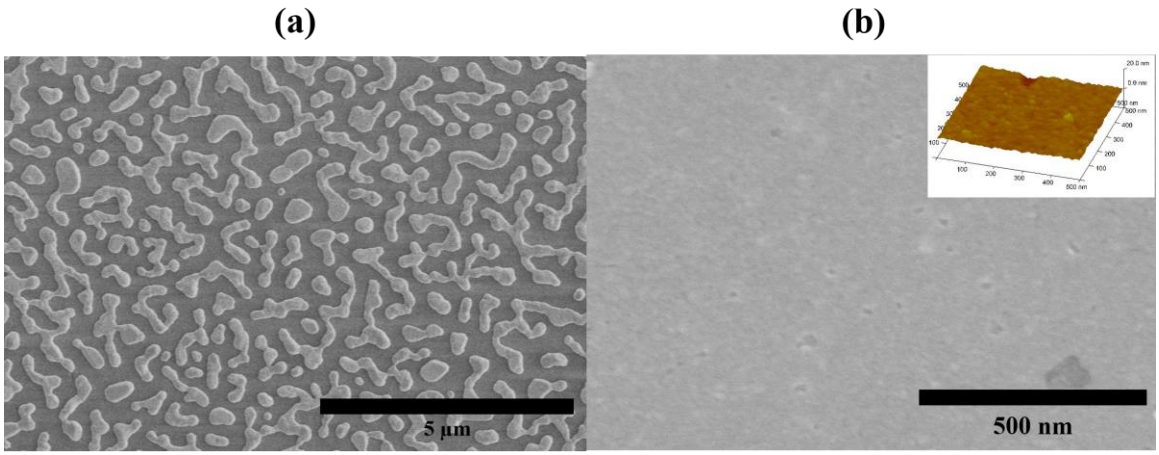

Figure 2.9: Thermal stability of pure Ag and Al-doped Ag films. (a) SEM of a 30 nm pure Ag film after being heated in a nitrogen (N_2) environment for 3 minutes, and the Ag film has totally de-wetted from the substrate. (b) SEM of a 7 nm Al-doped Ag film which underwent annealing treatment in a N_2 environment at 500 °C for 3 minutes. Al-doped Ag film maintains its smooth surface morphology, and its RMS roughness changes from 0.773 nm to 0.836 nm (AFM image in the inset).

In fact, after the thermal treatment, the optical loss of Al-doped Ag films is further reduced, which is due to the removal of defects from films [33]. Figure 2.10 shows the measured permittivities of both as-deposited Al-doped Ag, and Al-doped Ag that undergoes annealing treatment at 500 °C in a nitrogen (N_2) environment for 3 minutes. Compared to the permittivity values of as-deposited Al-doped Ag, the real part of permittivity of annealed Al-doped Ag is similar, while the imaginary part of permittivity (which is proportional to the optical loss) is significantly reduced. Furthermore, such improvement of the Al-doped Ag films can be observed for annealing cycles even as short as 10 seconds, making these films suitable for rapid thermal annealing treatments commonly used in semiconductor manufacturing.

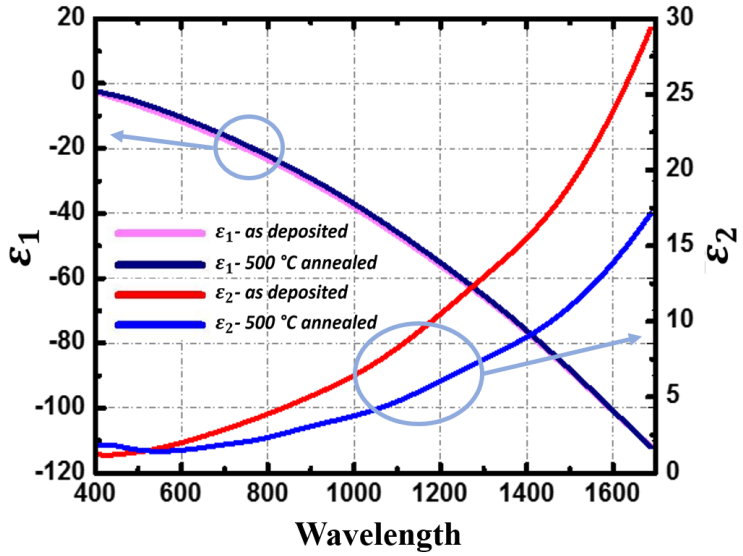

Figure 2.10: Measured real and imaginary parts of permittivity of as-deposited Al-doped Ag films and films underwent annealing treatment (500 °C for 10 s in N_2). Annealing treatment doesn't affect too much the real part of permittivity, but significantly reduces its imaginary part (lower down the optical loss).

Finally, the adhesion of Ag films to many widely used substrates has been improved. Since pure Ag is easily removed by ultrasound sonication or even Scotch tape, it requires adhesion layers to improve adhesion, which unfortunately degrade the device's optical performance [25-27]. Al-doped Ag has a sufficient adhesion with substrates to enable film processing in ultrasonic baths with many commonly used chemicals and solvents (e.g., resists, acetone, and isopropyl alcohol, etc). This is a crucial property that profoundly simplifies the fabrication of many nanophotonics devices that require either planar or patterned thin films, (e.g., plasmonic interconnects, metamaterials, and semi-transparent conductors).

2.5 Mechanism of ultra-thin Ag film formation

The amount of Al incorporation is less than 10% in terms of the atomic concentration in Al-doped Ag films under the "0.9 nm/s Ag and 0.06 nm/s Al" combination, which is evidenced by the X-ray photoelectron spectroscopy (XPS) in figure 2.11. Ag and Al have almost identical atomic radius (1.44 Å for Ag and 1.43 Å for Al) and same crystalline structure (face centered cubic). Therefore, adding a small percentage of Al atoms into Ag film does not affect the electrical and optical properties of the film much. The film property should be similar to pure Ag film property but with the advantages of being ultra-thin and smooth.

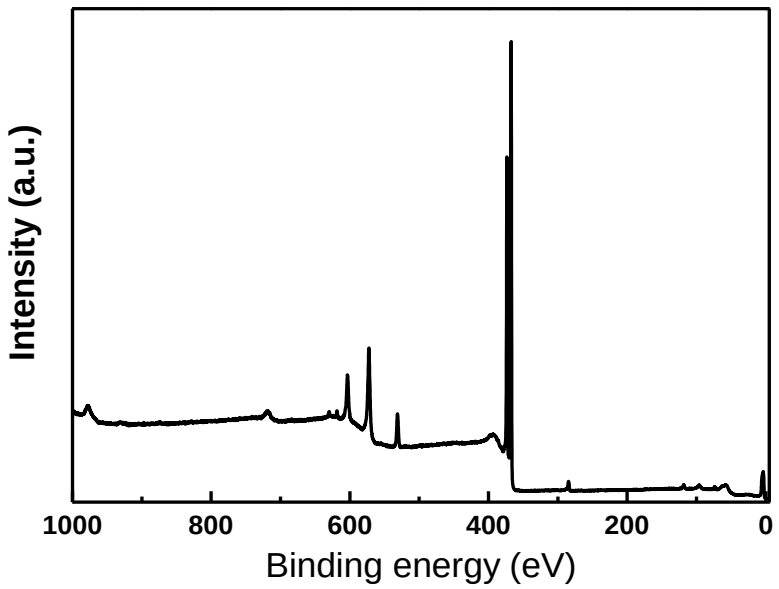

Figure 2.11: XPS spectrum of the Al-doped Ag film recorded by survey scanning. The atomic concentration of Al (less than 10%) was determined from the peak areas of Al2p and Ag3d by their respective atomic sensitivity factors.

The smooth surface morphology and lower percolation threshold of Al-doped Ag films indicate that a small amount of Al may strongly influence the nucleation and subsequent growth of Ag films on the substrate [34]. In order to investigate the effect of Al-doping on the nuclei density of Ag films, the surface morphology of pure Ag and Al-doped Ag films with a nominal thickness of 3 nm was measured by AFM. Figures 2.12a and b show that Al-doping results in smaller and denser particle clusters than those in pure Ag films. This reveals that Al-doping increases the nuclei density of Ag films.

The nuclei density and particle size of metal films are related to the diffusion rates of the metal atoms on the dielectric surface [35]. The metals with a smaller diffusion rate on the surface exhibit a higher nuclei density and smaller particle size. The diffusion rate of metal atoms on oxide substrates generally decreases with the increase of metal-oxygen bond strength [35, 36]. The bond strength of Al-O bonds is much larger than that of Ag-O bonds [37]. As a result, the average diffusion distance of Al atoms on the surface of SiO_2 is smaller than that of Ag atoms, and therefore, Al atoms are easier to be immobilized on the surface of fused silica substrates than Ag. Consequently, Al-doping results in an enhanced density of heterogeneous nucleation sites, thus leading to a larger nuclei density, a smaller particle size, and a smoother film morphology.

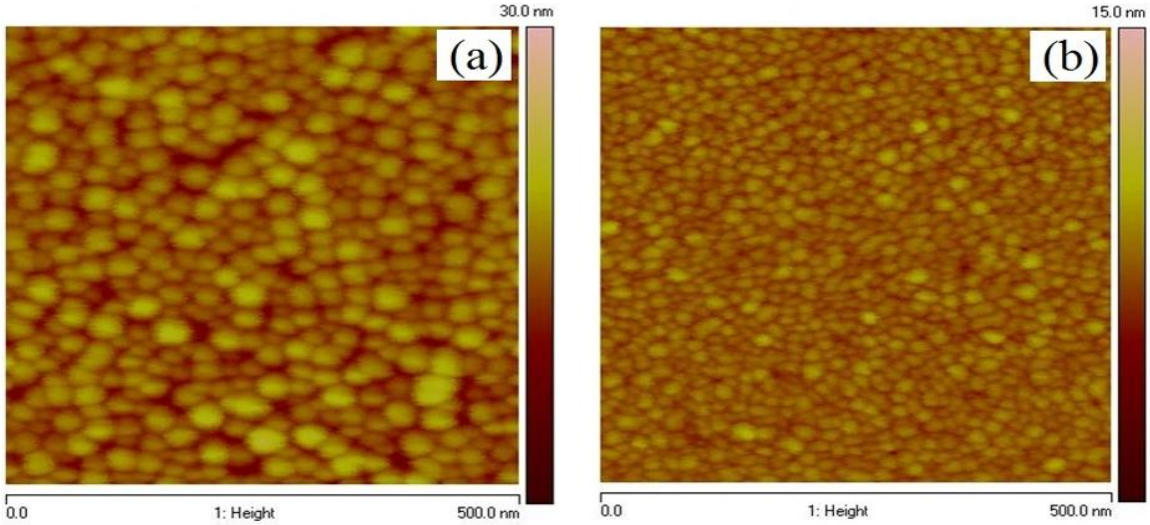

Figure 2.12: The 2D AFM images of (a) 3 nm pure Ag films and (b) 3 nm Al-doped Ag films. Al-doping results in smaller and denser particle clusters on the substrate than those in the pure Ag films.

2.6 Alternative ultra-thin, smooth and low-loss doped Ag films

As discussed earlier, ultra-thin and high-quality Ag films can be obtained by adding a small amount of Al during the Ag deposition. Al suppresses Ag atom's 3D growth mode and promotes a thin and smooth film formation. An ultra-thin and smooth Ag film is achieved with a thickness down to 6 nm as well as a sub-nm roughness. Also, the film has a significantly improved stability compared to pure Ag film. Subsequently, a natural question to ask will be: would other doping elements work as well to promote a thin Ag film formation, and how the properties of these films will be? A systematic study of doped Ag films with different doping elements will not only provide alternative thin doped Ag films with diverse properties, but also help to unveil the mechanism of such a thin doped film formation.

In this study, three different doping elements were investigated: Titanium (Ti), Chromium (Cr), and Copper (Cu). These materials were chosen based on their compatibility with the existing sputtering system, as well as their low cost and easy availability to the research community. During the experiment, the sputter power of Ag was kept at a constant value (230 w), and the power of the doping metal was adjusted in order to obtain co-sputtered thin film with different compositions. Spectroscopic ellipsometry was employed to determine the sputtering powers for depositing films with the optimized optical properties. Afterwards, the doped Ag film's surface morphology, conductivity, and structural properties were characterized.

Figure 2.13 shows the measured permittivities of the three kinds of doped Ag films with lower, optimized, and higher doping concentrations. During the experiment, the sputter power of the Ag target was kept at 230 w, while the power of the doping metal target was varied in order to deposit thin (~ 8 nm) doped Ag films with different compositions. For a thin Ag film with a lower doping, the film is less metallic (with a smaller ε_1). Also, the film's permittivity deviates from the trend of the Drude model, with a higher ε_2 over the visible and NIR range. It is known that pure Ag cannot form a high-quality thin film due to the 3D growth mode of the Ag atoms. The doping atoms provide nucleation sites to immobilize the Ag atoms on the substrate and therefore, reduce the percolation threshold of Ag films. However, with a non-sufficient doping concentration, the 3D growth mode of Ag atoms cannot be effectively suppressed and the resultant films have defects. This leads to a higher loss of the doped Ag films. For Ag films with both optimized and higher doping

concentrations, the films show good metallic behavior, and the permittiviies are correspond well with the Drude model. However, for Ag films with higher doping concentrations, the loss is higher. Although the doping atoms will promote a thin Ag film formation, a too high concentration of these atoms will also introduce additional loss into the resultant film.

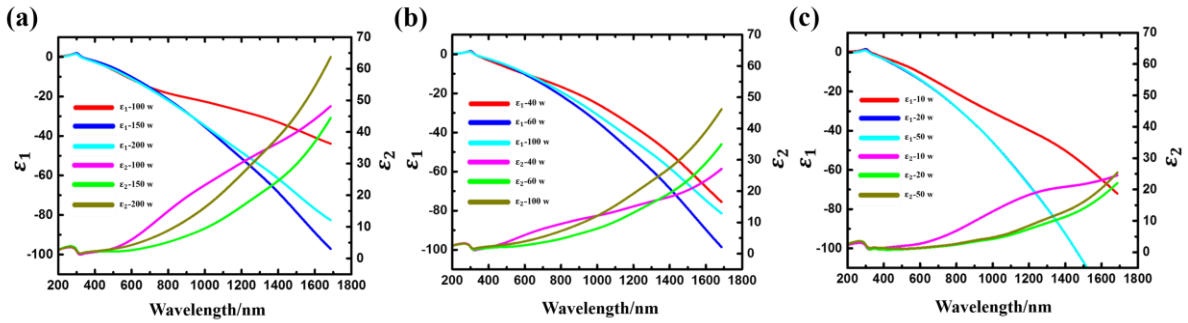

Figure 2.13: Permittivities of different doped Ag films with lower, optimized, and higher sputter powers of the doping metals. (a) Ti-doped Ag; figure. (b) Cr-doped Ag. (c) Cu-doped Ag. The sputter power of Ag is kept at 230 w in all cases.

Similar to Al-doped Ag films, Ti/Cr/Cu-doped Ag films also have smooth surface morphologies. Figure 2.14 shows the SEM pictures of ~ 8 nm doped Ag films with the optimized doping concentrations. All films have a sub-nm roughness, confirmed by AFM measurement. The film's conductivity was characterized by four point probe measurement. For a ~ 8 nm film, the sheet resistances of Ti-doped Ag, Cr-doped Ag, and Cu-doped Ag are 48.9, 24.3 and 12.6 Ω sq^{-1}, respectively.

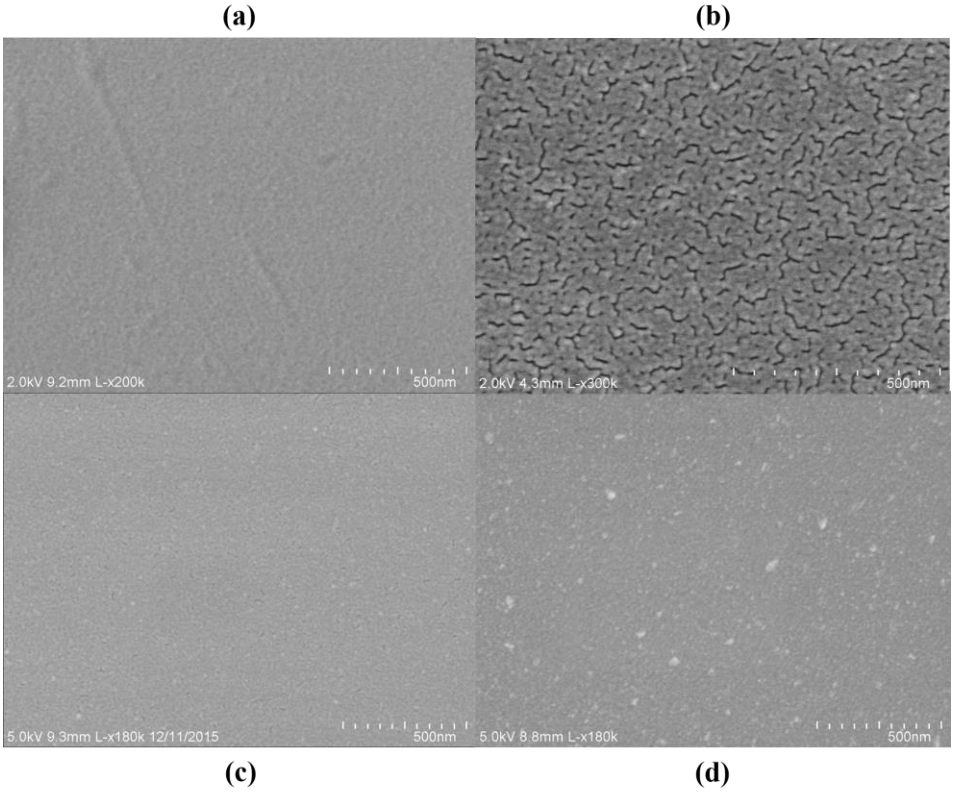

Figure 2.14: SEM pictures of ~8 nm (a) Al-doped Ag film; (b) Ti-doped Ag film; (c) Cr-doped Ag film; (d) Cu-doped Ag film. All films are deposited on fused silica substrate.

The film's structural composition was characterized by the X-ray diffraction analysis (XRD). In order to get scans with a good signal to noise ratio (SNR), samples with a 50 nm thickness were used. All samples show similar structural compositions compared to pure Ag films (figure 2.15). Since the doping element's concentration is low, the doped Ag film still maintains the structural properties of pure Ag.

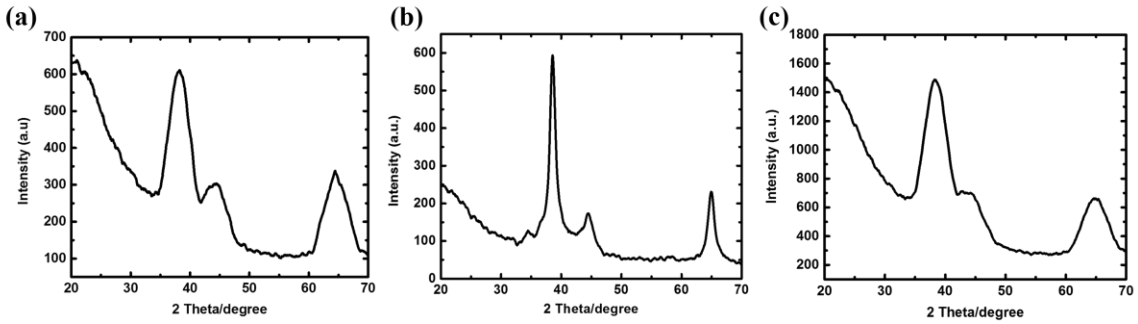

Figure 2.15: XRD scans of a (a) 50 nm pure Ag film; (b) 50 nm Cr-doped Ag film; (c) 50 nm Cu-doped Ag film. All films are deposited on amorphous fused silica substrate, and they have similar diffraction peak positions.

2.7 Conclusions

This chapter presents an ultra-thin, smooth, and low-loss Al-doped Ag film. Al doping increases the nucleation sites on the substrates and suppresses the Vomer-Webber growth (3D growth) mode of Ag atoms. Consequently, ultra-thin, smooth, and low-loss Ag films can be obtained. Compared to pure Ag, Al-doped Ag has a significantly improved long-term and thermal stability, as well as good adhesion to various substrates. Several techniques (spectroscopic ellipsometry, SEM, AFM, TEM, and XPS) have been utilized to characterize the optical and structural properties of Al-doped Ag films. In the end, preliminary studies of alternative doped Ag films are also discussed. These films include Ti-doped Ag, Cr-doped Ag, and Cu-doped Ag. Their optical, structural, and electrical properties are characterized and compared.

Chapter 3

Organic Solar Cells Using Al-doped Ag Films as Transparent Conductors

3.1 Introduction

Optically transparent conductors are required for most optoelectronic devices. Currently, one of the most commonly used transparent conductors is indium tin oxide (ITO); However, it suffers from issues, such as poor mechanical flexibility, insufficient conductance for large-area devices, and rising cost due to the limited Indium supplies on the planet as well as the roaring displays and related electronics market [38]. To meet these challenges, many alternative transparent electrodes have been developed, including graphene [39-41], carbon nanotubes [42], highly conductive polymer [43-45], patterned metal grid [46, 47], as well as metal nanostructures and nanowires [48-54]. Carbon-based materials improve the mechanical flexibility of electrodes; however, the low conductivity largely limits their electronic performance [55]. Transparent metal mesh structures and nanowire networks require complex patterning or synthesis. Moreover, both platforms only provide global conductivity but are totally non-conductive between the wires, which limits these nanostructures' applications as transparent electrodes for light-emitting diodes (LEDs) and photovoltaics (PVs) unless an additional conducting layer is added [56, 57]. Many practical applications, including large-area flexible organic photovoltaics (OPVs),

still call for easy-to-fabricate and high-performance transparent conductors. A thin and continuous metal film by a simple deposition method is an ideal solution, and can be integrated into semi-transparent smart windows [58, 59] and tandem structures [60, 61].

Considering the application as transparent electrodes, thin Ag films should be semi-transparent and with good conductivity. However, Ag follows the 3D growth mode: during deposition, Ag atoms first agglomerate into isolated islands, and as the deposition continues, these islands finally connect to each other and form a continuous film. On one hand, a certain threshold of thickness (usually beyond 10 nm) is required to get a continuous and conductive Ag film. Though the conductivity is satisfied by a thicker film, the transparency is inevitably compromised. On the other hand, the roughness of a continuous Ag film is large (e.g., a root-mean-square (RMS) roughness of 6 nm for a 15 nm Ag film), which results in an additional light scattering loss. Moreover, since most OSCs and OLEDs are only few hundred nm thick, a rough surface could easily result in electrical shorts between electrodes, especially for large-area devices.

3.2 Optical and electrical characterizations of Al-doped Ag films

The ultra-thin and smooth Al-doped Ag film satisfies the requirements of a desirable transparent electrode by its simple fabrication process, close-to-flat transmission spectrum, easy device integration, and robustness. It is worth highlighting that the surface roughness of electrodes is detrimental for the reliability of organic optoelectronic devices, which

originates from irregularities of the electrode itself or tiny particles adsorbed on top of its surface [62, 63]. Since the whole device thickness is only on the order of hundred nanometers, a rough surface could easily result in electrical shorts between the electrodes, especially for large-area devices. The devices with rough electrodes are prone to obtain low efficiencies due to the current shunt paths which produce higher dark currents [51]. The naturally smooth Al-doped Ag film is of significance to provide a simple solution to overcome this problem.

The ultra-thin Al-doped Ag film has a high transparency while remaining a good electrical conductivity. Transmittances of Al-doped Ag films with different thicknesses are plotted in figure 3.1a. Although the 6 nm Al-doped Ag film is thinner, its transmittance is lower. This corresponds to the fact that 6 nm is the percolation threshold for a continuous film formation, and there are more defects in the film at this stage. To demonstrate this, the imaginary parts of permittivities (ε_2) of films with different thicknesses are plotted in the inset of figure 3.1a, and ε_2 of a 6 nm film is higher than those of others. The transmittance of a 7 nm film is greater than 80% up to around 500 nm, and drops towards the longer wavelength. This behavior is typical of a continuous metal film, where there is an increased reflection from the film towards longer wavelengths. It is worthwhile to note that the increased reflection from the thin metal electrode, together with the high reflection from the top thick anode in the OPV devices, can be advantageously utilized to form a Fabry-Perot (FP) optical cavity to improve the optical absorption by the thin organic active layer.

This strategy can benefit the power conversion efficiencies (PCEs) of OPVs, which will be discussed in detail later.

A 45 nm ZnO layer is spin-coated on the Al-doped Ag film to work as an electron transporting and hole blocking layer. Consequently, the overall transmittance is further increased to above 80% from 400 to 800 nm in the case of a 7 nm film, exhibiting a transmittance of 92% at 550 nm, as shown in Figure 3.1b. This can be explained that the ZnO film works as an anti-reflection layer (Figure 3.2a). The ZnO coated Al-doped Ag films of different thicknesses are also compared to other reported transparent conductors in terms of transmittance at 550 nm versus sheet resistance (Figure 3.2b), where they show a similar or superior performance. Since the ZnO layer thickness needs to meet other requirements for the OPV device operation, no further optimization of the ZnO layer thickness is carried out at this stage to achieve a maximized transmittance.

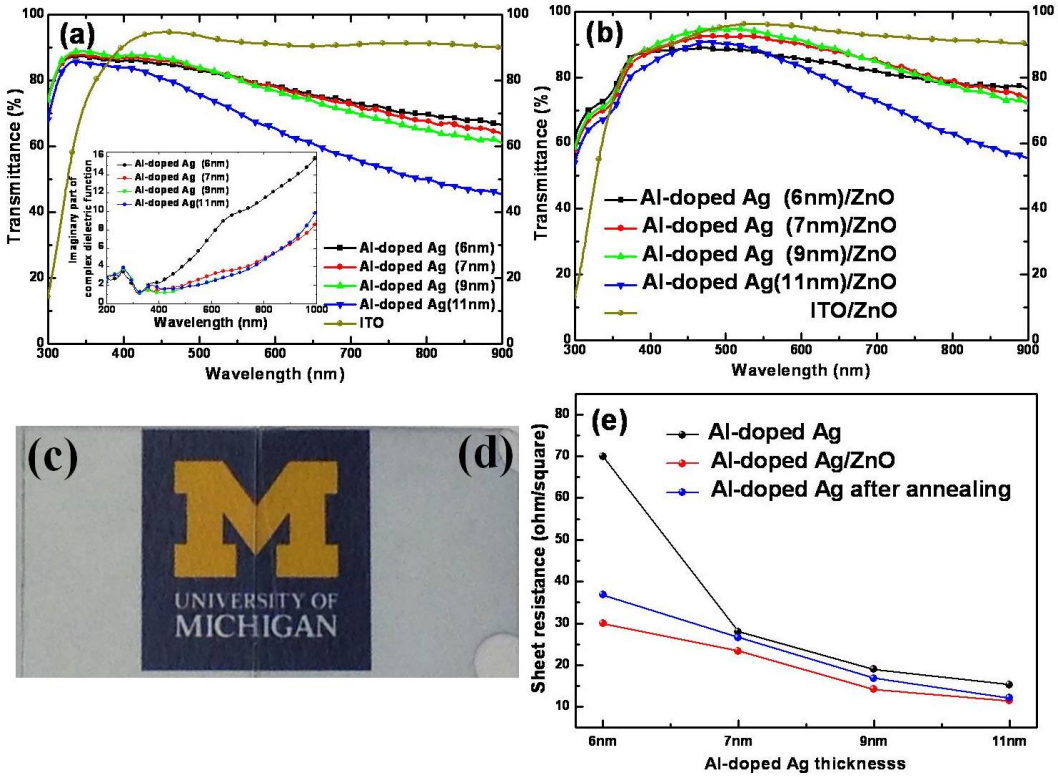

Figure 3.1: Transmittance spectra of (a) Al-doped Ag films and (b) Al-doped Ag/ZnO films with different thickness (6, 7, 9, and 11 nm), in which ITO and ITO/ZnO films are shown as well. Photos of (c) ITO/ZnO and (d) 7 nm Al-doped Ag/ZnO transparent conductors in front of a colored logo. The inset of in (a) compares the dependence of the imaginary part of the complex dielectric function on the wavelength for Al-doped Ag films with different thickness (6, 7, 9, and 11 nm). (e) Sheet resistance versus the Al-doped Ag film thickness (black: Al-doped Ag film; red: Al-doped Ag/ZnO film; blue: Al-doped Ag film after annealing in N_2 environment).

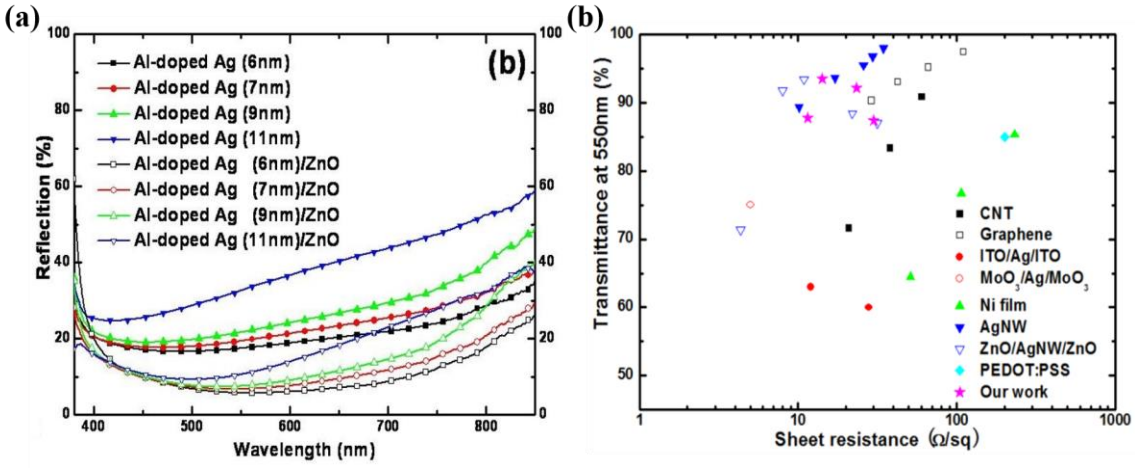

Figure 3.2: (a) Reflection spectra of Al-doped Ag films and Al-doped Ag/ZnO films with different thicknesses (6, 7, 9, and 11 nm). Adding the ZnO layer further suppresses the reflection. (b) Comparison of optical transmittance (at 550 nm) versus sheet resistance for our work Al-doped Ag/ZnO and other reported works: CNT [55] , Graphene [64], ITO/Ag/ITO [65], MoO_3/Ag/MoO_3 [7], nickel thin films [66], silver nanowires (AgNW) [67], ZnO/AgNW/ZnO [68], PEDOT:PSS [44]. Note that all selected data are based on their applications in optoelectronic devices.

The sheet resistances of Al-doped Ag (Al-doped Ag/ZnO) films with different Ag thicknesses of 6, 7, 9, and 11 nm are 70 (30), 28 (23.4), 19 (14.2), and 15.3 (11.5) Ω sq^{-1}, respectively (Figure 3.1e). The Ag film conductivity improves as its thickness increases [69, 70]. Notably, there is a significant drop in the film sheet resistance from 6 nm to 7 nm, which further supports that 6 nm is the percolation threshold. The conductivity of the film is further improved after the ZnO coating, which is partially attributed to the baking treatment for converting the ZnO sol gel to a ZnO crystalline film. To prove this, post-annealing treatment to Al-doped Ag films was carried out in a nitrogen (N_2) environment at 150 °C for 15 minutes (the same temperature and time as that for baking the ZnO sol gel film) and the drop in sheet resistance was observed (Figure 3.1e). The reason for the improved conductivity can be explained that the defects and scattering sites in the thin

films which affect the free electron motion can be reduced by an annealing treatment [71, 72].

3.3 Organic Solar cells with Al-doped Ag films as transparent conductors

Al-doped Ag films with different thicknesses have been deposited for evaluating their feasibility as transparent electrodes in OPVs, and their performance are compared to those of OPVs made on ITO electrodes with other layers being identical. The device geometry using ITO and ultra-thin Al-doped Ag electrodes is shown in Figure 3.3.

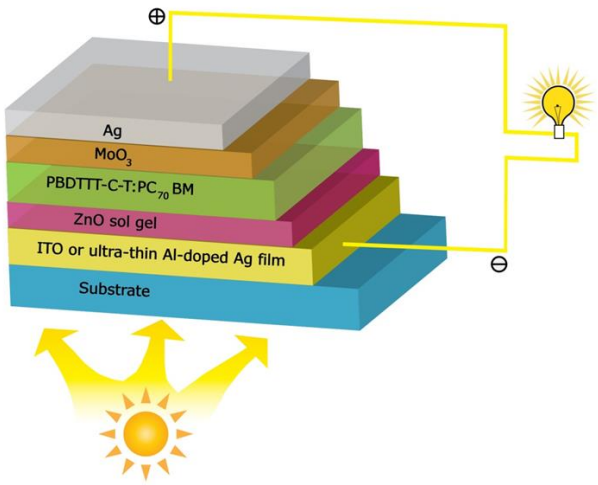

Figure 3.3: The solar cell geometry using either an ITO or ultra-thin Al-doped Ag electrode.

Control devices were fabricated on ITO coated glass substrates with a sheet resistance of 12 Ω sq^{-1}. The substrates were cleaned in an ultrasonic bath with acetone and isopropyl alcohol for 10 minutes. The ITO surface was cleaned by an oxygen plasma for 100 s. It is

worth mentioning that the Al-doped Ag film does not require any surface treatment for making OPV devices [73]. The ultra-thin Al-doped Ag film and ITO coated substrates were transferred into a glove box filled with N_2 for the ZnO coating. The ZnO sol gel solution was prepared as reported [74] and was spin-coated on top of ITO and Al-doped Ag films, followed by baking at 70 °C for 5 minutes. Then the ZnO sol gel coated substrates were taken out of the glove box and baked at 150 °C for 15 minutes in air. Consequently, a 45 nm ZnO layer was formed. Afterwards, the substrates were transferred into the glove box again for the polymer active layer deposition. A blend solution made of poly[4,8-bis-(2-ethylhexyloxy)-benzo[1,2b:4,5b0]dithiophene-2,6-diyl-alt-4-(2-ethylhexyloxy)-thieno-[3,4b]thiophene-2,6-diyl] (PBDTTT-C-T) (Solarmer) and [6,6]-phenyl C71-butyric acid methyl ester (PC70BM) (American Dye Sources Inc.) with a weight ratio of 1:1.5 in chlorobenzene (25 mg mL^{-1}) with 3 vol% 1,8-diiodooctane (DIO, Sigma-Aldrich) was spin-coated onto the ITO and Al-doped Ag substrates to form an active layer (~90 nm). This blend organic active layer exhibits a broad and strong light absorption from 350 to 750 nm as shown in Figure 3.5b. Subsequently, MoO_3 (6 nm) and Ag (100 nm) were evaporated (1×10^{-6} mbar) (Kurt J. Lesker). The final cells have an isolated electrode with a diameter of 1 mm.

The current density-voltage (J-V) characteristics were measured using a Keithley 2400 system while the solar cells were illuminated by AM 1.5 G simulated sunlight generated by an Oriel Solar Simulator with an irradiation intensity of 100 mW/cm^2. The incident power intensity at one sun was calibrated using a Silicon reference cell. The devices were

measured in the atmosphere without any encapsulation. The EQE measurement was performed in a nitrogen glove box and the EQE spectra were obtained using light from a 200 Hz-chopped, monochromated Xenon-lamp, which was calibrated against a silicon solar cell.

Figure 3.4a shows the comparison of the J-V characteristics of the devices whose electrode is either ITO or ultra-thin Al-doped Ag films of different thicknesses. The summary of their main photovoltaic parameters is tabulated in Table 3.1. ITO based device has a PCE of 6.87% with a short-circuit current density (J_{sc}) = 14.00 mA cm^{-2}, open-circuit voltage (V_{oc}) = 0.80 V, and fill factor (FF) = 61.3%. Devices built upon Al-doped Ag films with various thicknesses produce similar or better efficiencies than those made on ITO electrodes. Note that the OPV device fabricated on a 6 nm Al-doped Ag film has a similar performance to the ITO-based device. With the decrease of film thickness from 11 nm to 7 nm, J_{sc} and FF increase, producing a maximal PCE of 7.44% at 7 nm. However, further reducing of Al-doped Ag thickness to 6 nm lowers the J_{sc} and decreases PCE to 6.72%. The identical V_{oc}'s of 0.8 V obtained here imply that favorable Ohmic contacts are formed at both anode and cathode electrodes for both ITO and Al-doped Ag films with the aid of interfacial metal oxide layers, *i.e.,* MoO_3 [74, 75] and ZnO [74]. In this case, the V_{oc} is essentially determined by the difference between the highest occupied molecular orbital (HOMO) of PBDTTT-C-T and the lowest unoccupied molecular orbital (LUMO) of PC70BM [76]. Meanwhile, the FFs of ITO and Al-doped Ag based devices are comparable due to the good contacts of ITO or Al-doped Ag with the ZnO layer, resulting in similar

series resistances shown in Table 3.1. Therefore, it can be concluded that the increase in the PCEs of the Al-doped Ag based devices primarily originates from the enhancement of J_{sc}.

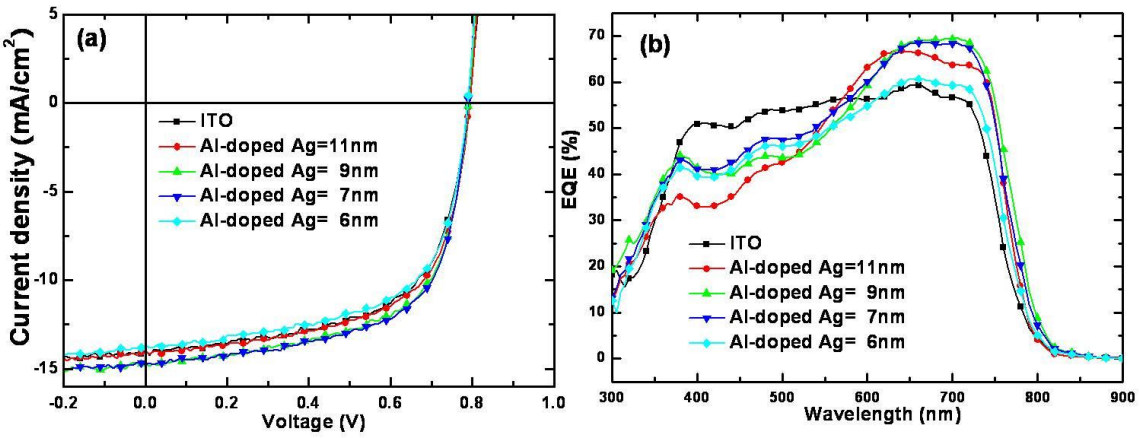

Figure 3.4: (a) J-V characteristics of ITO based and ultra-thin Al-doped Ag based OPVs. (b) EQEs of ITO based and ultra-thin Al-doped Ag based OPVs.

Table 3.1: Summary of the main photovoltaic parameters of the devices with ITO and Al-doped Ag films with different thicknesses as electrode.

	J_{SC} [mA cm^{-2}]	V_{oc} [V]	FF [%]	PCE [%]	R_s [Ω·cm^2]	R_{sh} [Ω·cm^2]
ITO	14.00	0.80	61.3	6.87	4.0	462.9
Al-doped Ag=11nm	14.03	0.80	62.0	6.95	3.9	460.0
Al-doped Ag= 9nm	14.70	0.80	62.5	7.35	3.3	498.2
Al-doped Ag= 7nm	14.76	0.80	63.0	7.44	3.0	512.5
Al-doped Ag= 6nm	13.71	0.80	61.3	6.72	3.4	368.0

Figure 3.4b shows the external quantum efficiencies (EQEs) of the devices with ITO and ultra-thin Al-doped Ag films with different thicknesses. This spectral response reflects the device's capability of converting photons to electrons at certain wavelengths, where the J_{sc}

can be obtained from the integral of the product of the measured EQE and incident light spectrum from the solar simulator. The spectral response of Al-doped Ag based device is different from that of ITO based device, where the former exhibits a significant enhancement in the long wavelength range, while the ITO based device has a fairly flat response.

In order to understand the origin of the photocurrent enhancement, the EQE and total absorption efficiency (TAE = 1-R, where R is the measured reflection from the device) are plotted and compared in Figure 3.5a, as well as relative TAE and EQE enhancement (ratio of 7 nm doped-Ag based device over ITO based device) in Figure 3.5b. The 7 nm Al-doped Ag based device shows a reduced EQE in the range from 370 to 580 nm due to a lower transparency of the doped Ag film than that of ITO. However, the EQE enhancement from 580 to 870 nm is evident, which contributes to a large increase in the photocurrent. Quantitatively, for the 7 nm Al-doped Ag based device, the reduction in J_{sc} due to the decrease of EQE in the range of 370-580 nm is estimated to be 0.6 mA cm^{-2}, while the enhancement in J_{sc} contributed by the increase of EQE in the range of 580-870 nm is estimated to be 1.4 mA cm^{-2} because of the high photon density of AM1.5G solar light in this range. A total enhanced J_{sc} of 0.8 mA cm^{-2} is in good agreement with the J-V characteristics.

To further investigate the origin of the EQE enhancement in the Al-doped Ag based devices, the optical field intensity ($|E|^2$) distribution versus position and wavelength for the

ITO and 7 nm Al-doped Ag based devices is simulated (figures 3.5c and d), since light absorption and photocurrent generation in the active layer is strongly correlated with optical field intensity inside this layer. This simulation is based on the 1D transfer matrix method [77]. The incident light is launched normally into the glass substrate side and the field intensity $|E|^2$ inside the solar cell is average over p and s polarizations and normalized to the incoming field intensity. For the 7 nm Al-doped Ag based device, a resonant cavity is formed in the active layer between the reflective top Ag anode and the semi-transparent Al-doped Ag cathode, exhibiting a spectrum peak located close to the absorption edge of PBDTTT-C-T:PC70BM (in the range from 750 to 850 nm). Such a cavity effect and the resultant increase in the optical field intensity will lead to a more efficient light harvesting as the active material layer itself has a low absorption in this region. Even though the benefit of this resonance effect is reduced by the lower EQE at wavelengths below 550 nm, the higher photon flux at the longer wavelength range (600-800 nm) over-compensates the loss in the lower wavelength range (Figure 3.5a).

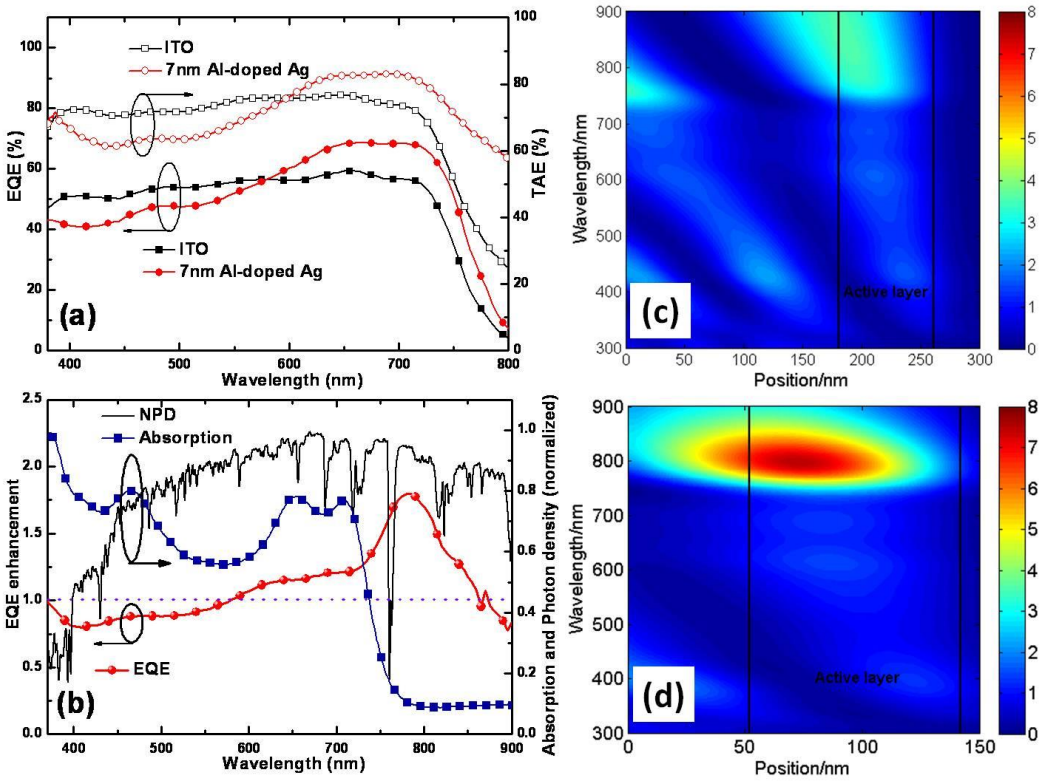

Figure 3.5: (a) TAEs and EQEs of ITO and 7 nm Al-doped Ag based devices. (b) EQE and TAE enhancements of 7 nm Al-doped Ag based devices over ITO based ones, as well as the normalized absorption spectrum of the PBDTTT-C-T:PC70BM active layer and normalized photon density of the AM1.5G solar light. Simulation of the optical field intensity ($|E|^2$) distribution versus position and wavelength in (c) an ITO based device and (d) a 7 nm Al-doped Ag based device, where the enhanced optical field in the active layer around 800 nm is responsible for the measured EQE enhancement at the same wavelength range shown in figure 3.5b.

Finally, the ultra-thin film deposited on a flexible PET film shows excellent mechanical stability as compared to ITO on PET. The ITO based device degraded very fast with an increased bending time and stopped operating after 40 times of bending (Figure 3.6a). On the contrary, the 7 nm Al-doped Ag based device has a much more stable performance even after 120 times of bending, showing no obvious performance degradation. The film sheet resistance increased by only 10% after 1000 times of bending (Figure 3.6b).

The robustness of Al-doped Ag film against time is another unique and important feature. The sputtered films were simply kept at atmosphere without any protection layer, and no obvious change in color and transparency was observed even after more than 1 month. Long-time stability of electrode is crucial in practical applications of organic electronics. Figure 3.7 shows the dependence of the PCEs of the Al-doped Ag based devices on the storage time. The result indicates that devices with the Al-doped Ag films as electrodes have a stable performance with time.

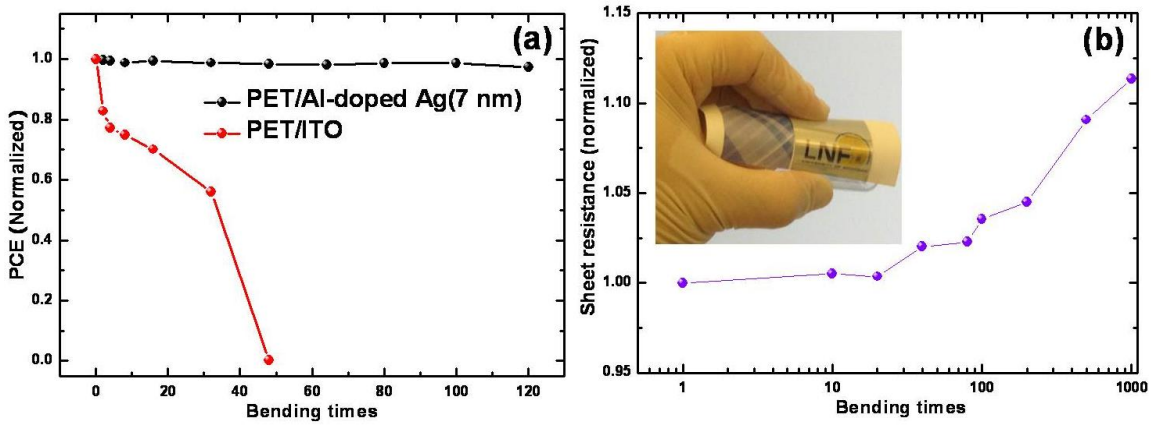

Figure 3.6: (a) Bendability test of the devices with PET/ITO and PET/Al-doped Ag as electrodes. (b) Sheet resistance of Al-doped Ag film versus bending times. The inset shows a photo of Al-doped Ag film on a PET substrate.

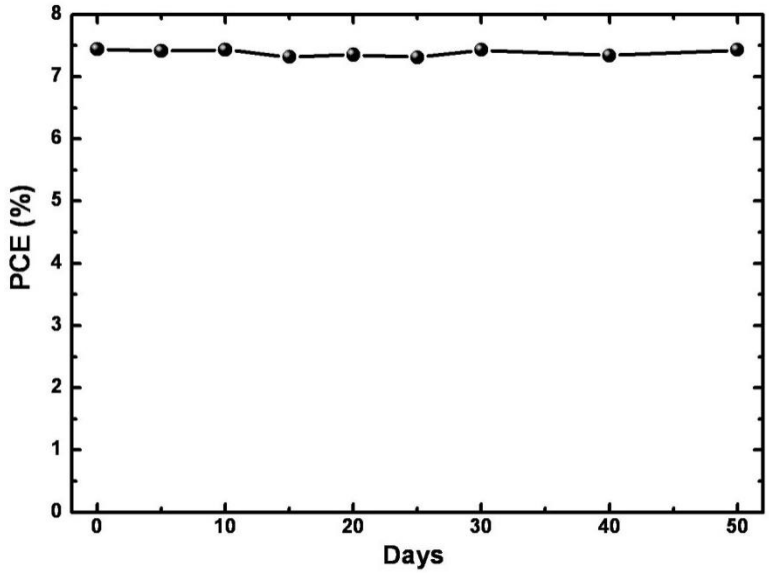

Figure 3.7: Dependence of the PCE of the device with an Al-doped Ag film as the electrode on the storage time.

3.4 Conclusions

This chapter presents Al-doped Ag film's application in OPVs as transparent electrodes, producing performance-enhanced devices compared to ITO-based ones. The PCE of the 7 nm Al-doped Ag based device is 7.44%, while that of the ITO based device is 6.87%. Such an improvement mainly originates from the photocurrent enhancement by the strong resonant light trapping effect in the polymer active layer at its absorption spectrum edge, as well as the high photon density of the solar spectrum in this range. The Al-doped Ag electrode shows excellent flexibility and stability compared with its ITO counterpart. This study has demonstrated that Al-doped Ag film is a promising and effective alternative to current transparent conducting electrodes by its simple deposition process, close-to-flat and high transmittance, high conductivity, and friendly device integration.

Chapter 4

Organic Solar Cells Using Al-doped Ag Films as Transparent Conductors: Improved Designs

4.1 Introduction

The ultra-thin, smooth, and low-loss Al-doped Ag films work well as semi-transparent conductors for organic solar cells. Devices with Al-doped Ag electrodes show better power conversion efficiencies than those with ITO electrodes. This is due to the fact that the reflection from a thin metal film increases towards longer wavelengths. Such an increased reflection, together with the high reflection from the top thick anode in the OPV devices, can be advantageously utilized to form a Fabry-Perot optical cavity to improve the optical absorption by the thin organic active layer in the long wavelength regime (resonant light harvesting). This strategy enhances the power conversion efficiencies (PCEs) of OPVs.

However, the EQE of the Al-doped Ag based device is reduced at the short wavelength range compared to that of the ITO based device, as shown in figure 3.5a. The enhanced EQE at the longer wavelength range compensate for the reduced EQE at the shorter wavelength part, and leads to larger PCEs of Al-doped Ag based devices. Therefore, a natural question to ask will be: Is there a better way to utilize such a resonant light

harvesting effect in OPVs? To answer this question, improved designs of Al-doped Ag based transparent conductors will be investigated in this chapter.

4.2 Ultra-thin Al-doped Ag films with Ta_2O_5 wetting layers

A 6 nm thick, wetting-layer-free Al-doped Ag film can be deposited on various substrates. Here, it will be shown that a conductive and transparent Ag based film as thin as 4 nm can be achieved by adding a wetting layer (Ta_2O_5) underneath the Al-doped Ag. Dielectric materials, such as MoO_x [6] and TeO_2 [78], are known to promote a continuous Ag film formation. Extending this approach, Ta_2O_5 is employed in this work as a wetting layer to further reduce the percolation threshold of Al-doped Ag films. Compared to a 6 nm Al-doped Ag film directly deposited on fused silica substrates, the insertion of Ta_2O_5 layer allows a continuous film formation down to 4 nm. Figures 4.1a and b show the SEM images of a 4 nm and 5 nm Al-doped Ag film on a 10 nm Ta_2O_5 layer. The film is continuous and has a uniform morphology, which is also confirmed by the AFM images in Figure 4.1d (for a 4 nm film). The RMS roughness values of the 4 nm and 5 nm Al-doped Ag films on Ta_2O_5 are 0.76 nm and 0.72 nm, respectively (Figure 5.2). In sharp contrast, a 7 nm pure Ag on Ta_2O_5 is still discontinuous and consists of isolated islands (Figure 4.1c).

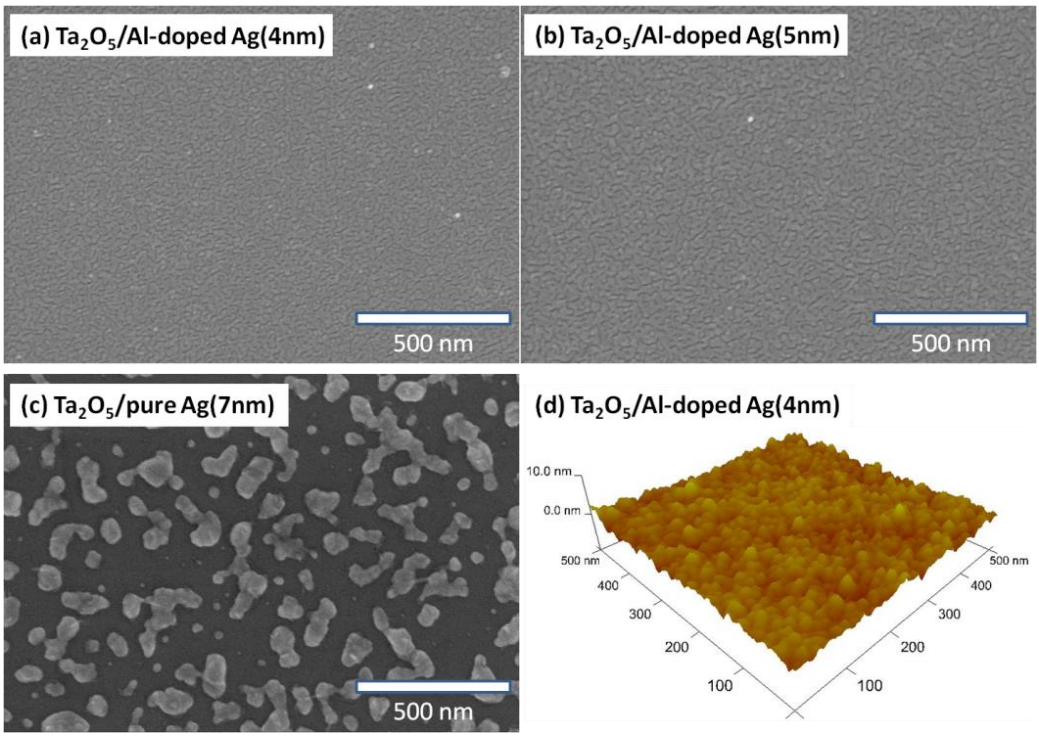

Figure 4.1: SEM images of (a) Ta_2O_5/Al-doped Ag (4 nm), (b) Ta_2O_5/Al-doped Ag (5 nm), (c) Ta_2O_5/pure Ag (7 nm), and (d) AFM image of Ta_2O_5/Al-doped Ag (4 nm) with an RMS roughness of 0.76 nm. All films are deposited on fused silica substrates.

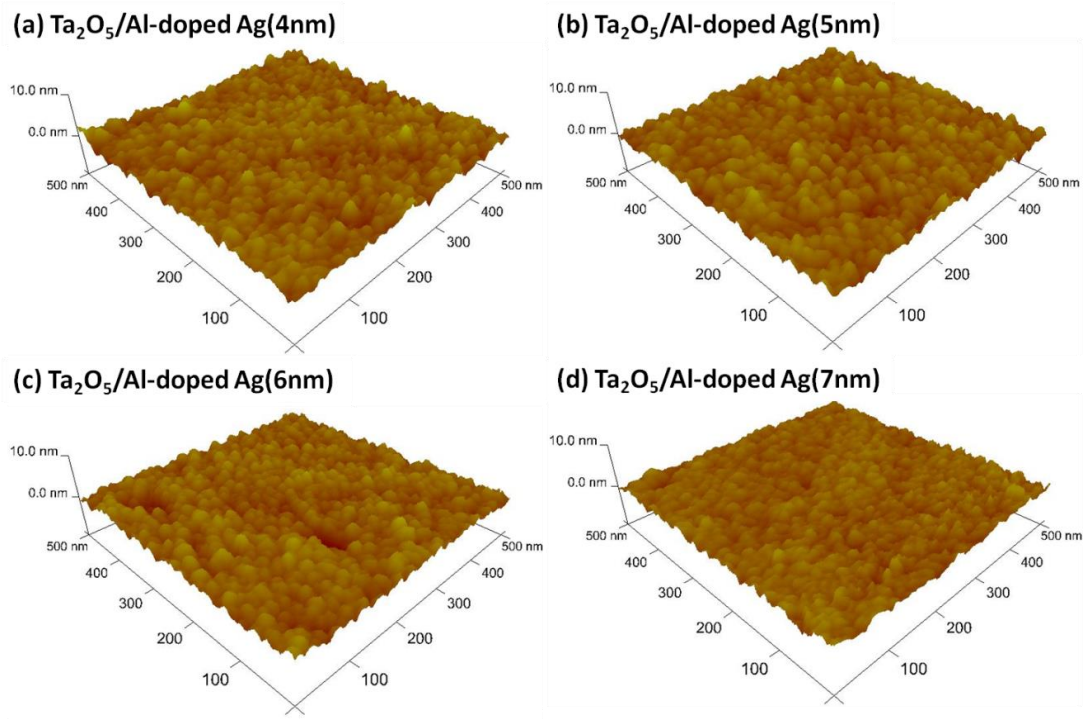

Figure 4.2: Tapping mode AFM images of (a) Ta_2O_5/Al-doped Ag (4 nm), (b) Ta_2O_5/Al-doped Ag (5 nm), (c) Ta_2O_5/Al-doped Ag (6 nm), and (d) Ta_2O_5/Al-doped Ag (7 nm), which all exhibit RMS roughness values less than 1 nm.

Figure 4.3a shows the transmittance spectrum of Ta_2O_5 (10 nm)/Al-doped Ag films with different Al-doped Ag layer thicknesses varying from 4 to 7 nm. Films with less than 7 nm Al-doped Ag exhibit a flat and averaged 75% transmission in the entire range. It is worthwhile to note that the 7 nm film has a higher transmission than thinner films. This is because thinner films have more defects at an early stage of continuous film formation and thereby, a higher optical loss. For the application of such ultrathin films as electrodes in OSCs, a 40 nm ZnO film as the electron transport layer (ETL) is spin-coated onto the Ta_2O_5 (10 nm)/Al-doped Ag films. Adding a ZnO layer further increases the transmittance of such electrodes over 80% in the entire spectrum, especially for the 7 nm Al-doped Ag whose

transmission is promoted to 93% at 550 nm (Fig. 4.3b). This can be explained that the ZnO layer acts as an anti-reflection coating. The sheet resistances of Ta_2O_5 (10 nm)/Al-doped Ag (4, 5, 6, and 7 nm) are 46.8, 33.8, 30.1, and 23.1 Ω/sq, respectively, which are suitable for applications in OSCs.

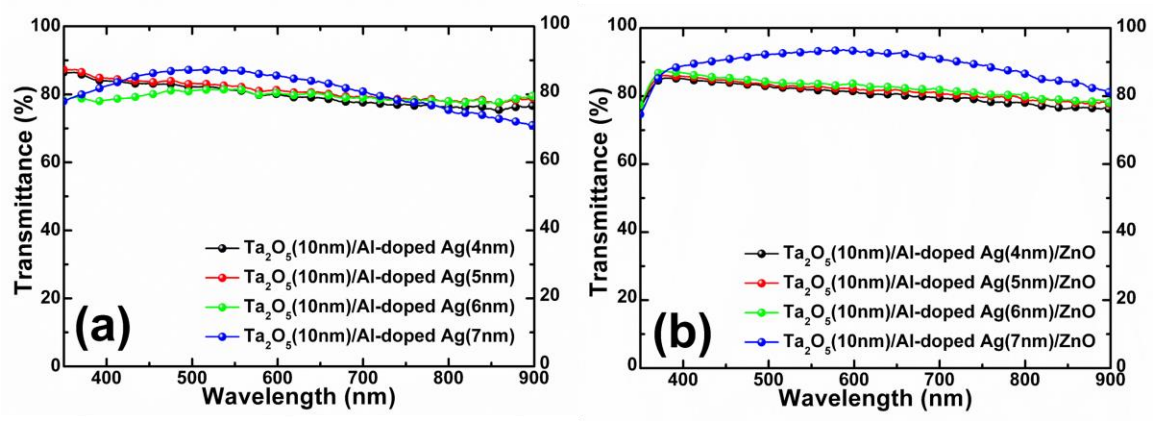

Figure 4.3: Transmission spectra of (a) Ta_2O_5/Al-doped Ag (4, 5, 6, and 7 nm), (b) Ta_2O_5/Al-doped Ag (4, 5, 6, and 7 nm)/ZnO (40 nm). All films are deposited on fused silica substrates.

An ultra-thin Ag film down to 4 nm is already applicable in making high-performance solar cells. Figure 4.4a shows the J-V characteristic of the device with Ta_2O_5/Al-doped Ag (4 nm) as the electrode and poly[4,8-bis(5-(2-ethylhexyl)thiophen-2-yl)benzo[1,2-b;4,5-b']dithiophene-2,6-diyl-alt-(4-(2-ethylhexanoyl)-thieno[3,4-b]thiophene-)-2-6-diyl)] (PBDTTT-C-T):[6,6]-phenyl C71-butyric acid methyl ester (PC70BM) as the photoactive layer. The device geometry is shown in Figure 4.5d. The device with a 4 nm Al-doped Ag has a PCE of 7.11% with a short-circuit current density (J_{sc}) = 14.3 mA/cm^2, open-circuit voltage (V_{oc}) = 0.79 V, and fill factor (FF) = 62.9%. Its corresponding EQE spectrum is shown in Figure 4.4b, exhibiting a broad spectral response with a peak EQE of 62% at 655

nm. To the best of the author's knowledge, it is the thinnest Ag layer as electrode in efficient OSCs. This result indicates that a 4 nm Al-doped Ag film is continuous and conductive to produce identical V_{oc} to the ITO control device and also a reasonable FF.

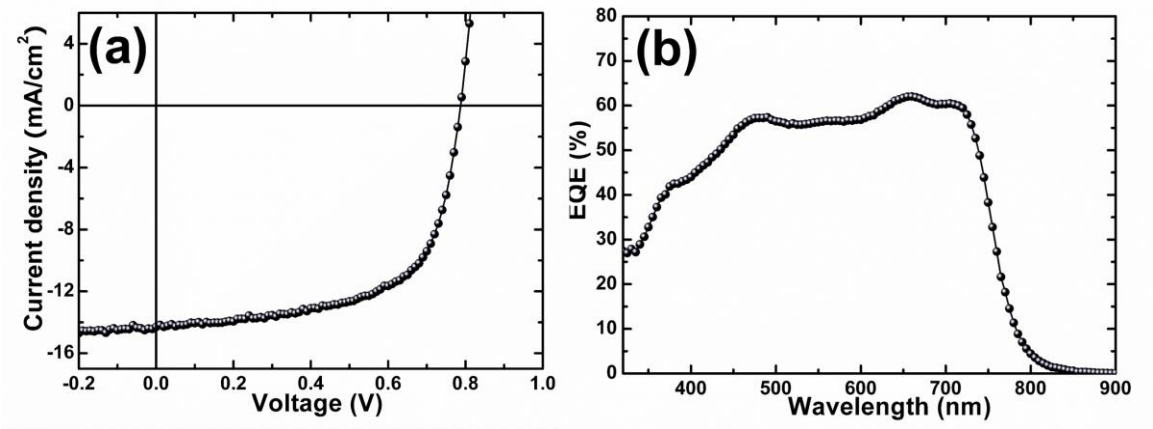

Figure 4.4: (a) J-V characteristic and (b) EQE spectrum of solar cells based on electrodes with Ta_2O_5/Al-doped Ag (4 nm).

4.3 Resonant light harvesting with Ta_2O_5/Al-doped Ag electrodes

Next, it will be demonstrated that the PCE of an OSC device can be optimized through resonant light harvesting by adjusting the thickness of the Ta_2O_5 layer. Although PCE is highly correlated to light absorption in the active layer, increasing its thickness is a straightforward way to increase the light absorption, but not always an efficient approach to boost PCE. This is due to the short exciton diffusion length and low carrier mobility in organic semiconductors, which result in high recombination rates of photo-generated charge carriers during their transport towards the electrodes. The above physical limitations indicate that a relatively thin photoactive layer is desired, as long as the light absorption

efficiency is not compromised at the same time [79-82]. To achieve this goal, light trapping plays an important role in obtaining a strong light absorption without relying on increasing the thickness of the photoactive layer. By choosing a proper thickness of the Ta_2O_5 layer, an optical field resonance is formed between top and bottom electrodes, which contributes to the enhanced light field inside the active layer.

The transmittance spectra of Ta_2O_5/Al-doped Ag (7 nm) with varying Ta_2O_5 thicknesses are shown in Figure 4.5a. It can be seen that the transmittance peak shifts towards the longer wavelength with the increase of Ta_2O_5 thickness from 5 to 30 nm. Beyond the peak, the transmittance gradually decreases with wavelength due to the increase of reflection from the Al-doped Ag film in the near infrared (NIR) range, as is true for good metals. Coating a ZnO layer on top of the Al-doped Ag further increases its transmittance, as shown in Figure 4.5b. The transmittance becomes higher and flatter in the range of 400-800 nm. For example, the maximum transmittance is 96% at 550 nm for a Ta_2O_5 (15 nm)/Al-doped Ag (7 nm)/ZnO (40 nm) film. Figure 4.5c shows the comparison of optical transmittance (at 550 nm) versus sheet resistance of this work (Ta_2O_5/Al-doped Ag/ZnO) to other reported works based on thin Ag planar films or nanostructures, where this work shows a better or comparable performance.

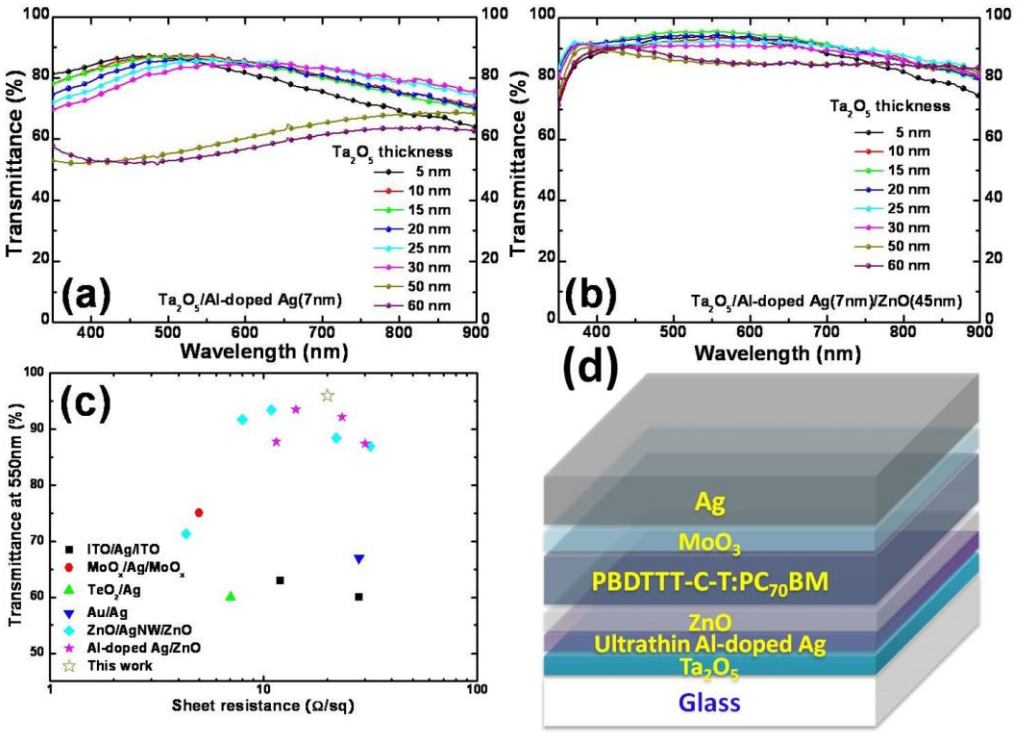

Figure 4.5: Transmission spectra of (a) Ta_2O_5 (x nm)/Al-doped Ag (7 nm) and (b) Ta_2O_5 (x nm)/Al-doped Ag (7 nm)/ZnO (40 nm) with varying thickness of the Ta_2O_5 layer. (c) Comparison of optical transmittance (at 550 nm) versus sheet resistance of Ta_2O_5/Al-doped Ag/ZnO electrode with other reported results based on Ag planar films/nanostructures: ITO/Ag/ITO [65], MoO_x/Ag/MoO_x [7], TeO_2/Ag [78], Au/Ag [83], ZnO/AgNW/ZnO [68], Al-doped Ag/ZnO [84], in which all selected data are based on their applications in optoelectronic devices. (d) Schematic of the OSC devices with Ta_2O_5/Al-doped Ag as the electrode.

To evaluate the effect of Ta_2O_5/Al-doped Ag electrode on the resonant light harvesting, solar cells using PBDTTT-C-T:PC70BM were built up on such electrodes. As a comparison, ITO is used as the electrode in the control device. Figure 4.5d shows the device geometry using either ITO or Ta_2O_5/Al-doped Ag electrodes. A 40 nm ZnO layer was first coated on all electrodes as ETL, and a 70 nm PBDTTT-C-T:PC70BM layer was spin-

coated subsequently with the same solution concentration and spinning speed. Finally, the top electrode was finished with 10 nm MoO_x and 100 nm Ag.

Figure 4.6a shows the comparison of the J-V characteristics of devices whose electrodes are either ITO or Ta_2O_5/Al-doped Ag (7 nm) with a varying thickness of the Ta_2O_5 layer. Their main photovoltaic parameters are tabulated in Table 4.1. The ITO-based device has a PCE of 8.22% with a J_{sc} = 15.54 mA cm^{-2}, V_{oc} = 0.79 V, and FF = 66.9%. Device built on Ta_2O_5 (15 nm)/Al-doped Ag (7 nm) has a PCE of 8.57% with a J_{sc} = 16.92 mA cm^{-2}, V_{oc} = 0.79 V, and FF = 64.1%. All devices have identical V_{oc}, indicating that no voltage loss occurs at either the anode or the cathode electrodes for both ITO and Ta_2O_5/Al-doped Ag (7 nm) with the help of interfacial layers: MoO_x and ZnO. Meanwhile, since Ta_2O_5 layer is the outmost layer of the entire device and only works as an optical spacer rather than a charge transport layer, changing its thickness would not affect the electrical performance of the devices. The FFs of ITO and Ta_2O_5/Al-doped Ag (7 nm) based devices are comparable, due to good contacts of ITO and Ta_2O_5/Al-doped Ag (7 nm) with the ZnO layer. Therefore, the increased PCE of Ta_2O_5/Al-doped Ag based devices primarily results from the enhancement of J_{sc}.

Figure 4.6b shows the external quantum efficiencies (EQEs) of the devices with ITO and Ta_2O_5/Al-doped Ag (7 nm) with varying thicknesses of the Ta_2O_5 layer. Their spectral responses reflect the capability of converting photons to electrons at a certain wavelength. For instance, the EQE-integrated J_{sc} for the ITO based device is 14.8 mA/cm^2, while that

for Ta_2O_5 (15 nm)/Al-doped Ag (7 nm) based device is 15.8 mA/cm^2. The spectral response of Ta_2O_5/Al-doped Ag (7 nm) based devices is different from that of ITO based devices, where the former exhibits a significant enhancement in certain wavelength ranges over the ITO based devices. Specifically, the EQE enhancements for selected thicknesses of the Ta_2O_5 layer (5, 15, 20, 25, 30, and 50 nm) are shown in Figure 4.6c. For all cases excluding the 50 nm Ta_2O_5-based device, Ta_2O_5/Al-doped Ag (7 nm) based devices have two enhanced EQE regimes compared to ITO based ones. With the increase of the Ta_2O_5 layer thickness, the enhancement at the shorter wavelength gets more prominent, while the other one at the longer wavelength becomes weaker. It is worth noting that the 15 nm Ta_2O_5 device obtains a consistently enhanced EQE from 430 to 780 nm compared to the ITO based device, leading to the strongest photocurrent enhancement and the highest PCE among all devices.

In order to examine the potential application of this electrode on flexible substrates, the Ta_2O_5/Al-doped Ag/ZnO film was deposited on flexible PET substrates. The radius of curvature for bending test is around 5 mm. As shown in Figure 4.6d, the performance of ITO based device significantly degraded each time when it was bent, and stopped operating after 60 times of bending. In contrast, the Ta_2O_5/Al-doped Ag based device has a stable performance even after 150 bending cycles.

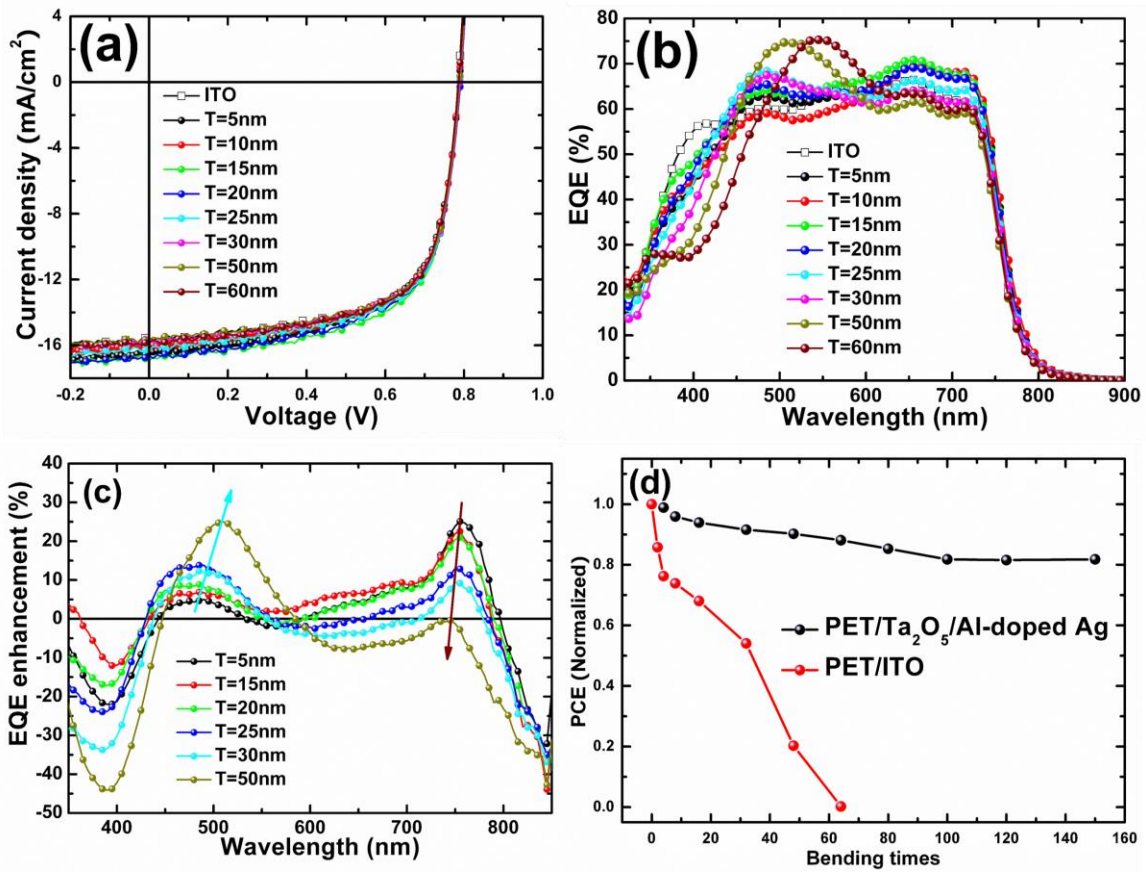

Figure 4.6: (a) J-V characteristics and (b) EQE spectra of ITO and Ta_2O_5 (x nm)/Al-doped Ag (7 nm) electrode based OPVs. (c) EQE enhancement of Ta_2O_5 (5, 15, 20, 25, 30, and 50 nm)/Al-doped Ag (7 nm) based OPVs over ITO based ones. (d) Bendability test of the devices with PET/ITO and PET/Ta_2O_5 (15 nm)/Al-doped Ag (7 nm) as electrodes.

Table 4.1: Summary of performance metrics of the devices with ITO and Ta_2O_5/Al-doped Ag (7 nm) with varying thicknesses of Ta_2O_5 layer, which are obatined from 6 devices for each condition.

	J_{SC} [mA cm^{-2}]	V_{oc} [V]	FF [%]	PCE [%]
ITO control	15.54 (±0.20)	0.79 (±0.01)	66.9 (±0.4)	8.22 (±0.18)
Ta_2O_5= 5 nm	16.43 (±0.24)	0.79 (±0.01)	63.2 (±0.3)	8.20 (±0.20)
Ta_2O_5= 10 nm	16.17 (±0.15)	0.79 (±0.01)	64.8 (±0.5)	8.28 (±0.19)
Ta_2O_5= 15 nm	16.92 (±0.19)	0.79 (±0.01)	64.1 (±0.6)	8.57 (±0.22)
Ta_2O_5= 20 nm	16.63 (±0.20)	0.79 (±0.01)	64.4 (±0.3)	8.46 (±0.18)
Ta_2O_5= 25 nm	16.40 (±0.10)	0.79 (±0.01)	65.0 (±0.5)	8.42 (±0.17)
Ta_2O_5= 30 nm	15.75 (±0.16)	0.79 (±0.01)	66.3 (±0.2)	8.25 (±0.16)
Ta_2O_5= 50 nm	15.68 (±0.15)	0.79 (±0.01)	66.3 (±0.1)	8.21 (±0.15)
Ta_2O_5= 60 nm	15.81 (±0.23)	0.79 (±0.01)	66.3 (±0.2)	8.28 (±0.21)

To verify the origin of the EQE enhancement in Ta_2O_5/Al-doped Ag (7 nm) based devices, the optical field intensity ($|E|^2$) distribution versus position and wavelength is simulated using the 1D transfer matrix method, since light absorption and photocurrent generation in the active layer are strongly correlated with the optical field intensity. The light is incident normally onto the glass substrate and the optical field intensity $|E|^2$ inside the solar cell is normalized to the incoming field intensity. The field intensity profiles inside ITO based device and Ta_2O_5 (15 nm)/Al-doped Ag (7 nm) based one are shown in Figures 4.7a and b. There is a strong field enhancement ranging from 750 to 850 nm in the Ta_2O_5 (15 nm)/Al-doped Ag (7 nm) based device, and a weak field enhancement between 500 and 650 nm, in correspondence with the measured EQE enhancement. When the thickness of Ta_2O_5 layer increases from 5 to 50 nm, the resonance at the longer wavelength regime (750 to 850 nm) gets weaker, while the resonance at the shorter wavelength regime (500 to 650

nm) becomes stronger (Figures 4.7c and d). This trend is also consistent with the measured EQE. It is worth mentioning that the optical field distribution is modulated by solely varying the thickness of the Ta_2O_5 layer, which is at the outmost of the entire device and does not affect any charge transport or collection. Thereby, there is no limit in the Ta_2O_5 layer thickness or any requirement on the modification of other layers in the device, making this approach universal and easy-to-apply.

To further demonstrate the generality of this approach, devices using Ta_2O_5/Al-doped Ag as electrodes but with a thinner active layer (50 nm) were fabricated. Similarly, by solely adjusting the thickness of the Ta_2O_5 layer, the device performance can be optimized and improved as compared to the ITO control device. The measured parameters are listed in Figure 4.8. The ITO-based device with a 50 nm active layer has a PCE of 5.92% with a J_{sc} = 11.35 mA cm^{-2}, V_{oc} = 0.78 V, and FF = 66.9%. Device built on a Ta_2O_5 (25 nm)/Al-doped Ag (7 nm) electrode has a PCE of 6.23% with a J_{sc} = 11.96 mA cm^{-2}, V_{oc} = 0.78 V, and FF = 66.8%.

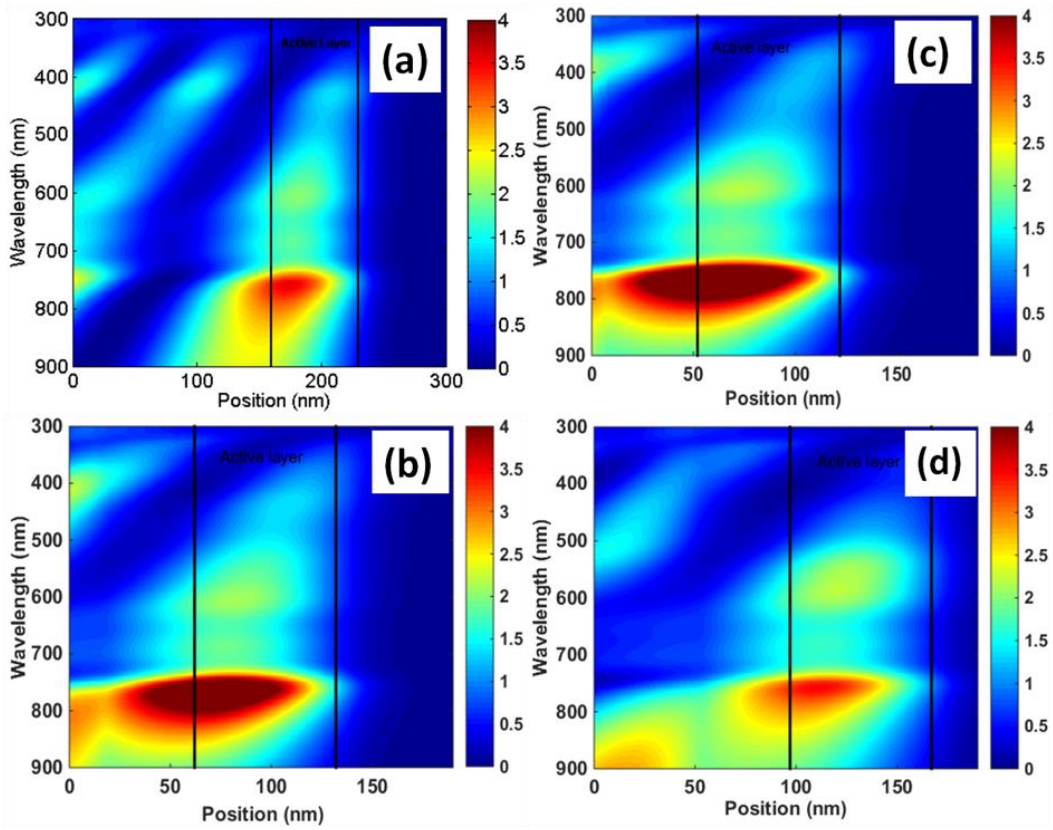

Figure 4.7: Simulation of the optical field intensity ($|E|^2$) distribution versus position and wavelength in (a) ITO based device, (b) Ta_2O_5 (15 nm)/Al-doped Ag (7 nm) based device, (c) Ta_2O_5 (5 nm)/Al-doped Ag (7 nm) based device, and (d) Ta_2O_5 (50 nm)/Al-doped Ag (7 nm) based device.

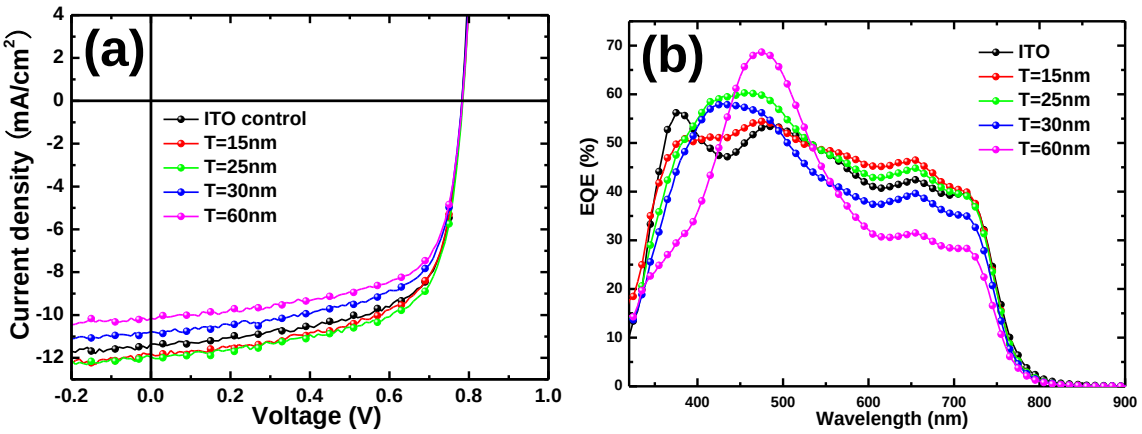

Figure 4.8: (a) J-V characteristics and (b) EQE spectra of ITO and Ta_2O_5 (x nm)/Al-doped Ag (7 nm) electrode based OPVs with a thin PBDTTT-C-T:$PC_{70}BM$ layer (50 nm).

The thickness of the semitransparent metal electrode influences the resonance effect inside the active layer in terms of both the enhanced light intensity and spectrum width, thus affecting the solar cell performance. This is demonstrated in Figure 4.9, which shows the light field intensity distribution ($|E|^2$) inside the solar cell with different Al-doped Ag electrode thicknesses. The Al-doped Ag layer thickness varies among 4 nm, 7 nm, 10 nm, and 14 nm, while the Ta_2O_5/ZnO/PBDTTT-C-T:PC70BM/MoO_x/Ag layer thicknesses are fixed as 15 nm/40 nm/70 nm/10 nm/100 nm respectively. Varying the Al-doped Ag thickness does not obviously change the resonant wavelength and location inside the device. This is because for a constructive interference to occur, the light field needs to be in phase at a certain position for a certain wavelength. The optical phase is contributed by both the propagation phase inside each layer and the reflection phase shift between layers, which are not affected too much by the slight variation of the Al-doped Ag thickness in a small range. However, varying the metal electrode thickness will change both its

reflectance and transmittance, thus affecting the enhanced field intensity as well as its spectrum width. For a thin electrode (e.g., 4 nm), the resonance has a weak peak intensity, but a broad spectrum. When the electrode film becomes thicker (e.g., 7 nm and 10 nm), the peak intensity gets stronger, but the spectrum width is compromised. If the electrode gets even thicker (e.g., 14 nm), both the peak intensity and spectrum width are reduced, and this is attributed to the relatively high loss associated with the metal electrode.

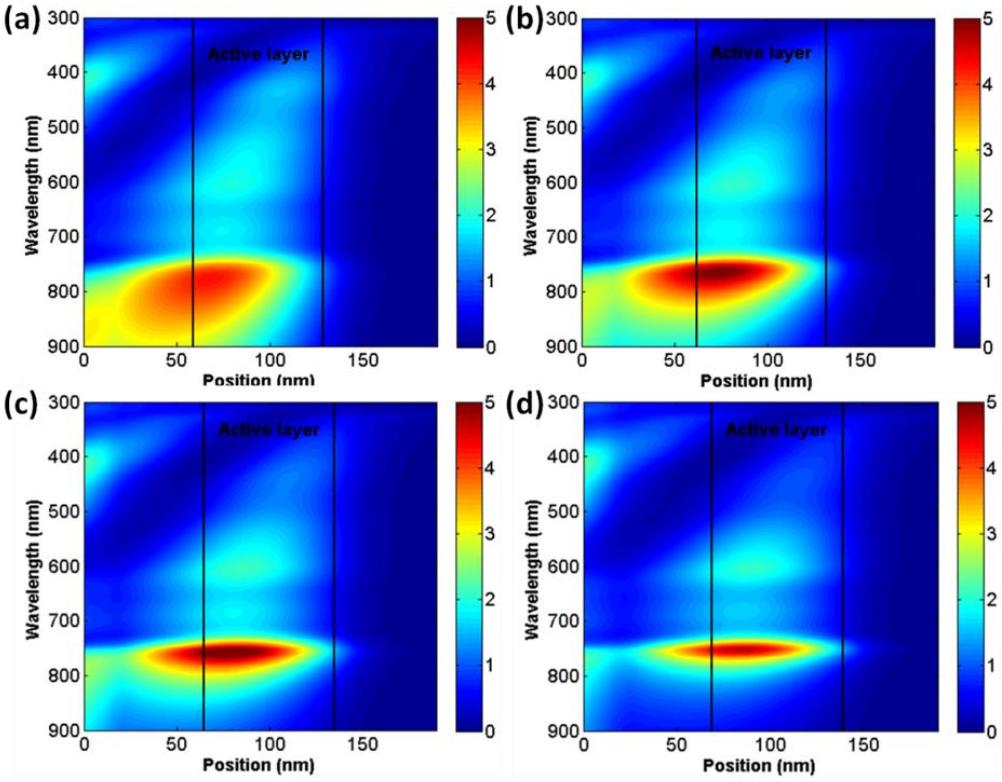

Figure 4.9: Simulation of the optical field intensity ($|E|^2$) distribution versus position and wavelength with varying Al-doped Ag electrode thicknesses at 4 nm (a), 7 nm (b), 10 nm (c), and 14 nm (d). The Ta_2O_5/ZnO/PBDTTT-C-T:PC70BM/MoO_x/Ag layer thicknesses are fixed at 15 nm/40 nm/70 nm/10 nm/100 nm respectively.

To further study the effect of Al-doped Ag electrode thickness on the device performance, the J_{sc} of solar cells with different Al-doped Ag electrode thicknesses is simulated while

keeping the other layers unchanged. A constant internal quantum efficiency is assumed for the absorbed light. Two devices with different active layer thicknesses (50 nm and 70 nm) are studied, consistent with our experimentally demonstrated ones. In each case, the Ta_2O_5 layer thickness is chosen in correspondence to the device configurations with maximal EQEs (25 nm Ta_2O_5 for the device with a 50 nm active layer and 15 nm Ta_2O_5 for the device with a 70 nm active layer). The normalized J_{sc} is plotted in Figure 4.10. For the device with a 70 nm active layer, the simulated current stays basically flat for a thin Al-doped Ag film (<8 nm), with a maximum value at 6 nm and then starts to drop with the increasing thickness of the metal electrode. The J_{sc} of the 50 nm active layer device has a more obvious dependence on the Al-doped Ag thickness, with a maximum value at 8 nm. Therefore, a thin, smooth, and low-loss metal electrode is advantageous for the resonant light harvesting in OSCs.

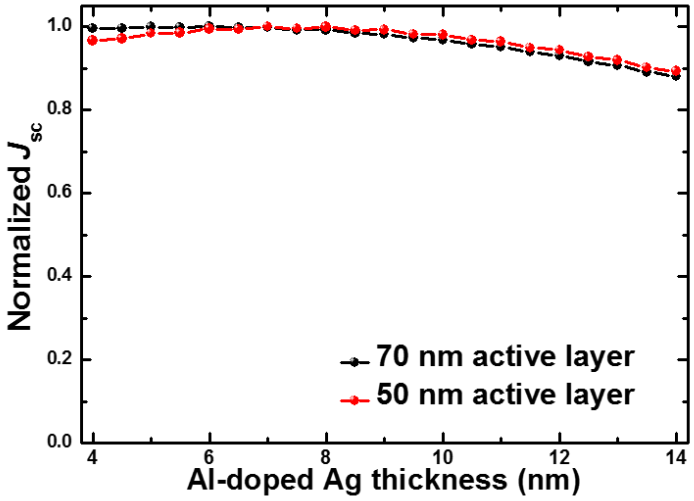

Figure 4.10: Simulated J_{sc} of the devices with varying thicknesses of Al-doped Ag layer from 3 nm to 14 nm and fixed other layer thicknesses.

4.4 Highly transparent TiO_2/Al-doped Ag/TiO_2/MgF_2 electrode

In order to be employed in universal device configurations, semitransparent conductors should have as high a transmission as possible. One strategy to further increase the transmission (reduce reflection) of a thin metal film is to employ a dielectric-metal-dielectric (DMD) structure, whose schematic is plotted in figure 4.11a. An ultra-thin Al-doped Ag film is sandwiched between two titanium dioxide (TiO_2) layers, and an additional layer of magnesium fluoride (MgF_2) is deposited on top of the upper TiO_2 layer to further suppress the reflection. By fixing the Al-doped Ag layer thickness, and adjusting the TiO_2 and MgF_2 layer thicknesses, an optimized DMD stack of 50 nm TiO_2/7 nm Al-doped Ag/ 40 nm TiO_2/100 nm MgF_2 provides both a high and flat transmittance over the visible and near IR range (400 nm to 1000 nm), giving an averaged transmittance of 92.4% (figure 4.11c). Such a transmission enhancement is induced by multiple optical resonances within the dielectrics. To show this, the net phase accumulation of each dielectric layer in the DMD structure of 50 nm TiO_2/7 nm Al-doped Ag/40 nm TiO_2/100 nm MgF_2 is plotted in figure 4.12. The net phase accumulation includes both the two reflection phase shifts from the two interfaces, as well as the propagation phase through the dielectric layer. The transmission is enhanced (reflection is thus suppressed) by the resonances within the dielectrics, which are indicated by the circles and occur when the net phase shift is equal to multiple times of 2π radians. The overlapped multiple resonances within every dielectric layer contribute to the broadband enhancement of transmission.

The measured spectrum of the fabricated structure is plotted in figure 4.11d, in close correspondence with simulation. The pictures of a bare fused silica substrate (left side) and a transparent conductor based on a 7 nm Al-doped Ag film (right side) are shown in figure 4.11b, both of which have similar appearances.

It is worth noting that such a DMD design also applies to thicker Al-doped Ag films; however, due to the increased absorption associated with thicker metal films, the optimized transmission is reduced (figure 4.11c). For example, for a 10 nm Al-doped Ag, the optimized structure of 40 nm TiO_2/10 nm Al-doped Ag/35 nm TiO_2/70 nm MgF_2 provides an averaged transmittance of 87.4% from 400 nm to 1000 nm. The transmission is even lower for structures with 13 nm and 16 nm Al-doped Ag films (averaged transmittance of 80.1% and 71.7% respectively).

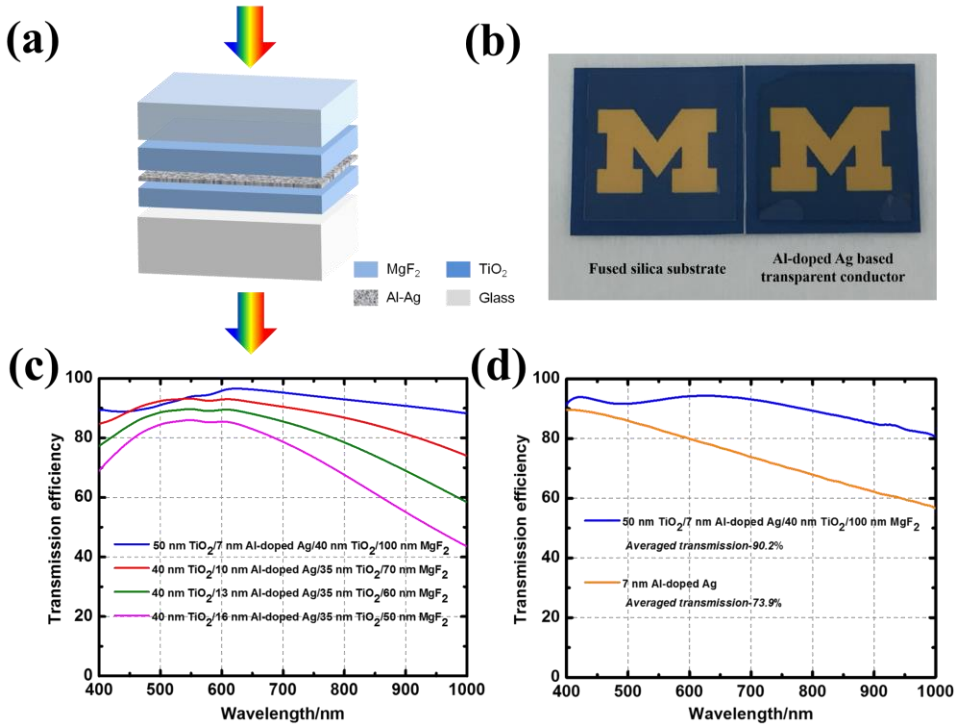

Figure 4.11: Transparent conductor based on Al-doped Ag films. (a) Schematic drawing of an Al-doped Ag based transparent conductor using dielectric/metal/dielectric (DMD) configuration. (b) Left: picture of a bare fused silica substrate; Right: picture of an Al-doped Ag based transparent conductor (50 nm TiO_2/7 nm Al-doped Ag/40 nm TiO_2/100 nm MgF_2). (c) Simulated transmission spectra of transparent conductors with different Al-doped Ag layer thickness. For each Al-doped Ag layer thickness, the thicknesses of TiO_2 and MgF_2 layers are adjusted to achieve optimized transmission efficiency from 400 nm to 1000 nm. (d) Measured transmission spectrum of transparent conductor (50 nm TiO_2/7 nm Al-doped Ag/40 nm TiO_2/100 nm MgF_2). The transmission through a 7 nm Al-doped Ag film is also plotted as a comparison.

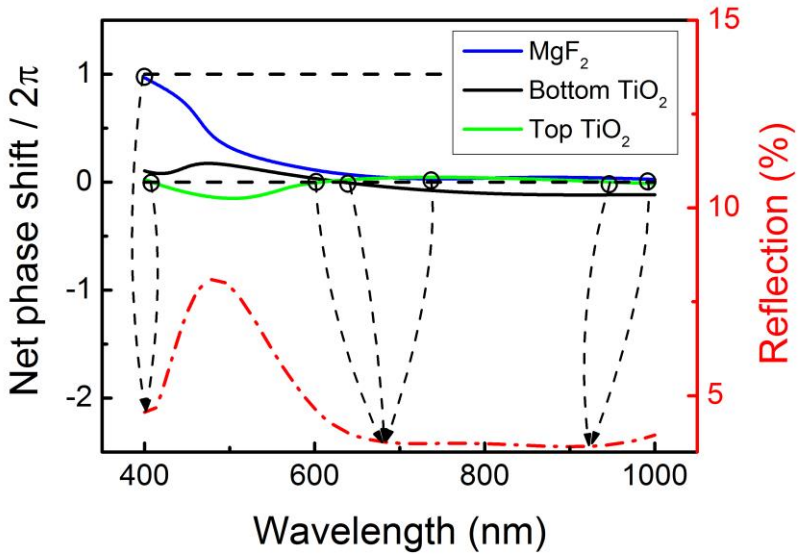

Figure 4.12: The net phase accumulation of each dielectric layer in the DMD transparent conductor consisting of 50 nm TiO_2/7 nm Al-doped Ag/40 nm TiO_2/100 nm MgF_2.

4.5 Conclusions

This chapter presents improved designs of transparent conductors based on Al-doped Ag films. With the aid of the Ta_2O_5 wetting layer, ultra-thin Al-doped Ag films down to 4 nm are obtained, and they work as efficient transparent conductors in organic solar cells. In addition, the Ta_2O_5 layer functions as an optical spacer to tune the optical field distribution in the entire solar cell without the need to change the other layers' geometries, locating the optical cavity resonance inside the active layer. The light harvesting of the active layer is enhanced in a certain range of its absorption spectrum while the absorption in the rest of the spectrum is not sacrificed (due to improved photon management), leading to enhanced PCEs. Ta_2O_5/Al-doped Ag films act as a high-performance electrode for OSCs with high transparency, low resistance, good mechanical flexibility, and improved photon

management capability. In the end, a highly transparent TiO_2/Al-doped Ag/TiO_2/MgF_2 electrode is designed and fabricated. It has an averaged transmittance of 92.4% over the visible and near-IR range (400 nm to 1000 nm), and is suitable to be employed as an ITO-free electrode in universal device configurations

Chapter 5

Organic Light Emitting Diodes Using Al-doped Ag Films as Transparent Conductors

5.1 Introduction

In previous chapters, thin doped Ag films have been investigated as high-performance transparent conductors in organic solar cells. They provide a high optical transmittance, good electrical conductivity, and great mechanical flexibility. With the aid of reflection from thin Ag films, a resonance enhanced optical field can be formed inside the photo-active layer, which further promotes the device's power conversion efficiency (resonant light harvesting). In this chapter, thin doped Ag films will be investigated as the transparent conductors in organic light emitting diodes (OLEDs).

Currently, one of the most widely used transparent conductors for OLEDs is indium tin oxide (ITO). However, it has several limitations. Scarcity of the Indium element renders ITO a high-cost material. Beside, ITO is brittle and has a poor mechanical flexibility, which limits its applications in flexible devices. Moreover, ITO usually requires a high temperature processing (e.g. post-annealing after deposition), which constrains its applications in OLEDs, especially as the top electrodes.

Another drawback of ITO-based OLEDs is the limited out-coupling efficiency. For OLEDs fabricated on glass substrates coated with ITO, only a small fraction of the emitted photons actually exit the device. Most of the emitted light will be trapped inside the OLED as waveguide modes due to total internal reflections at the interfaces between layers. This is because of the refractive index mismatch between the glass substrate (n~1.5), ITO (n~1.8), organic layers (n~1.7), and air (n=1).

Due to the above mentioned limitations of ITO, various alternative transparent conductors have been intensively researched, including thin metal films [85, 86], metallic nano-/micro-structures [87, 88], conductive polymers [89, 90], and carbon-based materials [55, 91, 92]. Among them, thin metals offer the advantages of low-cost, great optical transmittance, good electrical conductivity, and large-area uniformity.

5.2 ITO-based devices

The geometry of a conventional OLED investigated in this work is shown in figure 5.1. It has the following structure: glass substrate/ITO/PEDOT/Super yellow (SY)/ZnO/Al. The thicknesses of ITO, SY, and Al layers are fixed as 150 nm, 60 nm, and 100 nm, respectively. SY is the light emitting layer, with a central emission wavelength of 600 nm. In the ITO-based OLED, the emitted light with a parallel wave-vector ($k_{\parallel}$) smaller than the free-space wave-vector (k_0) will be able to propagate through all layers and exit into the air (air mode); For emitted light with a parallel wave-vector ($k_{\parallel}$) satisfying: $k_0 < k_{\parallel} < n_{glass} * k_0$, it will be trapped in the glass substrate (substrate mode); For emitted light with a parallel wave-

vector ($k_{\parallel}$) satisfying: $n_{glass} * k_0 < k_{\parallel} < n_{ITO}(n_{organic}) * k_0$, it will be trapped in the ITO and organic layers (ITO/organic mode); For emitted light with an even larger parallel wave-vectors: $k_{\parallel} > n_{ITO}(n_{organic}) * k_0$, they will be confined in the metal/dielectric interface as the surface plasmon polariton (SPP) wave (surface plasmon mode).

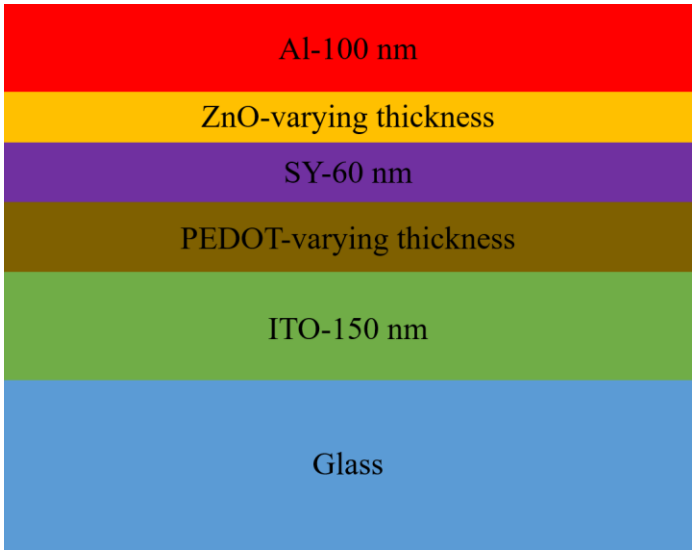

Figure 5.1: Schematic drawing of the OLED structure.

In order to enhance the out-coupling efficiency of OLED, a larger portion of the emitted photon energy needs to go to the air mode. The out-coupling optimization is conducted using the classical oscillating dipole model. The light emitting layer is modelled as a dipole, and its electromagnetic fields are calculated using the dyadic Green's functions. In the calculation, the dipole orientation, its location in the active layer, and frequencies of the emitted light taking are into consideration. Calculation details can be found in Ref. [93]. For the OLED in this study, the thicknesses of ZnO and PEDOT layers are adjusted for optimizing the out-coupling efficiency, while the thicknesses of ITO, doped Ag film, SY,

and Al layers are fixed as constant values. For the SY emitting layer, a horizontally-oriented dipole ratio of 2/3, and a vertically-oriented dipole ratio of 1/3 is assumed.

The calculated out-coupling efficiencies of the ITO-based device as a function of the PEDOT and ZnO thicknesses are shown in figure 5.2a. In this calculation, the dipole is assumed to be located at the center of the SY layer (a total thickness of 60 nm). The structure of glass/150 nm ITO/54 nm PEDOT/60 nm SY/24 nm ZnO/100 nm Al gives out an optimized out-coupling efficiency of 33.02 %. Figure 5.2b shows the calculated distribution of the dipole energy versus the dipole distance from the ZnO/SY interface. Unfortunately, there are about 20% of the emitted energy which goes to the ITO/organic mode, which is not easily extracted.

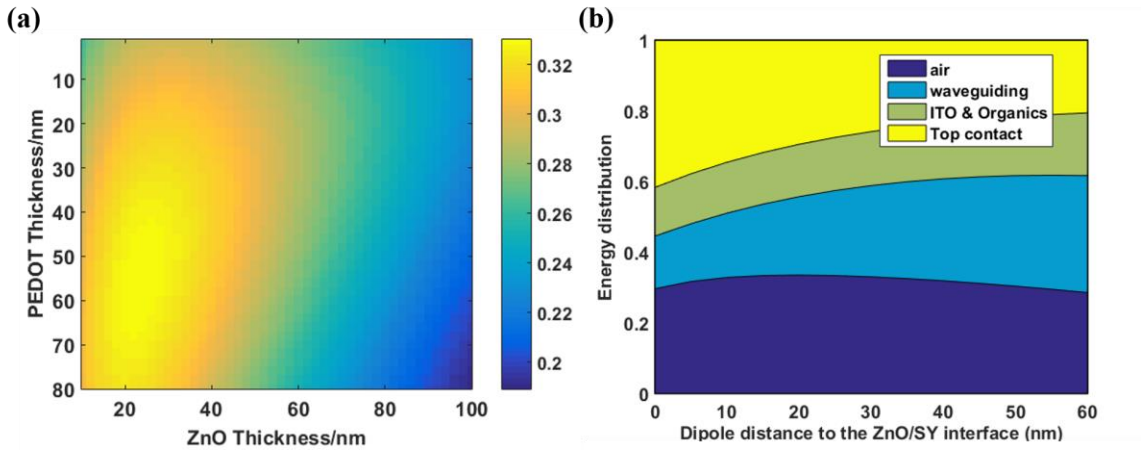

Figure 5.2: (a) Out-coupling efficiency of the ITO-based device with different thicknesses of the ZnO and PEDOT layers. (b) Energy distribution in all layers in the ITO-based device with an optimized out-coupling efficiency.

5.3 Ultra-thin doped Ag-based devices

The ITO/organic mode can be eliminated by replacing ITO with a thin Ag layer. Figure 5.3a shows the calculated out-coupling efficiencies of a 10 nm Al-doped Ag-based OLED as a function of the PEDOT and ZnO thicknesses. The structure of glass/10 nm Al-doped Ag/52 nm PEDOT/60 nm SY/26 nm ZnO/100 nm Al gives out an optimized out-coupling efficiency of 39.09 %. There is a ~18.4% enhancement in the out-coupling efficiency by simply replacing the 150 nm ITO with a 10 nm Al-doped Ag film. Figure 5.3b shows the calculated distribution of the dipole energy versus the dipole distance from the ZnO/SY interface. The ITO/organic mode has been fully eliminated.

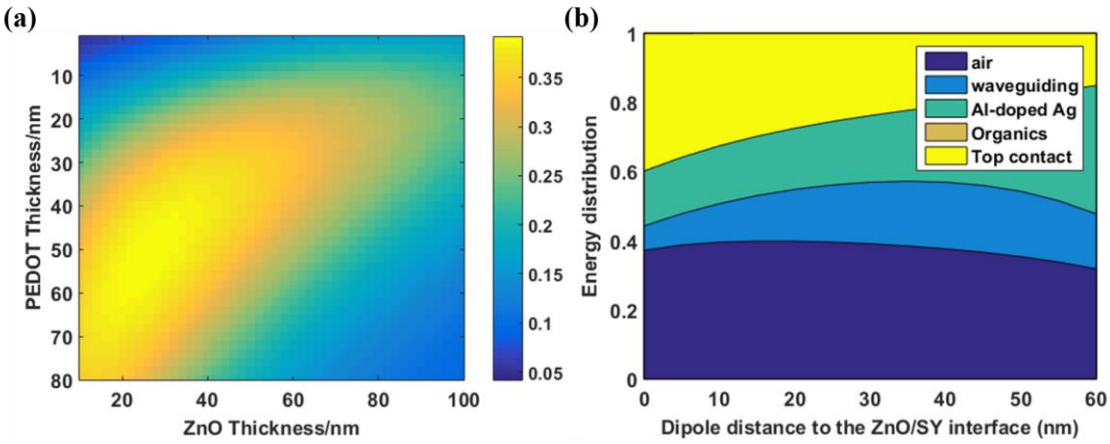

Figure 5.3: (a) Out-coupling efficiency of the 10 nm Al-doped Ag-based device with different thicknesses of the ZnO and PEDOT layers. (b) Energy distribution in all layers in the Al-doped Ag-based device with an optimized out-coupling efficiency.

The out-coupling efficiency of thin Ag-based OLEDs can be further enhanced by using thin Ag films with a lower optical loss at 600 nm, such as Cu-doped Ag. Figure 5.4a shows the calculated out-coupling efficiencies of a 10 nm Cu-doped Ag-based OLED as a

function of the PEDOT and ZnO thicknesses. The structure of glass/10 nm Al-doped Ag/54 nm PEDOT/60 nm SY/26 nm ZnO/100 nm Al gives out an optimized out-coupling efficiency of 41.61 %. Figure 5.4b shows the calculated distribution of the dipole energy versus the dipole distance from the ZnO/SY interface.

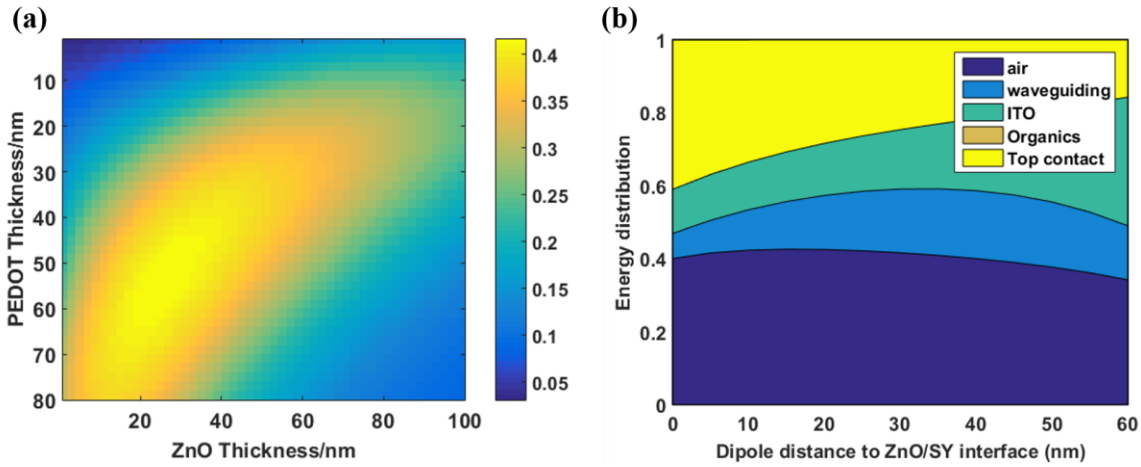

Figure 5.4: (a) Out-coupling efficiency of the 10 nm Cu-doped Ag-based device with different thicknesses of the ZnO and PEDOT layers. (b) Energy distribution in all layers in the Cu-doped Ag-based device with an optimized out-coupling efficiency.

Similar to the resonant light harvesting effect in organic solar cells discussed in chapter 4, such a micro-cavity effect is also related to the thickness of the Ag film. A too thin film will not support a sufficiently strong cavity effect, while a too thick film induces too much absorption loss. Figure 5.5 plots the out-coupling efficiencies with different thin doped Ag film thicknesses for both Al-doped Ag- and Cu-doped Ag-based OLED. The thicknesses of the ZnO and PEDOT layers are adjusted in order to achieve the optimized out-coupling efficiency for each case with a different Ag film thickness. It can be seen that there is a dependence of the optimized out-coupling efficiency on the thickness of the thin Ag film. For the OLED structure in this study, a highest out-coupling efficiency occurs at a 10 nm

electrode thickness for both Al-doped Ag- and Cu-doped Ag-based devices. This further signifies the unique advantages of using an ultra-thin, smooth, and low-loss doped Ag films as semitransparent conductors in OLEDs.

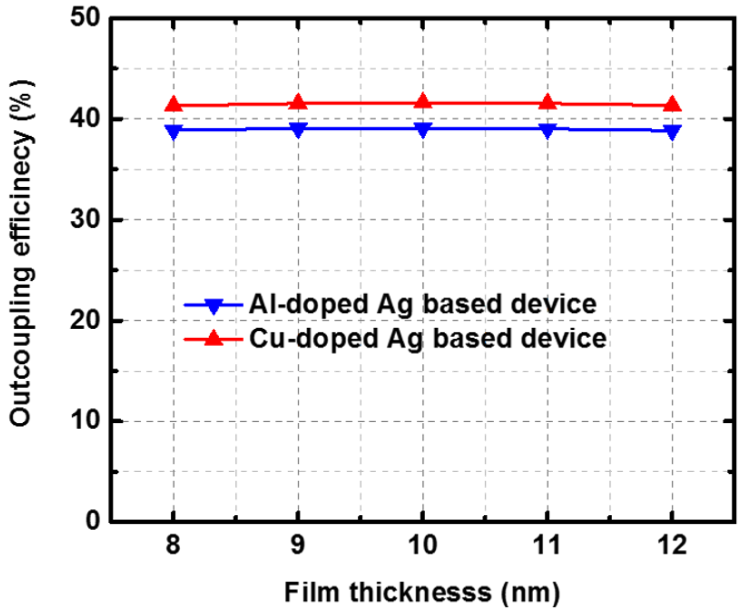

Figure 5.5: Optimized out-coupling efficiencies with different thin doped Ag film thicknesses for the Al-doped Ag- and Cu-doped Ag-based OLEDs.

5.4 Conclusions

This chapter presents the numerical studies of applying doped Ag films as transparent conductors in organic light emitting diodes (OLEDs). OLEDs based on ITO have limited out-coupling efficiencies due to the confined light emission in the ITO/organic layers, as well as poor mechanical flexibilities. Thin doped Ag film provides an effective solution to the above issues. OLEDs based on thin Al-doped Ag and Cu-doped Ag films are designed and compared. An OLED based on 10 nm thick Al-doped Ag electrode has an optimized

out-coupling efficiency of 39.09% in simulation, which is an 18.4% enhancement compared to that of the optimized ITO-based device. The out-coupling efficiency is further improved by replacing Al-doped Ag with a less lossy Cu-doped Ag film. A 10 nm Cu-doped Ag based OLED provides an out-coupling efficiency of 41.61. Corresponding OLED fabrication and characterization are currently underway.

Chapter 6

Nanophotonic Framework Enabled by Ultra-thin, Low-loss, and Stable Al-doped Ag Films

6.1 Introduction

In the past several decades, the emergence of nanophotonics and plasmonics has led to a number of exciting advances through the exploration of light-matter interactions at sub-wavelength scales [94, 95]. A negative index of refraction [96, 97], deep sub-diffraction imaging [8], ultra-thin optical devices [98, 99], structural colors [13, 100], and optical invisibility [101, 102] are just some of the important advances made by conjoining metal and dielectric optics. However, such nanophotonic/plasmonic systems have been largely limited due to their unavoidable optical loss. Consequently, there is now a significant effort to explore alternative materials and methods to improve the performance of plasmonic metals [103]. One material of significant interest is silver (Ag), as it has the highest performance ($\mathrm{Re}\{\varepsilon\}/\mathrm{Im}\{\varepsilon\}$) of any plasmonic material in the visible and near infrared. Unfortunately, Ag is well documented to have several fundamental problems, including difficulty to form continuous thin films (< 15 nm), rough surface morphology, poor chemical and thermal stability, and inferior adhesion to popular substrates like silicon and fused silica [19]. In fact, spontaneous de-wetting for a thin Ag film occurs even at room

temperatures [20] (such degradation is greatly accelerated even for modest temperatures ~100°C [21] [22]), whilst the entirety of Ag films can removed by ultrasonic vibrations or even Scotch tape [23].

To address several of the above issues, one commonly used method is to deposit a thin adhesion layer (e.g., Germanium [19], Nickel [24], or Molly Oxide [6]) before the Ag deposition, which can significantly reduce the Ag film roughness and promote thin film formation. However, these adhesion layers generally induce additional loss (as they are poor plasmonic materials), which is especially damaging for plasmonic structures since the optical field is enhanced at the metal-dielectric interface. Consequently, even a 1 or 2 nm thick wetting layer will cause a significant plasmonic mode damping [25-27].

This chapter reports on utilizing Al-doped Ag for building a high-performance nanophotonic framework. As discussed in detail in previous chapters, Al-doped Ag not only maintains Ag's superior optical properties, but at the same time, overcomes many of its limitations. Wetting-layer-free thin Ag films can be achieved for a thickness down to 6 nm with a sub-nanometer roughness on various substrates, including silicon, fused silica, and flexible substrates (e.g., PET films). Additionally, Al-doped Ag is shown to have a substantially improved substrate adhesion, and is stable at both room temperatures and elevated temperatures up to 500 °C. Building upon these unique advantages, several key nanophotonic components based on Al-doped Ag have been demonstrated, including hyperbolic metamaterials and low loss plasmonic waveguides.

6.2 Hyperbolic metamaterials based on Al-doped Ag films

The first nanophotonic application of Al-doped Ag is in high performance hyperbolic metamaterials (HMMs). HMMs are highly anisotropic structures which exhibit a metallic response (i.e., Re$\{\varepsilon\} < 0$) in one (two) directions and a dielectric response (i.e., Re$\{\varepsilon\} > 0$) in the other two (one) directions. Such a high anisotropy endows HMMs with a theoretically unbounded hyperbolic dispersion and thus, an ultra-high photonic density of states (PDOS) [1]. HMMs have been used to demonstrate broadband absorption [104, 105], enhanced spontaneous emission [12], and engineered thermal radiation [106].

One way to fabricate HMMs is by depositing alternating layers of thin metal and dielectric films (inset of figure 6.1a), leading to a dielectric response (i.e., Re$\{\varepsilon_\perp\} > 0$) in the direction normal to the layers and a metallic response (i.e., Re$\{\varepsilon_\parallel\} < 0$) in-plane. The electromagnetic response of such HMMs is described by an effective magnetic permeability equal to the value of the free-space, and an effective electric permittivitity in the tensor form: $\varepsilon_{eff} = \begin{pmatrix} \varepsilon_\parallel & 0 & 0 \\ 0 & \varepsilon_\parallel & 0 \\ 0 & 0 & \varepsilon_\perp \end{pmatrix}$, where $\varepsilon_\parallel$ and $\varepsilon_\perp$ are complex values ($\varepsilon_\parallel = \varepsilon'_\parallel + i\varepsilon''_\parallel$ and $\varepsilon_\perp = \varepsilon'_\perp + i\varepsilon''_\perp$).

The dispersion relation of HMMs is given by: $k_x^2/\varepsilon_\perp + k_z^2/\varepsilon_\parallel = k_0^2$, where k_x and k_z are the complex amplitudes of the transverse and normal components of the complex wave-vector, and k_0 the free-space wave-vector (with respect to the coordinate system in figure

6.1a). Since $\varepsilon'_{\parallel} < 0$ and $\varepsilon'_{\perp} > 0$, HMMs are governed by hyperbolic equi-frequency curves. For example, in the case of the HMM shown in figure 6.1a (four periods of 7nm Al-doped Ag and 20 nm Ta_2O_5 films), the measured $\varepsilon'_{\parallel}$ and $\varepsilon'_{\perp}$ at 700 nm are -1.41529 and 7.86797, respectively. This leads to a dispersion curve plotted in figure 7.2b. There is a cut-off band defined by $|k_x| < k_c$, where $k_c = \sqrt{\varepsilon_{\perp}} * k_0$. Electromagnetic waves with transverse wave-vector k_x located within this band decay evanescently in the z direction. In contrast, for electromagnetic waves with transverse wave-vectors $|k_x| > k_c$, they are propagation modes in the HMM (high-k modes)

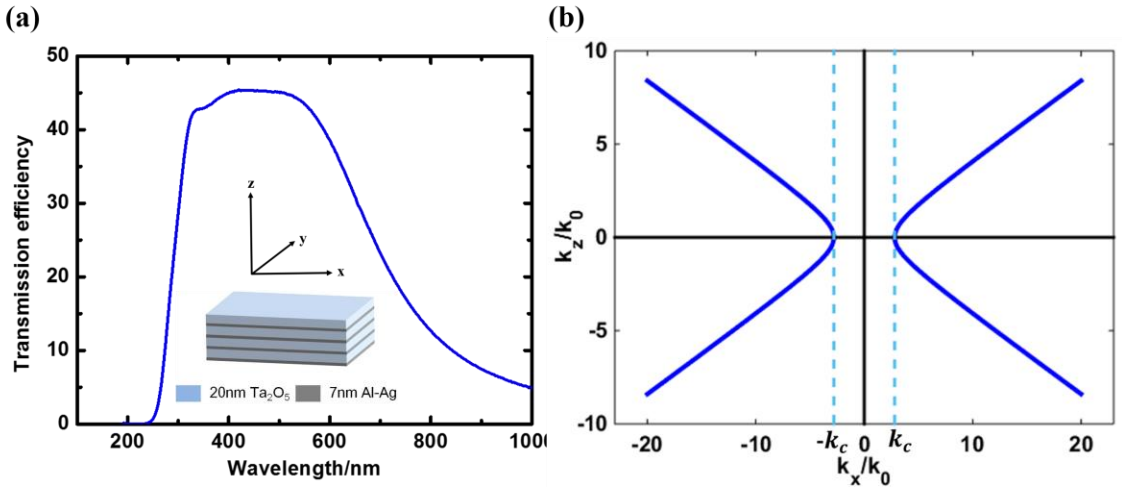

Figure 6.1: (a) Measured transmission efficiency of the fabricated HMM consisting of 4 period of 7 nm Al-doped Ag and 20 nm Ta_2O_5. The inset is its schematic drawing. (b) Dispersion curve of HMM at 700 nm. The HMM supports the propagation of modes with transverse wave-vectors larger than k_c.

However, there is a limit of the maximal allowed high-k modes, which is determined by the inverse of the HMM unit cell size, *i.e.*, $\Lambda = t_{metal} + t_{dielectric}$. This is because that at a large value of k_x, the normal component of wave-vector k_z is also large (consistent with

the hyperbolic dispersion). Consequently, the effective wavelength ($\lambda_z = \frac{2\pi}{k_z}$) along the normal direction is getting comparable with the unit size cell and therefore, the effective medium theory approximation breaks down. Instead, the photonic band structures originating from the multi-layer configurations of HMMs should be considered, which seriously compromises the ultra-high PDOS predicted by the theoretical hyperbolic dispersion of HMMs. Therefore, it is desirable to have thin constituent layers in HMMs. Also, maintaining thin constituent layers increases the transmission per period and enabling light to propagate farther into the material. However, since it is challenging to obtain thin and smooth Ag films, most reported HMMs use relatively thick (and rough) Ag films, and suffer from a lossy and non-homogeneous response (e.g., oscillating transmission spectra which deviates from effective medium theory [16]). In contrast, the ultra-thin and smooth Al-doped Ag films greatly improve upon these limitations, facilitating the fabrication of low-loss and homogeneous HMMs with a high transmission, small unit cell size, and optical properties which are well approximated by effective medium theory.

The fabricated HMM consists of four periods, alternating layers of 7 nm Al-doped Ag and 20 nm Ta_2O_5, starting with the Al-doped Ag film on the fused silica substrate (inset of figure 6.1a). The measured transmission at normal incidence is plotted in figure 6.1a. It has both a high and smooth transmittance across the visible range, which benefits from the ultrathin, smooth and low-loss metallic layer.

The structure's optical properties were characterized using spectroscopic ellipsometry (M2000, J. A. Woollam Co.), where the HMM was modelled as a uniaxial anisotropic medium with different in-plane (parallel) and out-of-plane (perpendicular) optical constants. The simulated and measured permittivities are plotted in figures 6.2a and b (real and imaginary part, respectively), which corresponds closely with each other. In the parallel direction, the epsilon near zero (ENZ) point is around 610 nm, and beyond this wavelength, the HMM's dispersion transits from an ellipsoidal to hyperbolic behavior.

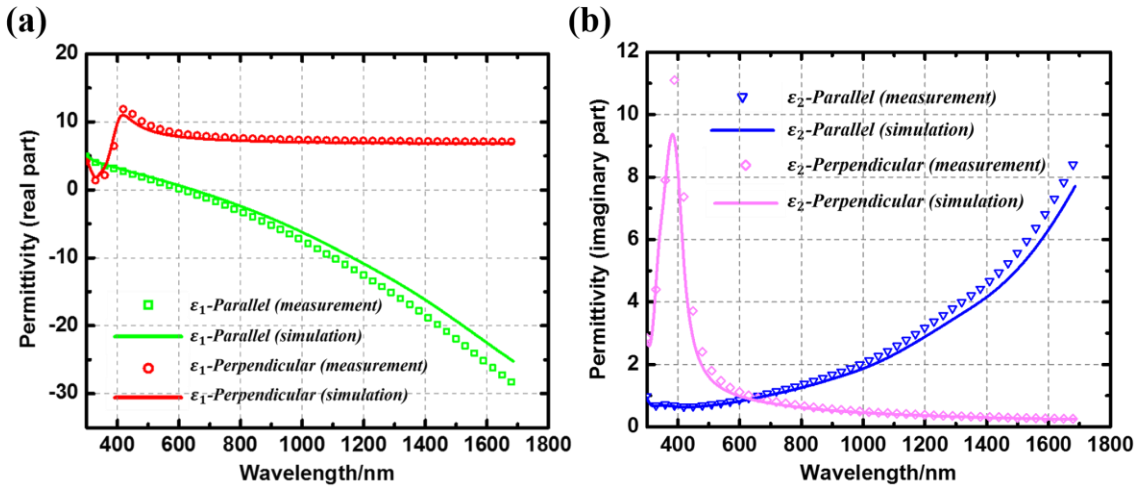

Figure 6.2: Measured permittivities of the fabricated HMM. (a) Simulated (solid curve) and measured (dotted curve) of the real part of the permittivity of the fabricated HMM. The permittivity along the parallel direction turns into negative beyond 610 nm and therefore, the HMM has a hyperbolic dispersion. (b) Simulated (solid curve) and measured (dotted curve) of the imaginary part of the permittivity of the fabricated HMM.

As noted previously, the maximal allowed high spatial wave-vectors (high-k modes) in HMMs are determined by the inverse of HMM unit cell sizes. One way to demonstrate this is by examining the transmission amplitude of an electromagnetic wave with a large-value k_x through the HMM [10]. Figures 6.3a and b show the transmission amplitudes of modes

with different k_x values through two HMMs, which have an identical thickness and ratio of metal-dielectric layers, but a different unit cell size. The HMM considered in figure 6.3a consists of 8 periods of 7 nm Al-doped Ag and 20 nm Ta_2O_5, while the HMM in figure 6.3b consists of 4 periods of 14 nm Al-doped Ag and 40 nm Ta_2O_5. Although these HMMs have an identical ratio and total thickness of metal and dielectric layers (thus an identical behavior predicted by the effective media theory), the HMM with thinner constituent layers supports a much broader transmission band for high-k modes, which contributes to a larger photonic density of states (PDOS) [107]. A high PDOS is essential to many extraordinary phenomena enabled by HMMs (broadband absorption, enhanced spontaneous/stimulated emission, engineered thermal radiation, etc). As an example, for a dipole emitter located 10 nm above the HMM, the Purcell enhancement factor of the emitter on top of HMM with thinner layers is much larger than that of the emitter on top of HMM with thicker layers (figure 6.4).

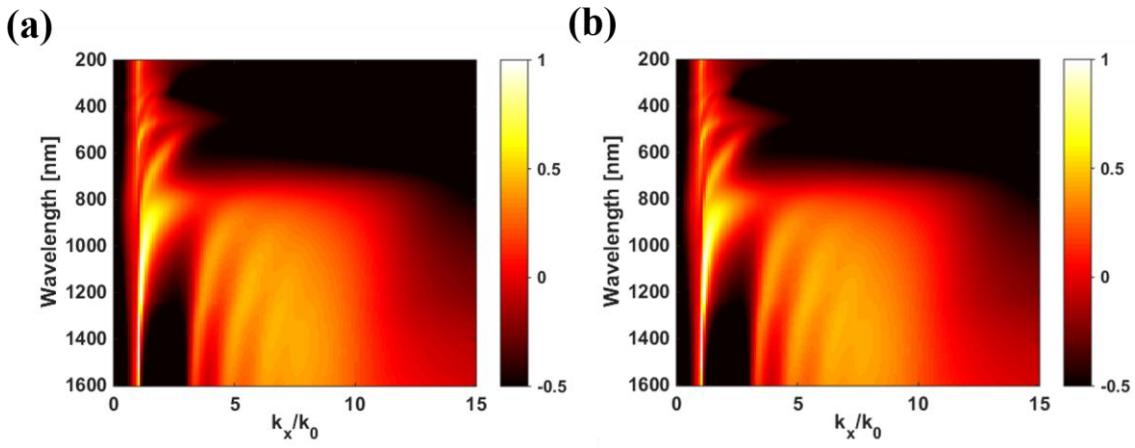

Figure 6.3: (a) Calculated transmission amplitude of an electromagnetic wave with different transverse wave-vectors (k_x) through a HMM made of 8 periods of 7 nm Al-doped Ag and 20 nm Ta_2O_5. (b) Calculated transmission amplitude of an electromagnetic wave with different transverse wave-vectors (k_x) through a HMM made of 4 periods of 14 nm Al-doped Ag and 40 nm Ta_2O_5. HMM consisting of thinner constituent layers supports a broader bandwidth of high-k modes.

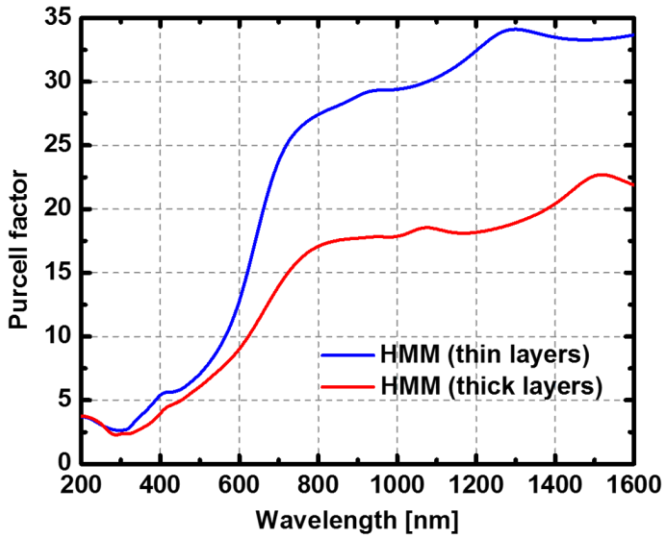

Figure 6.4: Calculated Purcell factor of a dipole emitter located 10 nm above two HMMs studied in figure 6.3a and 6.3b. The Purcell factor is averaged over different dipole orientations (2/3 contribution from parallel dipoles and 1/3 contribution from vertical dipoles). HMM with thinner constituent layers provides a larger Purcell factor.

In a planar system, when a dipole is placed at a distance d above a single or multilayer films with a perpendicular (⊥) or parallel (∥) orientation to the interfaces, the corresponding Purcell factors F can be written as the following: [108, 109]

$$F_{\perp} = 1 - \eta_0 + \frac{3}{2}\eta_0 \mathrm{Re}\left[\int_0^{\infty} dk_x \frac{1}{k_z}\left(\frac{k_x}{\sqrt{\varepsilon_1}k_0}\right)^3 \left(1 + r_p e^{2ik_z d}\right)\right]$$

$$F_{\parallel} = 1 - \eta_0 + \frac{3}{4}\eta_0 \mathrm{Re}\left[\int_0^{\infty} dk_x \frac{1}{k_z}\frac{k_x}{\sqrt{\varepsilon_1}k_0}\left(1 + r_s e^{2ik_z d} + \frac{k_z^2}{\varepsilon_1 k_0^2}\left(1 - r_p e^{2ik_z d}\right)\right)\right]$$

Here, η_0 is the internal quantum efficiency of the emitter in free space and is assumed to be unity in this calculation. k_x and k_z are the components of the wave-vector along the x and z axis, respectively. k_0 is the free-space wave-vector. r_s and r_p are the reflection coefficients of the structure at the interface for an s and p polarized light, and are calculated using the transfer matrix method. ε_1 is the relative permittivity of the host media of the emitter and is unity in this calculation. The integrants in the above two equations refer to the normalized dissipated power spectra, which represents the energy emitted into different dissipation channels.

In the case of isotropic orientated emitters (2/3 contribution from parallel dipoles and 1/3 contribution from vertical dipoles), the average Purcell factor can be calculated as:

$$F = \frac{1}{3}F_{\perp} + \frac{2}{3}F_{\parallel}$$

6.3 Plasmonic interconnects based on Al-doped Ag films

Another application which can greatly benefit from high quality thin metallic films is low loss plasmonic waveguides. For a thin metallic film embedded in a dielectric surrounding, the surface plasmon polaritons (SPPs) on both the upper and lower interface between the film and dielectric will couple with each other and form a symmetric long-range SPP (LR-SPP) mode that is quasi-photonic [110]. Such modes have many advantages (e.g., wide operational bandwidth, the ability to couple with other plasmonic structures, the ability to support both electrical and optical signals, etc), and have been utilized in various plasmonic devices [111-115]. Although Ag is a low-loss plasmonic material in the visible and near-IR range, it is rarely employed in LR-SPP waveguides due to its difficulty in forming thin films, surface roughness, poor adhesion with substrates, and rapid degradation in ambient environments. It is worthwhile to note that the methods of adding adhesion layers to produce thin Ag films are not suitable for fabricating LR-SPP waveguides, and this is because wetting layers, such as Ge, Ni, Cr, are highly lossy plasmonic materials and therefore lead to a significant damping of the SPP modes [25-27].

Using Al-doped Ag films, LR-SPP waveguides were fabricated on fused silica substrates and their performances were characterized. The device layout is shown in figure 6.5a, where the index matching condition at 1.55 μm was achieved using an index-matching oil. To fabricate the LR-SPP waveguide, a 10 nm thick, Al-doped Ag film was first deposited on a fused silica substrate by Al and Ag co-deposition. Subsequently, the film underwent an annealing treatment (500 °C for 10 s in a N_2 environment) to further reduce its loss.

Photolithography was used to define the waveguide shape in the photoresist first (GCA AS200 AutoStep) and the pattern was then transferred into the Al-doped Ag films by Argon (Ar) ion-bombardment etching (STS Pegasus ICP). Finally, the photoresist was removed by Acetone with the aid of ultrasound sonication. As mentioned earlier, Al-doped Ag films have good adhesion with substrates and are robust against commonly used chemicals during the nano-fabrication. These properties contribute to the successful fabrication of Al-doped Ag based LR-SPP waveguides. The fabricated Al-doped Ag LRSP waveguide has a width of 9 μm and thickness of 10 nm (figure 6.5b).

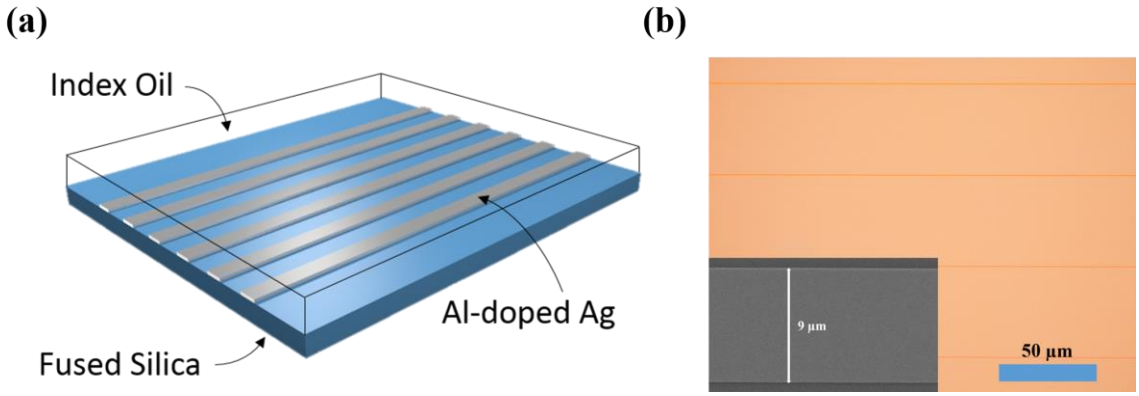

Figure 6.5: LR-SPP waveguide based on Al-doped Ag. (a) Schematic drawing of the Al-doped Ag LR-SPP waveguide. Index matching oil is used to match the refractive index of fused silica substrate at 1.55 μm. (b) Optical microscope of fabricated Al-doped Ag LR-SPP waveguide. The insert is the SEM picture of one waveguide.

The device performance is characterized by the fiber end-coupling method, as shown in figure 6.6. The out-coupled waveguide mode and its intensity profile along the vertical direction are shown in figure 6.7a and b, respectively, where the vertical mode size ($1/e^2$ width) is found to be ~9 μm with a propagation loss (1/e decay length) of 0.66 dB/cm.

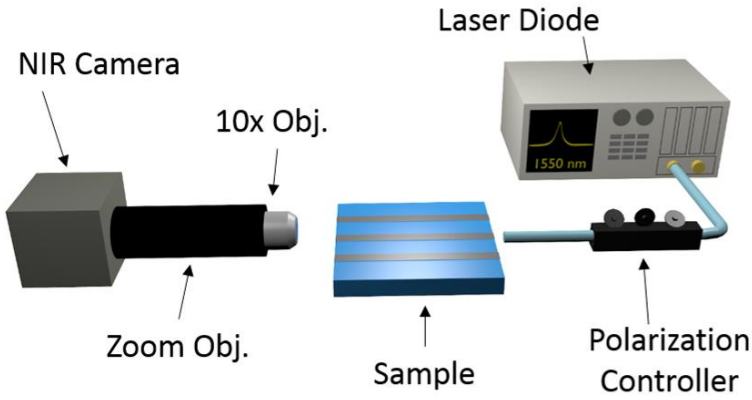

Figure 6.6: Measurement set-up to characterize the mode profile and propagation loss of the waveguide.

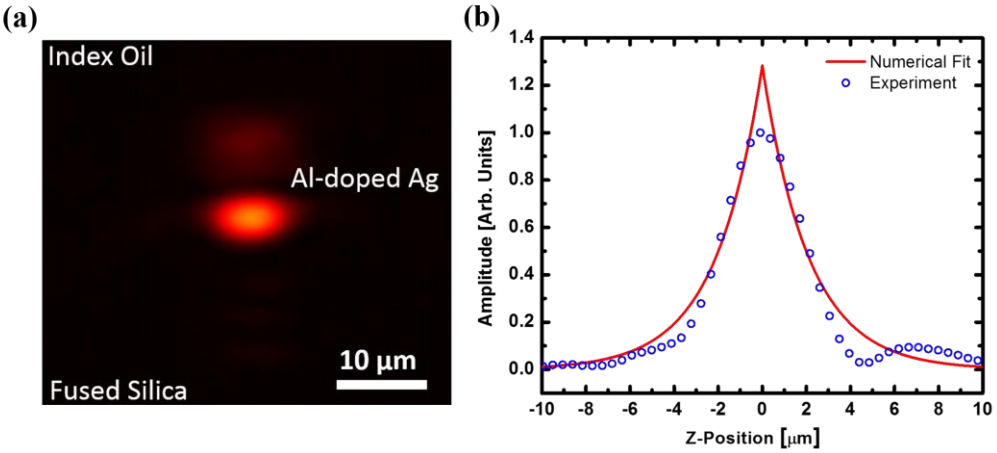

Figure 6.7: (a) Experimentally measured modal profile from the output facet of the Al-doped Ag LRSP waveguide. (b) Fitting of the vertical intensity with an exponential decay of the plasmonic mode.

The measurement is compared to simulation, shown in figure 6.8, where the simulated mode size and propagation loss for the 10 nm thick and 9 µm wide waveguide are 13 µm and 0.46 dB/cm, respectively. The discrepancy between simulation and measurement can be attributed to factors such as film thickness variation during deposition and lensing effects due to the index matching oil [116]. The experimentally demonstrated propagation

length of over 3 centimeters is an order of improvement compared with those from similar 10 nm thick, LR-SPP waveguides made of Au and TiN (figure 6.8) [116-118], and such an improvement is due to the low-loss nature of the Al-doped Ag films. Moreover, the propagation length can be further improved by reducing Al-doped Ag strip width and thickness, improving the cladding material properties [119], or using multi-strip configurations [120].

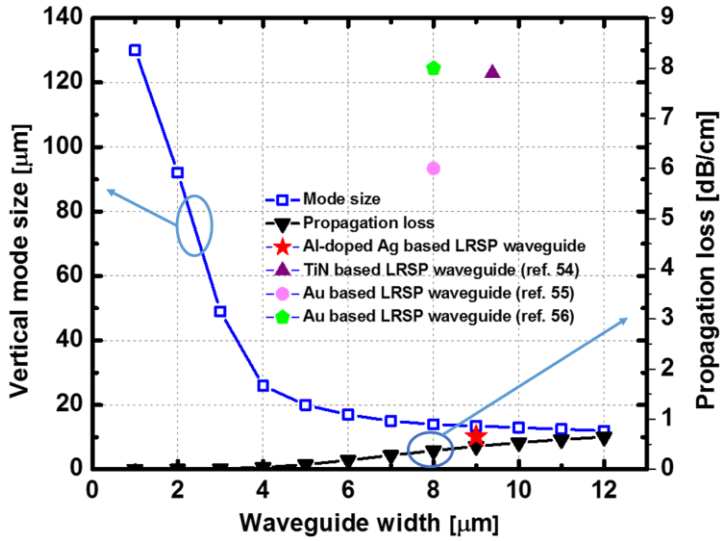

Figure 6.8: Simulated mode size and propagation loss of 10 nm thick, Al-doped Ag strip waveguide with different strip widths (solid lines). The red star denotes the measured propagation loss of a 10 nm thick, 9 μm thick Al-doped Ag LR-SPP waveguide in this work. The purple triangle denotes the measured propagation loss of a 10 nm thick, 9.38 μm thick TiN LR-SPP waveguide [116]. The green pentagon and magenta circle denote the measured propagation loss from two 10 nm thick, 8 μm wide Au LR-SPP waveguides [117, 118].

6.4 Conclusions

This chapter presents a nanophotonic framework enabled by Al-doped Ag films. Two representative nanophotonic devices are investigated: hyperbolic metamaterials (HMMs) and long range surface plasmon polariton (LR-SPP) waveguides. HMMs consisting of thin constituent layers of Al-doped Ag films have both a low-loss and homogenous response. Also, they support a broader bandwidth of high-k modes compared to HMMs made of thicker layers. LR-SPP waveguides based on thin Al-doped Ag films demonstrate a propagation length of a few centimeters, which is an order of improvement compared to similar structures made of other plasmonic materials.

Chapter 7

Highly Efficient, Broadband, and Angular Robust Asymmetric Light Transmitting Metasurface

7.1 Introduction

In the previous chapters, a new kind of optical materials: Al-doped Ag film and its various applications in optoelectronic and nanophotonic devices have been studied. Here, I will switch the gears and discuss a few photonic devices which don't necessarily reply on doped Ag films. These devices include metasurfaces which provide asymmetric transmission of light, metasurfaces which convert a linearly polarized input light into an axially polarized output light, as well as optical resonant structures which work as high-performance ultrasound detectors.

The first example is a highly efficient, broadband, and angular robust asymmetric light transmitting metasurface. Devices providing asymmetric transmission of light are useful components for optical communication systems, information processing, and laser applications [121-124]. Recently, asymmetric light transmission with metamaterials has received considerable interest [125-128]. Although these devices are usually reciprocal and not suitable for applications such as optical isolation [129, 130], they have unique advantages of passive operation and compact size. They can be realized using photonic

crystals [131, 132], helical wires [133], hyperbolic metamaterials [10], and non-symmetric gratings [134, 135]. However, they typically suffer from complex fabrication processes, low efficiency, and limited operational bandwidth. For example, helical wires provide efficient and broadband asymmetric transmission for circularly polarized light in the infrared region [133], but they are fabricated by direct laser writing and gold plating, which is complex and time-consuming. Hyperbolic metamaterials sandwiched between two Chromium (Cr) gratings have shown broadband asymmetric light transmission as well, but exhibited a low transmission efficiency [10]. A device consisting of a metallic grating cascaded with a dielectric grating provides close to 100% transmission efficiency in simulation, but has a limited bandwidth [136]. Besides, the performance of these metamaterials is usually sensitive to fabrication errors and the angle of incident light, which limits their practical applications. Further, it is also difficult to employ the same design strategy for asymmetric light transmission at different wavelength ranges.

In this chapter, a few-layer metasurface offering efficient and broadband asymmetric transmission of light is reported. Metasurfaces are sub-wavelength textured surfaces that can be thought of as the two-dimensional equivalent of metamaterials [137-141]. They exhibit versatile, tailored electromagnetic functions such as frequency selectivity [13, 142], polarization control [98, 143-146], wavefront engineering [147-151], and even nonlinear responses [152-154]. The asymmetric light transmitting metasurface in this work consists of three closely-spaced layers of one-dimensional (1D) gold nano-gratings. Contrary to predictions of the conventional theory (e.g., Malus' law), the proper cascade of three layers

of nano-gratings instead offers an efficient and broadband asymmetric light transmission for a linearly polarized light. Furthermore, the device is only 290 nm (λ/5) thick, and its performance is robust to angle of incidence and fabrication variations. As an experimental demonstration, a device providing asymmetric transmission at a central wavelength of 1.5 μm is fabricated and characterized, which shows a transmission efficiency of 80%, extinction ratio of 24:1, and a full width half maximum (FWHM) operating bandwidth of 1.7 μm. Furthermore, the design concept is suitable for large-area device manufacturing and can be easily transitioned to achieve asymmetric light transmission at other wavelengths.

7.2 Design

The designed asymmetric light transmission metasurface consists of three layers of 40 nm thick gold (Au) nano-gratings, each of which are separated by a 125 nm thick SU-8 dielectric spacer (Figure 7.1). The nano-gratings on the left and right layers have a period of 140 nm and linewidth of 70 nm. The nano-grating on the middle layer has a period of 200 nm and linewidth of 100 nm. The gratings are oriented 0°, 45°, and 90°, for the first, second, and third layers, respectively. When x-polarized light is incident from the left side, it is efficiently transmitted through the metasurface and converted to y-polarized output. In contrast, there is very little transmission of x-polarized light when incident from the right (opposite) side of the metasurface. Therefore, this metasurface provides asymmetric transmission for linearly polarized light.

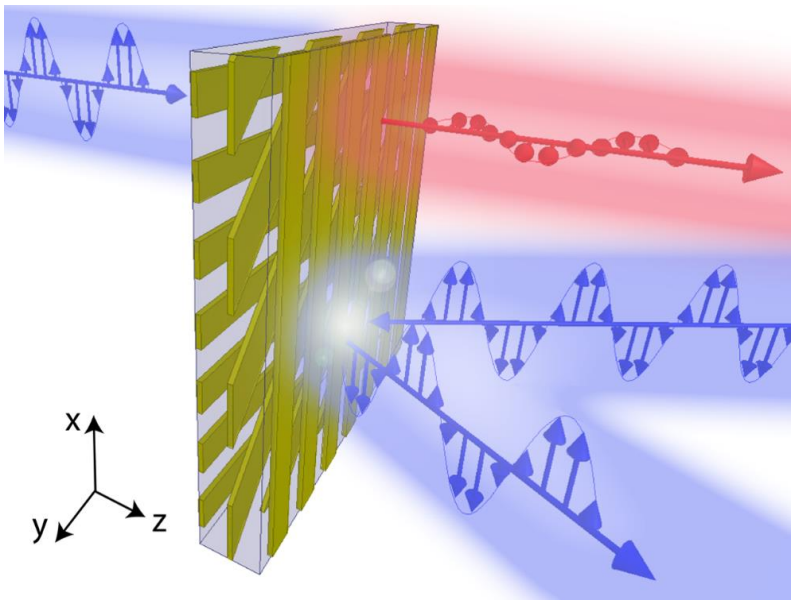

Figure 7.1: Artistic rendering of the metasurface, consisting of three layers of cascaded Au nano-gratings. The metasurface provides high transmission of x-polarized light incident from the left side, but blocks x-polarized light that is incident from the right side.

Each layer of the Au nano-gratings individually functions as a linear polarizer, which transmits light polarized orthogonal to the grating, while absorbing/reflecting light polarized along the grating. According to Malus' law, the transmission intensity of a linearly polarized light through a linear polarizer is: $I = I_0 \cos^2 \theta$, where I_0 and I are the light intensity before and after the polarizer, and θ is the angle between the incident light polarization direction and the polarizer transmission axis. In an ideal case where the metallic nano-gratings provide unity light transmission, there will only be 25% transmission intensity for x-polarized light incident from the left side through the cascaded system of three linear polarizers whose transmission axes are rotated 45° with respect to each other. When the finite cell size and material absorption are taken into account, the efficiency is even lower. The response of an individual layer of the Au nano-gratings within

the dielectric environment is simulated using Ansys HFSS. The electric field transmission coefficients of each layer are expressed as:

$$T_b = \begin{pmatrix} b_{xx} & b_{xy} \\ b_{yx} & b_{yy} \end{pmatrix} \qquad T_m = \begin{pmatrix} m_{xx} & m_{xy} \\ m_{yx} & m_{yy} \end{pmatrix} \qquad T_t = \begin{pmatrix} t_{xx} & t_{xy} \\ t_{yx} & t_{yy} \end{pmatrix}$$

Where b_{xx} denotes the electric field transmission coefficient of the bottom layer for an x-polarized input to an x-polarized output, and m_{xy} denotes the electric field transmission coefficient of the middle layer for a y-polarized input to an x-polarized output. Malus' law neglects reflections between the layers, so all coefficients are treated as real numbers (transmission amplitude only), and no phase information is included.

The total electric field transmission through the three layers can be calculated as:

$$T = \begin{pmatrix} E_{xx} & E_{xy} \\ E_{yx} & E_{yy} \end{pmatrix} = T_t T_m T_b = \begin{pmatrix} t_{xx} & t_{xy} \\ t_{yx} & t_{yy} \end{pmatrix} \begin{pmatrix} m_{xx} & m_{xy} \\ m_{yx} & m_{yy} \end{pmatrix} \begin{pmatrix} b_{xx} & b_{xy} \\ b_{yx} & b_{yy} \end{pmatrix}$$

Finally, the intensity transmission coefficients are calculated as the squares of the electric field transmission coefficients. They are plotted in figure 7.2. The notation T_{nm} means transmission intensity of m-polarized input light into n-polarized output light.

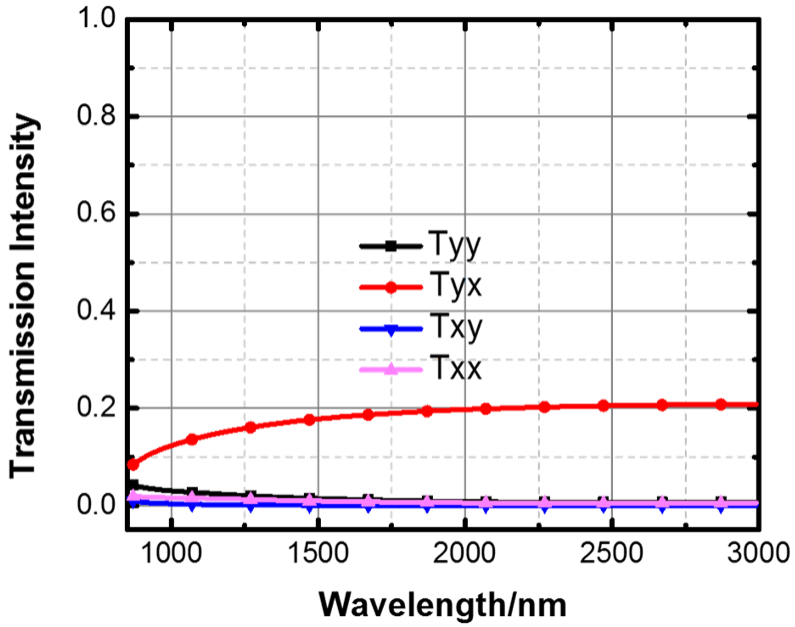

Figure 7.2: Simulated transmission intensity through three layers of Au nano-gratings based on the Malus' law.

However, Malus' law breaks down for the proposed structure consisting of closely spaced Au gratings. Next, the three layers of cascaded Au nano-gratings are treated as an integrated structure and its electromagnetic response is calculated (linear scale in Figure 7.3a and logarithmic scale in Figure 7.3b). In contrast to the predictions of Malus' law, this metasurface provides a high transmission of x-polarized light when it is incident from the left side, while blocking the same polarization incident from the right side. The simulated transmission efficiency around 1.5 μm is 85% with an extinction ratio of 53 (17.2 dB). The extinction ratio is defined as the ratio of the transmittance of x-polarized light from the left side ($T_{yx} + T_{xx}$) to the transmittance of x-polarized light from the right side ($T_{xy} + T_{xx}$). The device has a FWHM operating bandwidth of 1.67 μm. Malus' law only applies to cases where the multiple reflections between layers are negligible. However, for the metasurface

here, there are strong multiple reflections between the Au nano-grating layers. Such interaction leads to an asymmetric light transmission as well as polarization conversion in the structure.

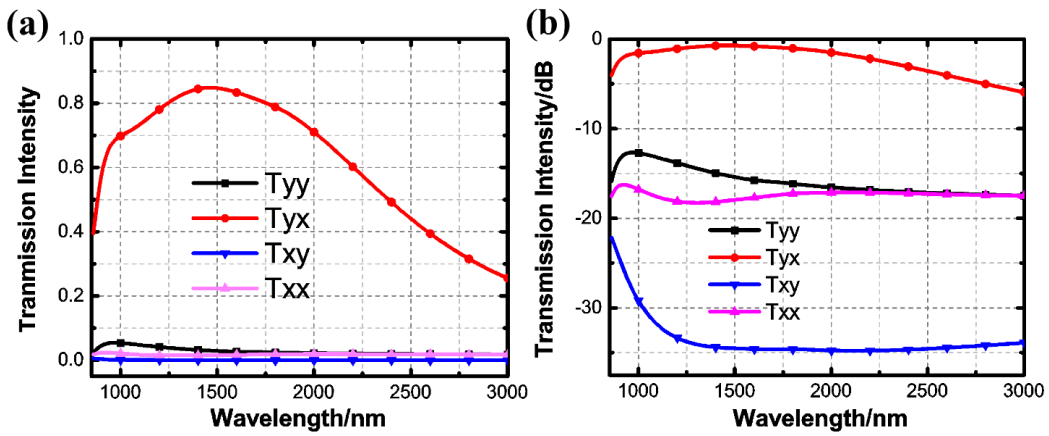

Figure 7.3: Simulated transmission intensity through the metasurface in the linear (a) and logarithmic (b) scale.

The asymmetric response is due to the "cavity effect" rather than the near field coupling between layers. The multiple reflections between layers in this properly designed three-layer structure leads to an enhanced cross-polarization transmittance (T_{yx}) over a broad bandwidth, as well as suppressed transmittances of other co- and cross-polarization conversions (T_{yy}, T_{xy}, and T_{xx}). This contributes to the asymmetric light transmission behavior of the metasurface. To better illustrate this point, the effective anisotropic impedance of each grating layer is simulated first, and then the grating layers are replaced with three infinitesimally thin sheets which have the effective impedances of the gratings. In this study, only the "cavity effect" is taken into account. As shown in Figure 7.4, the simulated transmittance of the three "equivalent sheets" corresponds well with the full-wave simulated transmittance of the metasurface.

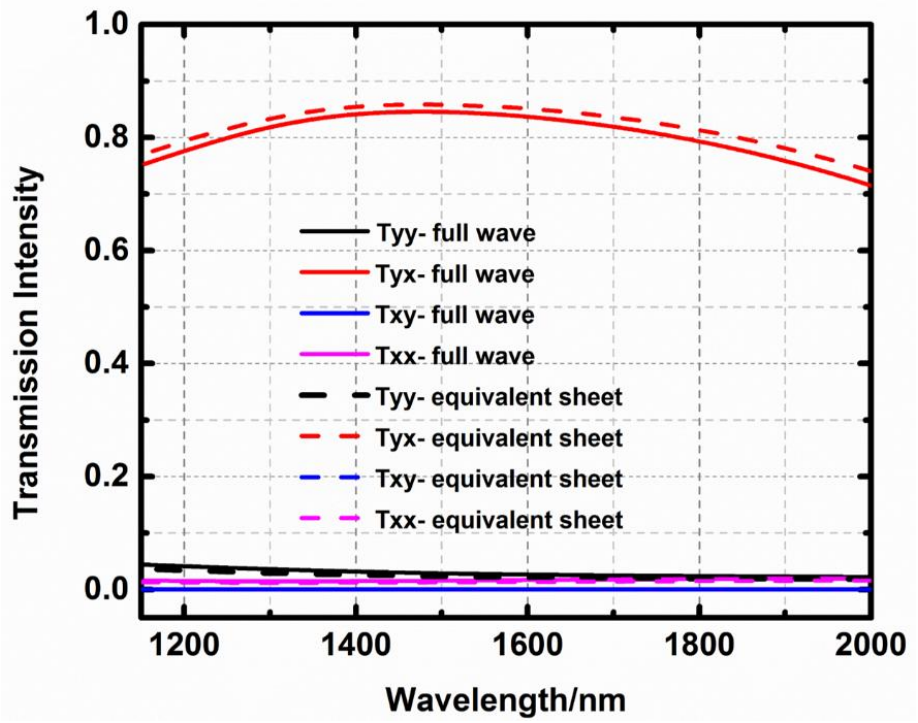

Figure 7.4: Calculated transmittance of the metasurface based on full-wave simulation of the structure (solid curves) and simulation of cascaded equivalent sheets.

Cascading two orthogonal 1D metallic gratings (e.g., left and right grating layers in Figure 7.1) will lead to weak co-polarization conversions, and negligible cross-polarization conversions. There will also be some weak "cavity effect" in this two-layer structure depending on the separation between layers, as shown in Figure 7.5. However, the 45˚ orientated middle grating works as an efficient polarization conversion layer to generate cross-polarization transmission. Furthermore, such a conversion mechanism is enhanced by the cavity effect within the metasurface, which leads to its broadband asymmetric light transmission behavior.

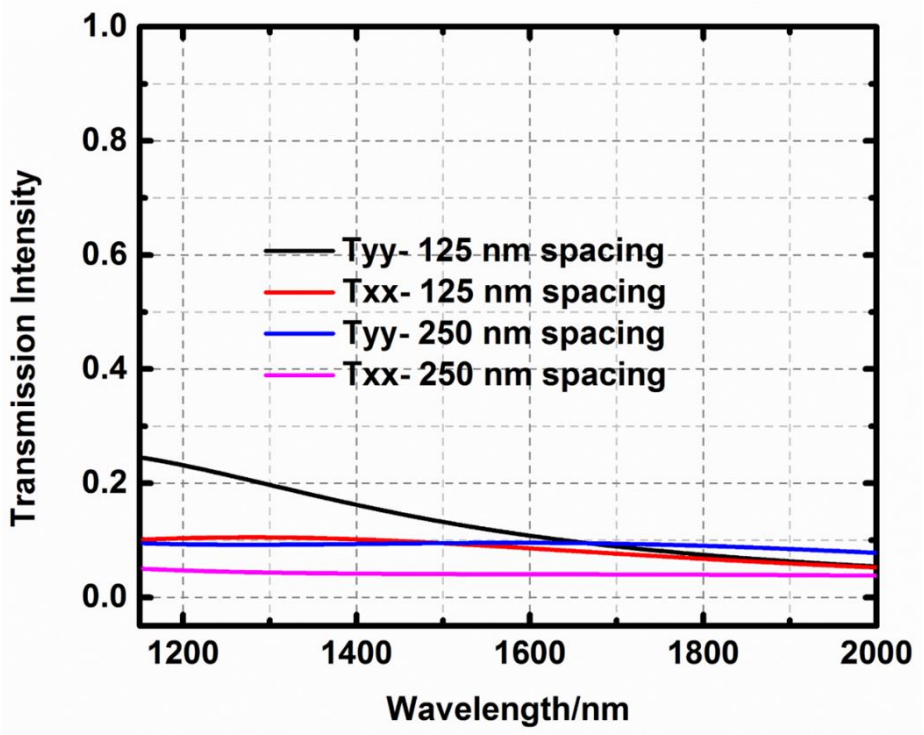

Figure 7.5: Calculated transmittance of two orthogonal grating layers separated a SU8 spacer. The grating geometry is identical to the top and bottom layer gratings studied in the manuscript. There are weak co-polarization transmittance, and the transmittance depends on the spacer layer thickness (cavity effect). However, there are negligible cross-polarization conversions.

Indeed, generating asymmetric transmission for linear polarization requires anisotropic electric and bianisotropic responses (i.e. magneto-electric coupling). An arbitrary electric response can be generated using a single-layer patterned sheet. However, a single sheet cannot generate magnetic and magneto-electric responses, which are necessary for a high-efficiency polarization conversion. In fact, the fundamental limit for cross-polarization conversion is 25% if only an electric response is utilized [155]. Therefore, in this work, the attention is turned to designs consisting of multiple layers. A systematic design method for realizing arbitrary polarization conversion is outlined in Ref. [145]. It is shown that each

sheet can be homogenized as an equivalent sheet impedance with well-defined transmission and reflection coefficients. This allows the overall response of multiple cascaded sheets to be calculated, which simplifies the design procedure. It can be shown that at least 3 sheets are required to independently control electric and magnetic responses [156].

This work demonstrates that rather than designing complicated patterns that closely approach the ideal sheets, a simplified design with 1D metallic gratings can also achieve a relatively high performance. Consider two half-spaces separated by the metasurface, where the electric fields on either side of the metasurface are related by the following relation:

$$\begin{pmatrix} E_t^x \\ E_t^y \end{pmatrix} = \begin{pmatrix} t_{xx} & t_{xy} \\ t_{yx} & t_{yy} \end{pmatrix} \begin{pmatrix} E_i^x \\ E_i^y \end{pmatrix} = T \begin{pmatrix} E_i^x \\ E_i^y \end{pmatrix}$$

Here, T is the Jones matrix of the metasurface, and $E_i^{x/y}$ and $E_t^{x/y}$ are the incident and transmitted electric field polarized along the x and y directions, respectively. The element t_{nm} in the Jones matrix denotes transmission coefficient of the m-polarized electric field to the n-polarized electric field, and is usually a complex number (containing both field transmission amplitude and phase information). The transmission intensity coefficient T_{nm} equals the square of $|t_{nm}|$. For an ideal asymmetric transmitting device that allows unity conversion of x-polarized light to y-polarized light in one direction only, its Jones matrix is written as: $\mathrm{T} = e^{-i\emptyset}\begin{pmatrix} 0 & 0 \\ 1 & 0 \end{pmatrix}$ [157]. For the structure in this study, its Jones matrix at 1.5 μm is calculated as $\begin{pmatrix} 0.126e^{i75.1^\circ} & 0.018e^{-i131^\circ} \\ 0.920e^{-i44.6^\circ} & 0.169e^{i51.9^\circ} \end{pmatrix}$, which approaches the ideal case. It has been recently demonstrated that by designing each layer with complex geometries, the

metasurface performance can be further optimized [98, 145]. However, the design here, with only three layers of nano-gratings, is advantageous due to its simplicity and suitability for large-area device fabrication, with a very minimal compromise of its performance.

7.3 Fabrication and characterization

The metasurface is fabricated on a 500 μm thick fused silica substrate using the process shown in Figure 7.6a. The bottom layer is fabricated by electron beam (E-beam) lithography (JEOL 6300FS, JEOL) using Poly(methyl methacrylate) resist (PMMA 950k, A2, Microchem) followed by the deposition of a 3 nm Titanium (Ti) adhesion layer and a 37 nm Gold (Au) layer, and then metal lift-off in an acetone solution. The PMMA layer was spin-coated on the substrate at a rate of 1600 rpm for 40 seconds, and the sample was subsequently baked on the hotplate at 180 ˚C for 3 minutes. The PMMA thickness was about 100 nm. To solve the charging issues during the E-beam writing, a conductive polymer layer (E-spacer, SHOWA DENKO K.K. 13-9, Shiba Daimon 1-Chome Minato-Ku, Japan) was spin-coated onto the PMMA layer at a rate of 1500 rpm for 45 seconds, and the sample was subsequently baked on the hotplate at 110 ˚C for 2 minutes. The E-spacer layer thickness is about 20 nm. After the E-beam writing, the E-spacer layer was removed after the sample was rinsed in the DI water for 15 seconds. Subsequently, the PMMA layer was developed in the developer solution (1:3 MIBK to IPA) for 45 seconds, and rinsed in IPA for another 30 seconds. To achieve uniform pattern features, proximity effect correction (PEC) was implemented during the E-beam writing. After the metal lift-off, a 125 nm thick SU-8 layer is spun on the metal layer and cured with ultraviolet (UV)

radiation (MJB2, Karl Suss). The patterning and metal deposition/lift-off process is repeated three times in order to fabricate all three layers. The scanning electron micrographs (SEMs) of the layers are shown in Figures b to d.

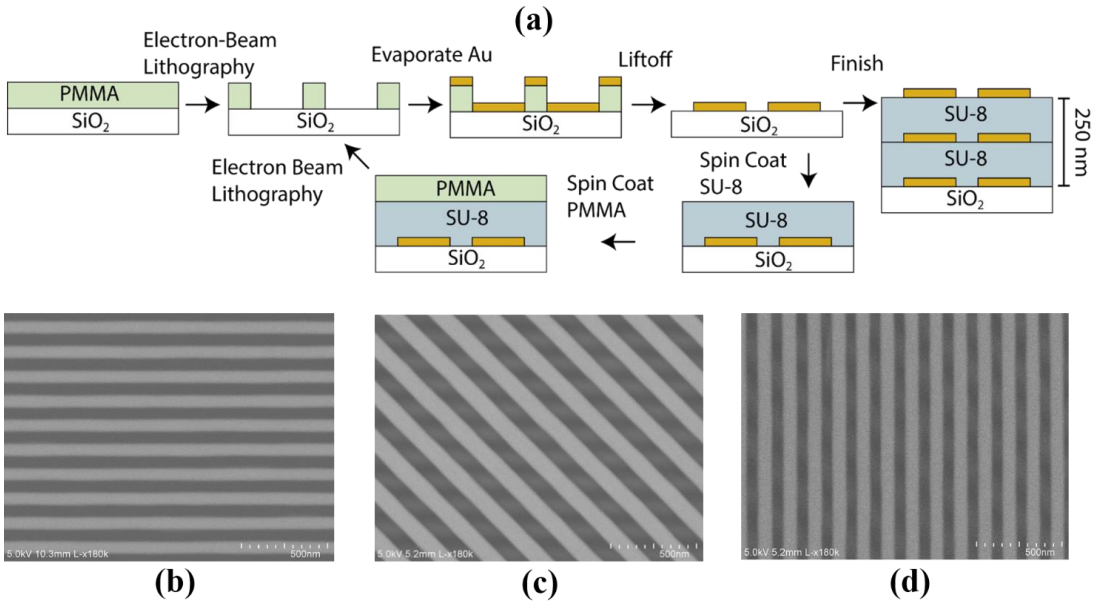

Figure 7.6: (a) Metasurface fabrication flow chart; (b-d) SEM pictures of the bottom (b), middle (c) and top (d) layer.

The metasurface is experimentally characterized after fabrication. Output from a tunable laser (TLB 6326, Newport, central wavelength at 1.5 μm) is sent through a polarization controller (FPC032, Thorlabs), a single mode optical fiber (P3-1550A-FC-1, Thorlabs), and then onto the metasurface. The polarization state from the input fiber is adjusted by the polarization controller and confirmed by a separate linear polarizer (LPNIRA050-MP2, Thorlabs) before illuminating the metasurface. The light transmitted by the metasurface passes through another linear polarizer (LPNIRA050-MP2, Thorlabs) and is collected by an objective lens into an optical power meter (2835-C, Newport). The laser wavelength is

scanned between 1470 nm and 1530 nm. The measured and simulated transmittance is plotted in figures 7.7a (linear scale) and b (logarithmic scale), showing a close correspondence. The metasurface has an averaged transmission efficiency of 80% around 1.5 μm, and an extinction ratio of 24 (13.8 dB).

Due to the limited output wavelength range from the laser, the device is only characterized over a narrow band. However, numerical simulation predicts its broad operational bandwidth (1.7 μm). To demonstrate this, the metasurface is also characterized using a different experimental setup consisting of a rotating analyzer spectroscopic ellipsometer (Model V-VASE, J.A. Woollam Co., Inc.) between 1200 nm and 1850 nm. The illumination beam size from the ellipsometer (about 700 μm in diameter) is much larger than the metasurface area (250 μm by 250 μm square), and the measured Jones Matrix represents a superposition of the fraction of the light beam sampling the device and the surrounding area. However, since the cross-polarization conversion only takes place within the metasurface, the T_{xy} and T_{yx} components can be obtained. Figure 7.8 plots the simulated and measured T_{xy} and T_{yx} components. As the contributions from the device and surrounding area are not separated, the experimental values in Figure 7.8 are normalized to the simulation result at 1610 nm and are in arbitrary units. The measurement demonstrates that the device behavior agrees well with simulation over a large bandwidth. It should be noted that, due to the absorption in a fiber optic cable on the source side of the ellipsometer, there is insufficient light intensity near 1400 nm, causing the gap in the data seen there. More accurate measurements could be ascertained by using a smaller beam spot

or a series of measurements of different size beam spots to appropriately quantify the Jones matrix elements for only the device area.

A visual demonstration that highlights the performance of the metasurface is shown in Figures 7.7c and d. Figure 7.7c is a picture of the metasurface taken with an infrared camera when a 1.5 μm laser beam illuminates the back of the metasurface. Figure 7.7d corresponds to the same setup but with the metasurface flipped around so that the laser beam illuminates from the opposite side. The same laser beam intensity and polarization are maintained in the two cases. The metasurface provides high and low transmission in Figures c and d, respectively.

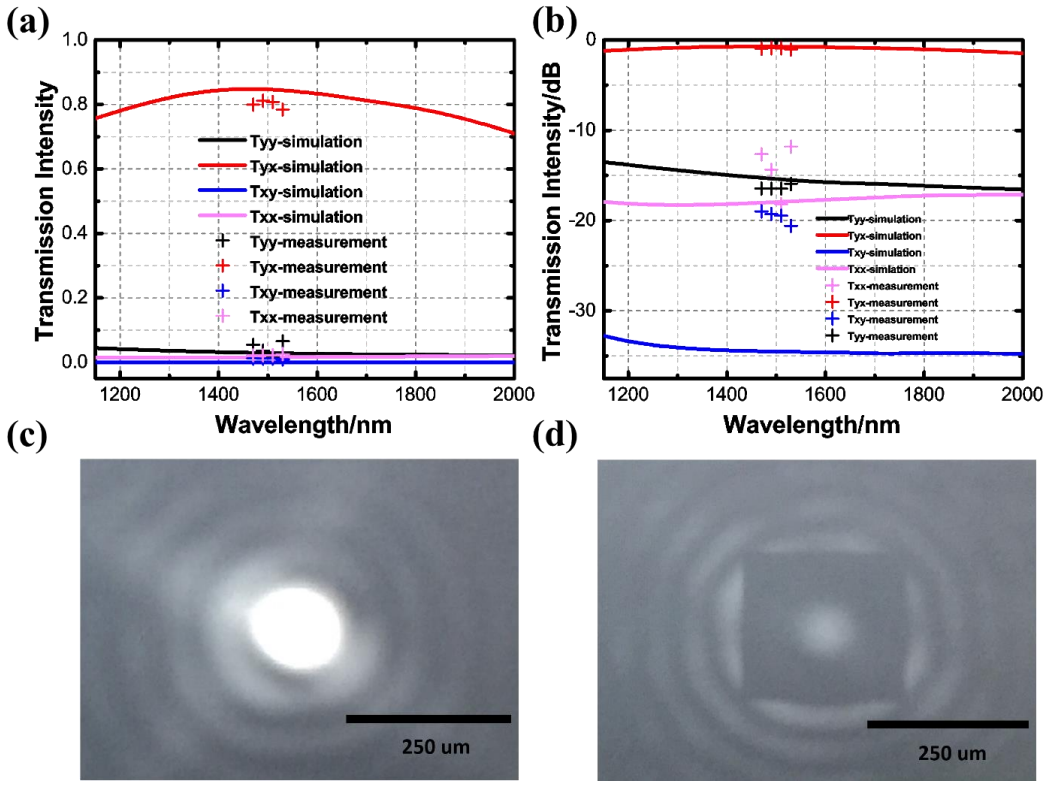

Figure 7.7: (a-b) Measured transmission intensity from the metasurface in the linear (a) and logarithmic (b) scale; (c) Bright transmitted light pattern from one direction; (d) Blocked transmitted light pattern from the reverse direction. The incident laser beam intensity is kept the same in two cases.

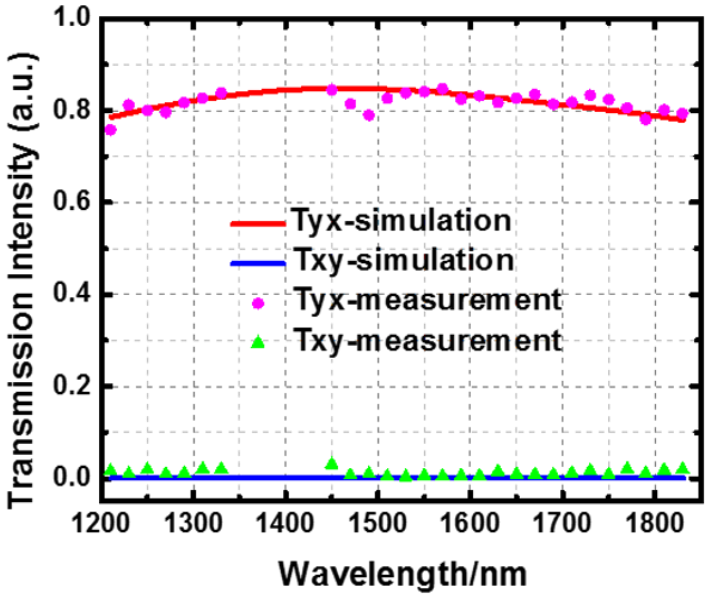

Figure 7.8: Measured T_{xy} and T_{yx} components with a broadband ellipsometer and large beam size. The measurement demonstrates the device broadband behavior and agrees well with simulation.

7.4 Angular robustness and design tolerance

For many practical applications, the device performance should be robust to the variations in the angle of incidence [13]. This also helps reduce the requirements of other optical components in the system. Figures 7.9a and b plot the simulated transmittance of the metasurface at 1.5 μm versus different angles of incidence in the XZ and YZ plane. There is a minimal performance degradation of the metasurface until the incident angle reaches 50°. As an experimental verification, the transmittance was measured at a 30° input angle (XZ and YZ plane respectively) and is plotted in figure 7.9c and d. It can be seen that at such an incident angle, the metasurface still maintains its properties of high transmission, broad bandwidth, and a good extinction ratio. The device's robust angular tolerance can be

understood by examining the angular response of the individual layers. The transmission intensity through a single Au nano-grating layer is simulated at both normal incidence and 30˚ oblique incidence (in the YZ and XZ plane respectively. Figure 7.10). The grating has a period of 140 nm and linewidth of 70 nm, and the Au thickness is 40 nm. It can be seen that the individual layer has a good incident light angular tolerance and this leads to the angular robust performance of the metasurface.

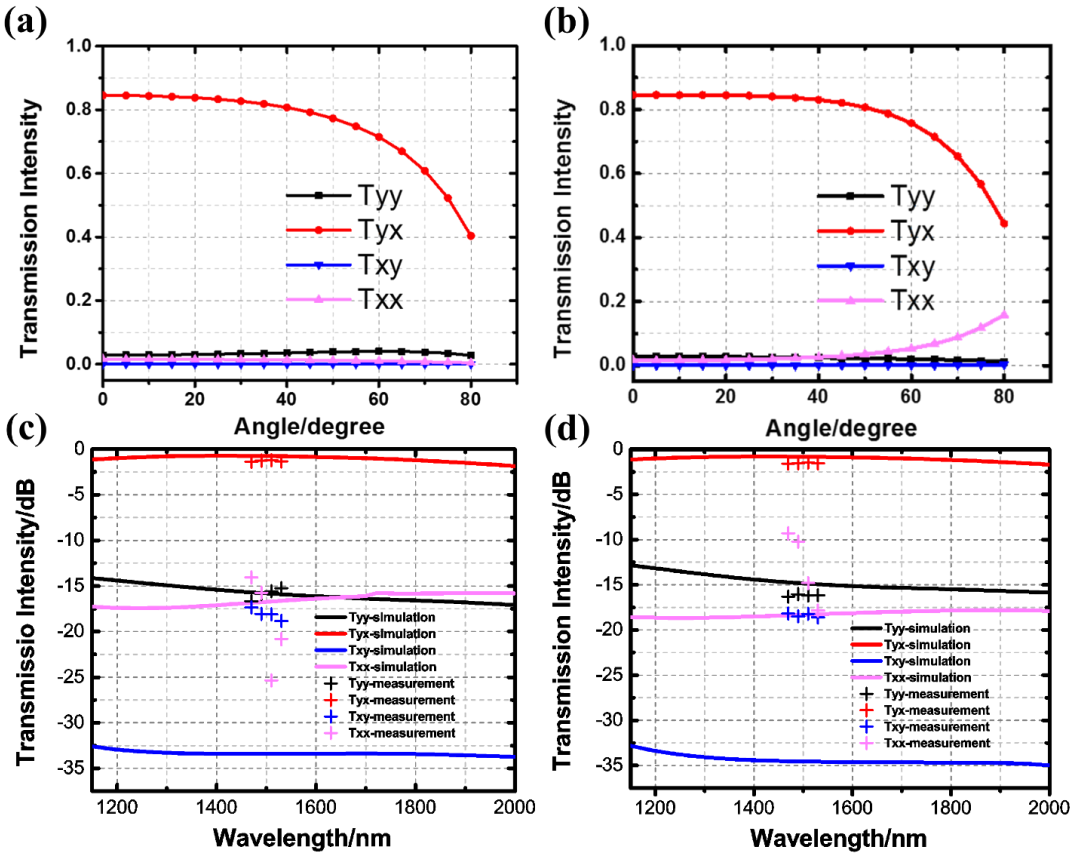

Figure 7.9: (a-b) Simulated transmittance at 1.5 μm with different values of angle of incidence in the XZ (a) and YZ (b) plane; (c-d) Measured transmittance with a 30° angle of incidence in the XZ (c) and YZ (d) plane.

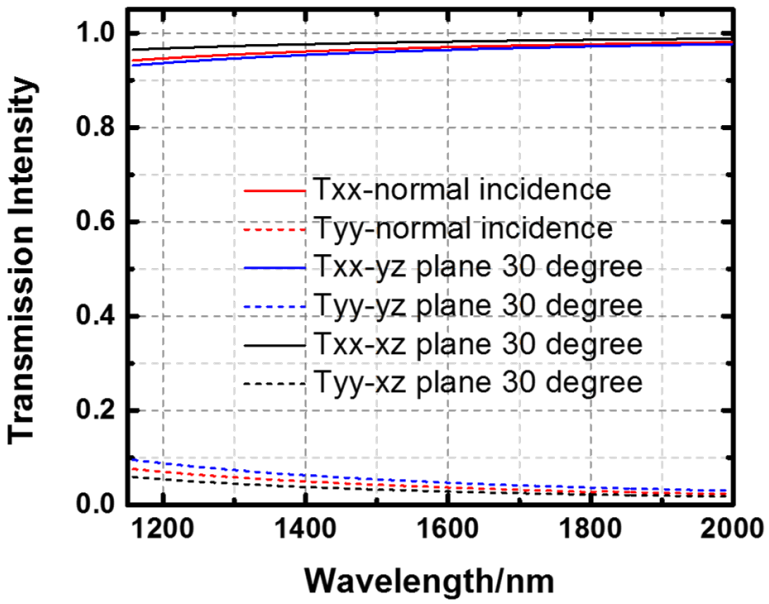

Figure 7.10: Normal transmission and angular transmission intensity from a single grating layer, which shows good angular tolerance behavior.

The metasurface is also insensitive to variations in the nano-grating width and period. Increasing or decreasing the grating width by 20 nm does not degrade its performance (Figure 7.11). Every individual layer functions as a linear polarizer (anisotropic element), and its anisotropic response will not change significantly with grating width variations over a certain range. In other words, these three layers of cascaded Au nano-gratings can be generalized as three layers of coupled anisotropic metallic sheets (Figure 7.12a). This response also suggests that the nano-grating period can be modified without sacrificing device performance.

To simulate all three Au nano-grating layers with identical geometries (period, linewidth and wire height), the middle Au nano-grating layer (140 nm period, 70 nm linewidth and

40 nm grating height) was simulated in the SU-8 surrounding dielectric environment first, and its transmission and reflection coefficients were extracted. Then, the middle layer inside the original metasurface HFSS model was replaced with an anisotropic sheet impedance having an optical response equal to that of the simulated structure. This allowed periodic boundary conditions to be used to simulate the response of the three layer structure with identical periodicities. It should be noted that this analysis assumes there is no evanescent coupling between the layers, which becomes more accurate as the layer spacing is increased and the periodicity is decreased.

The transmittance of the metasurface consisting of three identical layers of 40 nm thick, 70 nm wide, and 140 nm period Au nano-gratings is plotted in figure 7.12b, and is very similar to that of three layers of Au nano-gratings with a unique middle layer grating period in Figure 7.7a. Such a relaxation of the requirements on grating geometries (e.g. width and period) paves the way to realize large-area device fabrication for practical applications. It is true that sub-wavelength structures are usually fabricated through electron beam lithography, which is time consuming and makes it difficult to achieve large-area devices. However, for certain structures such as the nano-gratings in this study, they can be easily realized by various methods such as interference lithography [158], plasmonic lithography [159-161], or nano-imprinting [162-164]. The insensitivities of the device performance to variations in the grating geometry leave room for reasonable fabrication errors/inaccuracies.

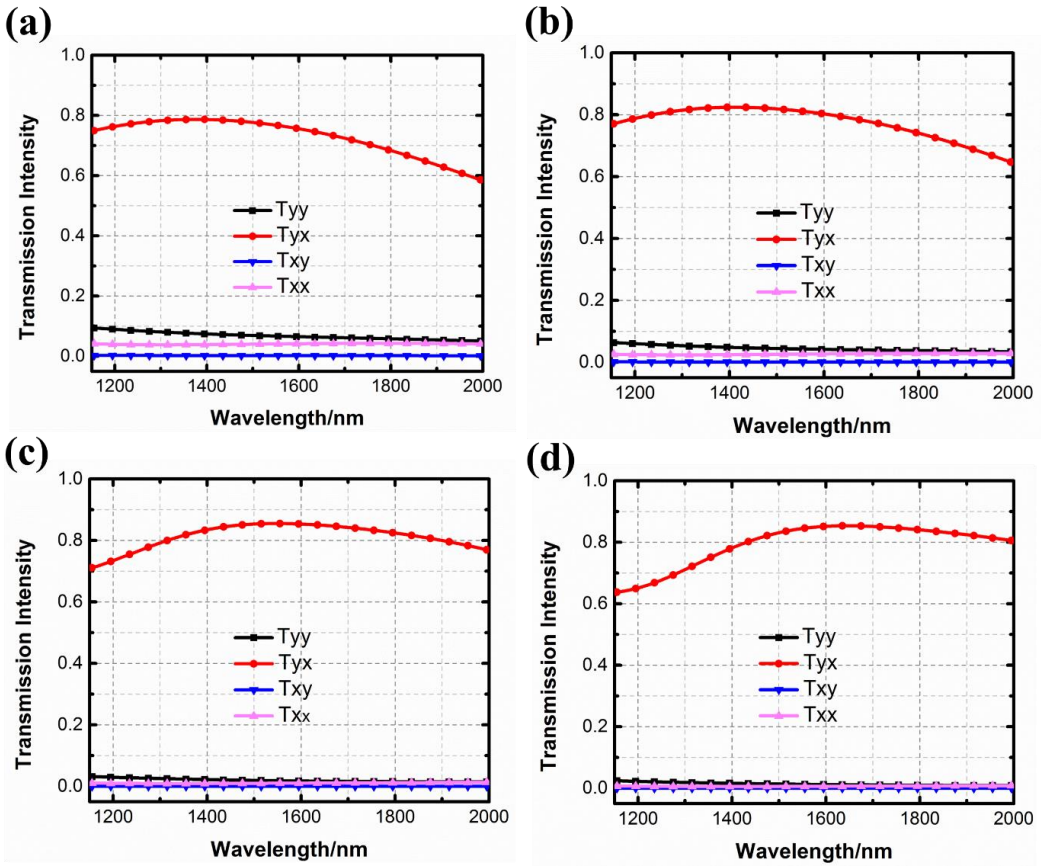

Figure 7.11: (a) Simulated transmittance when the grating width is reduced by 10 nm (60 nm, 90 nm, and 60 nm for the bottom, middle, and top layers, respectively). (b) Simulated transmittance when the grating width is reduced by 20 nm (50 nm, 80 nm, and 50 nm for the bottom, middle, and top layers, respectively). (c) Simulated transmittance when the grating width is increased by 10 nm (80 nm, 110 nm, and 80 nm for the bottom, middle, and top layers, respectively). (d) Simulated transmittance when the grating width is increased by 20 nm (90 nm, 120 nm, and 90 nm for the bottom, middle, and top layers, respectively).

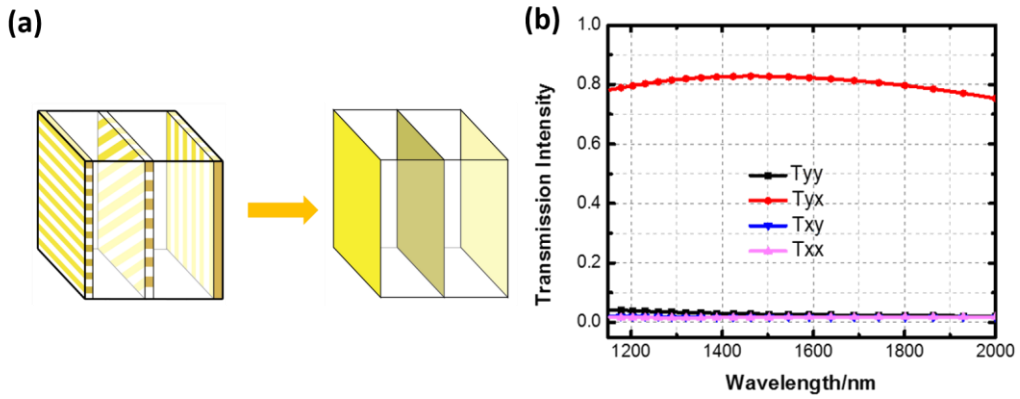

Figure 7.12: (a) Generalized model of the metasurface as coupled metallic sheets. (b) Simulated transmittance of metasurface with three layers of identical Au nano-gratings.

Further, the design strategy for the metasurface can be easily extended to other wavelength ranges to achieve asymmetric light transmission devices. One simple way is to modify the spacer layer thickness. As shown in Figure 7.13, asymmetric light transmission around 1 μm and 2 μm can be realized by setting the spacer thickness as 70 nm and 260 nm respectively. The detailed transmission characters of each design are plotted in figure 7.14. Moving the current design with Au to the visible regime will lead to a degraded performance, because of the high optical loss with Au in this wavelength range. Better designs can be achieved by choosing low-loss constituent materials in this wavelength range (e.g., Silver or Aluminum), and engineering the geometry of the constituent layers in order to achieve impedance matching with air and therefore, a suppressed reflection.

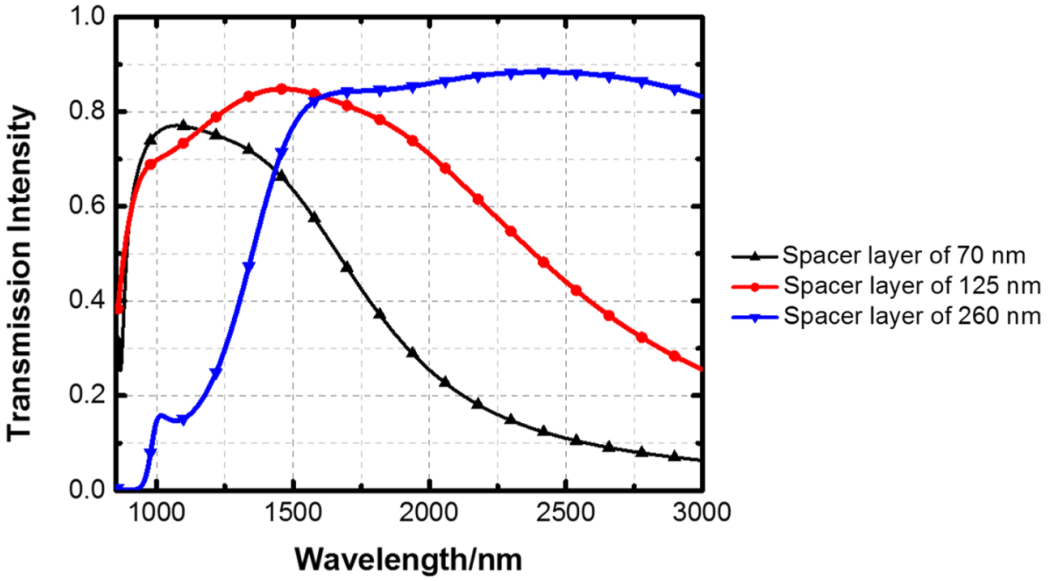

Figure 7.13: Adjusted transmittance of the metasurface by varying the nano-grating layer spacing.

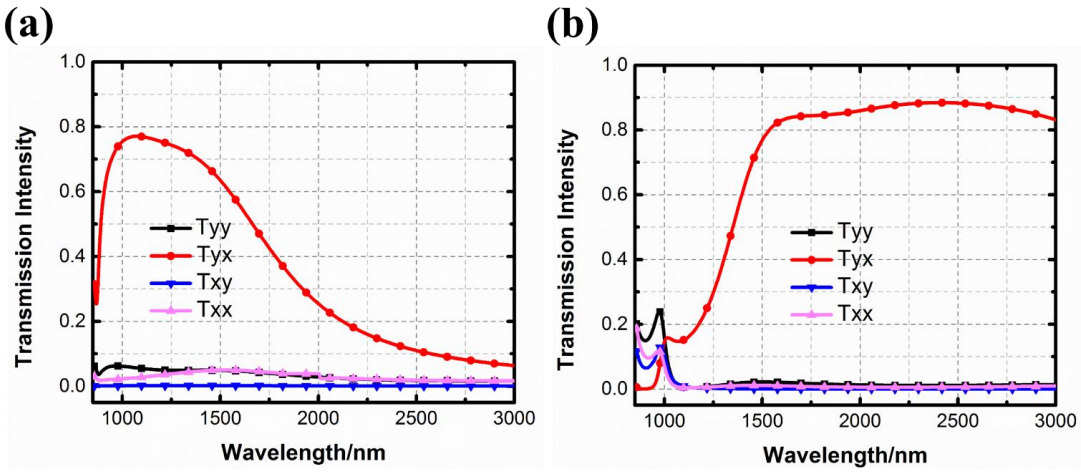

Figure 7.14: (a) Simulated transmittance of the metasurface with a 70 nm spacer layer thickness. (b) Simulated transmittance of the metasurface with a 260 nm spacer layer thickness

7.5 Conclusions

This chapter presents a thin (λ/5) asymmetric light transmitting metasurface. It has the advantages of high transmission (80%), broad bandwidth (FWHM bandwidth of 1.7 μm), and good extinction ratio (24; 13.8 dB). In addition, its performance is insensitive to both the incident light angle and the nano-structure geometric variations. The design principle is general and can be applied to other wavelength ranges. In addition, the device structure is suitable for large-area device manufacturing techniques such as a nano-imprinting or roll-to-roll printing.

Chapter 8

Printed Metasurface

8.1 Introduction

Future photonic and optoelectronic devices need to be compact in size for high-density on-chip integration. In addition, engineering their configurations at the micro- or nano-scale, i.e., photonic crystals and metamaterials, can improve exiting and create new device functionalities. These advances demand highly precise techniques to fabricate structures of various sizes using a wide range of materials at a low cost and high throughput.

So far, various micro- and nano-lithography techniques have been developed, many of which are driven by the continuous demands from the semiconductor industry to manufacture smaller transistors and denser integrated circuits. They can be roughly categorized into (a) photon-based lithography (optical lithography [165], deep-UV / extreme-UV lithography [166, 167], X-ray lithography [168], and plasmonic lithography [169]), (b) charged particle-based lithography (electron beam lithography [170, 171] and focused ion beam milling [172]), (c) printing-based lithography (nano-imprinting [162, 164] and micro-contact printing [173, 174]), (d) direct laser writing [175], (e) tip-based lithography (dip-pen lithography [176, 177] and thermal tip lithography [178]), and f) various self-assembly methods [179, 180].

Photon-based lithography is currently being widely used in industry, but their resolutions are limited by the light diffraction effect. To further increase the resolution, either light sources with shorter wavelengths and corresponding photo resists need to be developed, or other complex set-ups such as immersion type lithography needs to be used. At the same time, the lithography systems are getting more and more complicated with a decreasing feature size. Charge particle-based lithography (electron-beam, ion-beam) provides a high resolution, but suffers from issues, such as slow speed, low throughput, and complicated tool set-up. Moreover, patterning can only be performed over a limited area due to their intrinsic low speed. In comparison, printing-based lithography is compatible with rich groups of materials and they can be scaled to pattern structures over very large areas. Moreover, its throughput is high, and many of the printing methods do not reply on complicated tool designs, making the fabrication highly efficient and inexpensive.

Nanoimprint lithography (NIL) is an important member of the printing-based lithography family. It was proposed in the 1990s by Stephen Chou and his co-workers [181, 182]. The technique was a modification of the manufacturing process of compact disks and was similar to a molding process developed by Japanese researchers in the 1970s [183]. However, in the nineties, the semiconductor industry was struggling to shrink the lateral patterning dimensions in order to keep up with Moore's law. Therefore, nanoimprinting's demonstration of 10 nm feature sizes instantly made it a promising alternative to expensive UV optical lithography.

Although NIL has been in existence for over 20 years, several critical issues are still being identified and solved so that it can be employed in the highly demanding semiconductor industry. Firstly, NIL is conducted with a 1x mask (typically called the imprinting mold / template). Therefore, in order to perform NIL, an expensive and high precise mask needs to be prepared first. Also, NIL is a contact process, wherein defects can easily be generated and pattern distortions can happen during the mold/substrate separation (de-molding) process. Moreover, there is usually a residual layer on the substrate after NIL, which needs to be removed before subsequent processing. However, the above constraints can be well tolerated by other applications such as photonics, magnetics (e.g. patterned media), sensors, micro-/nano-fluidics, and biology. Indeed, NIL's high resolution, great repeatability, low cost, and virtually unlimited throughput ability make it an advantageous approach for both research prototype fabrication and large-volume product manufacturing for these applications.

In this chapter, nanoimprinting is utilized as an efficient and cost-effective technique for fabricating metasurfaces. Metasurfaces are sub-wavelength textured surfaces that can be thought of as the two-dimensional equivalent of metamaterials. By properly choosing their constituent nano-antennas' materials and geometries, versatile light property (spectrum, direction, and polarization) control has been demonstrated. The two-dimension nature of metasurfaces corresponds well with nanoimprint lithography (NIL), which patterns nanostructures over a plane. Imprinting has numerous advantages including simplified fabrication, high resolution, great fidelity, and increased throughput. Also, this method is

capable of processing various kinds of materials on diverse substrates. All these unique features enable high performance printed photonic devices. As an example, a printed dielectric metasurface is demonstrated and it has the function to convert a linearly polarized input to a radially polarized output.

8.2 Design

The metasurface is made of poly-Si, which has a negligible light absorption at its working wavelength (1500 nm). The unit cell consists of 1D Si gratings on a fused silica substrate, and the grating has a height of 400 nm, width of 180 nm, and period of 800 nm. It is worth noting that the Si layer thickness is much smaller than the working wavelength of the metasurface. However, with a proper design here, light polarized perpendicular to the grating direction (TE) will excite a fundamental electric resonance inside the Si gratings, while light polarized along the grating direction (TM) will excite a second order magnetic resonance inside the grating [147]. The difference in the resonance behaviors for TE and TM light leads to a π phase difference upon their transmission, while at the same time, similar transmission intensities (figure 8.2). Therefore, the Si grating works as an efficient nano-size half waveplate.

In order to convert a linearly polarized incident light (along the y-axis) into a radially polarized light upon transmission, the principle axes of the nano-size half-wave plates need to be placed according to their azimuthal positions over the plane. As shown in figure 8.1b, for a nano-size half-wave plate which has an angle of α with the x-axis, its slow axis needs

to have an angle of β with respect to the x-axis. Angle α and β are related by the following relation: $\beta = \frac{\pi}{4} + \frac{\alpha}{2}$. In this way, such a nano-size half-wave plate will flip the polarization of a linearly polarized light (along the y-axis) with respect to its slow axis, and therefore, generates a transmitted light polarized along the radial direction.

Figure 8.2 depicts the layout of the nano-size half-wave plates over the plane, where their period is fixed as 800 nm. The antennas' orientations are set as constant values every 5˚ along the azimuthal direction. Except for the tiny central part where the nano-antennas are arranged in an irregular fashion, areas away from the central part have antennas locally arranged in a regular 1D grating geometry. Consequently, such a "gradient" 1D grating maintains the antenna's function as a half-wave plate.

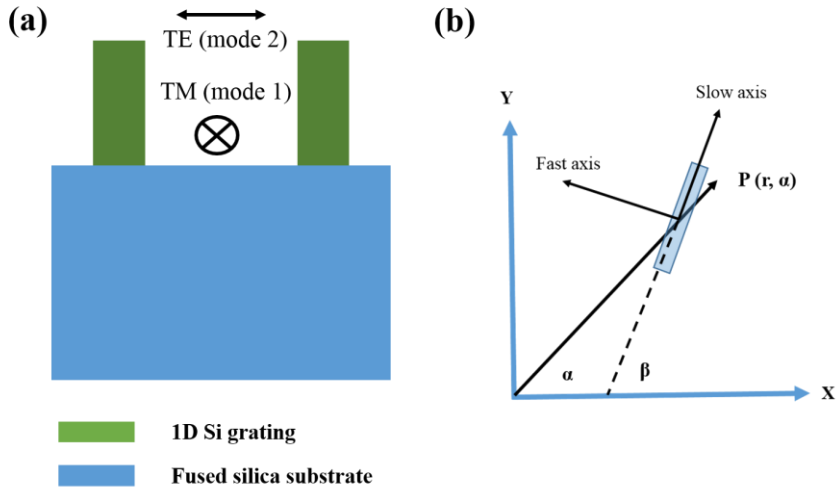

Figure 8.1: (a) Schematic drawing of the cross-sectional view of the Si metasurface. (b) Schematic drawing of a rotated Si nano-bar with a rotation angle according to its azimuthal position.

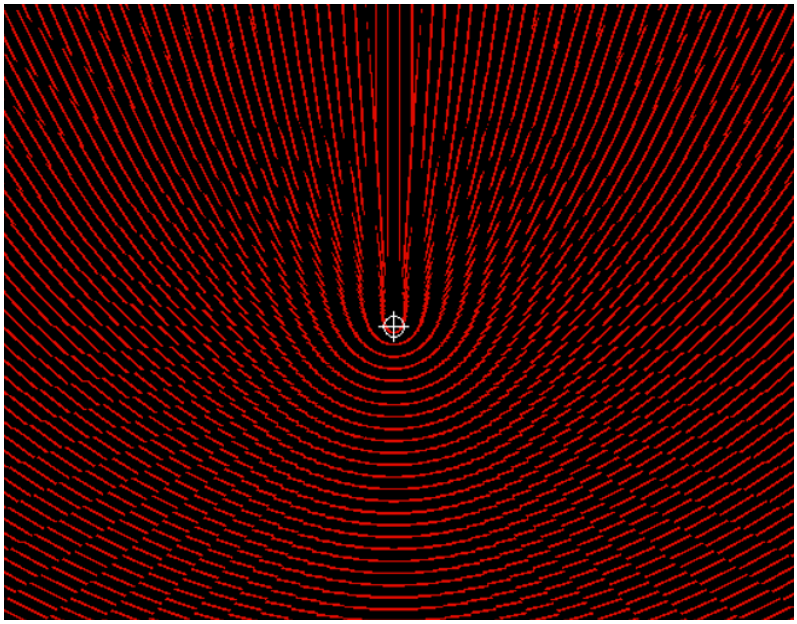

Figure 8.2: Schematic of the layout of the nano-antennas whose orientations are rotated gradually over the plane.

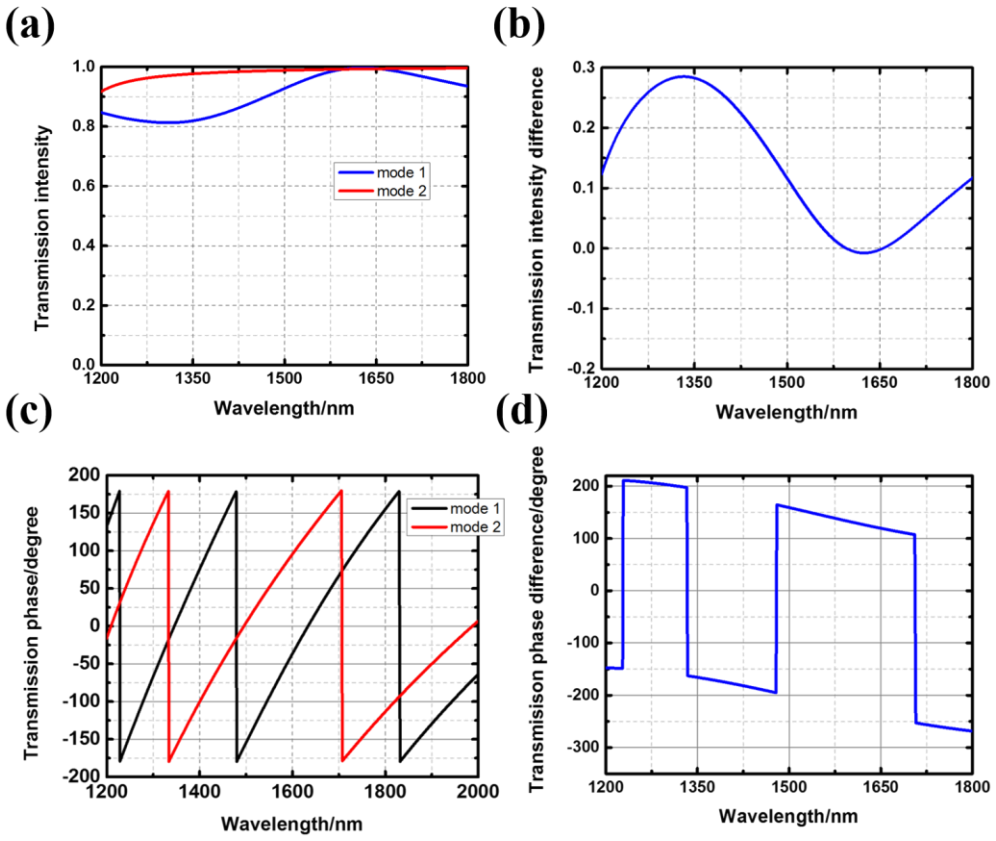

Figure 8.3: (a) Transmission intensities of the two modes through the 1D Si grating. (b) Transmission intensity difference of the two modes through the 1D Si grating. (c) Transmission phases of the two modes through the 1D Si grating. (d) Transmission phase difference of the two modes through the 1D Si grating

8.3 Fabrication and characterization

The imprint mold is fabricated on a silicon wafer. Electron beam lithography is employed to define the metasurface patterns on ZEP 520a resist and the patterns are transfer onto the Si wafer by Si etching. A 400 nm thick, poly-Si layer is deposited on a fused silicon substrate using a low pressure chemical vapor deposition (LPCVD). Mr-I 8030 is chosen as the thermal imprint resist. After the patterns are printed onto the mr-I resist, a short time

oxygen plasma etching is applied in order to remove the residual mr-I layer formed in the imprinting step. Afterwards, the patterns are transferred down to the poly-Si layer beneath through Si etching. The fabricated sample is 1 mm by 1 mm in size. Figure 8.4 shows the SEM picture and the optical microscope picture of the imprinted Si metasurface.

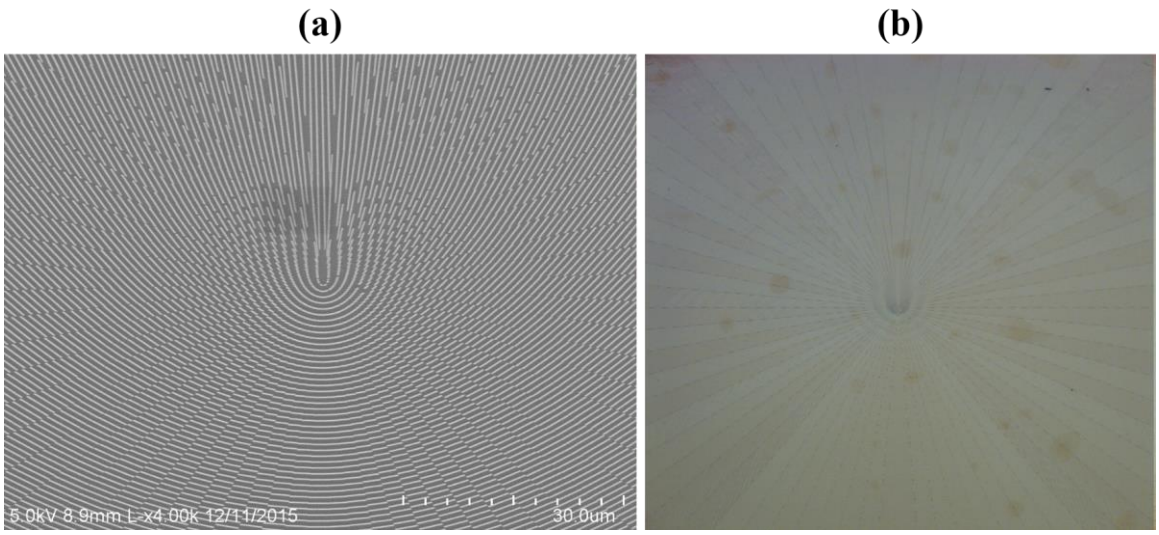

Figure 8.4: (a) a SEM picture of the imprinted Si metasurface. (b) An optical microscope picture of the device with a 1 mm x 1 mm area.

In order to characterize the device's performance, a lineally polarized light along the vertical direction is send through the metasurface, which goes through a linear polarizer and is finally collected by an optical power meter. The linear polarizer transmission axis is rotated over 180°, and the transmission intensity after the polarizer is recorded every 10°. It can be seen that the output intensity remains flat along with the polarizer's rotation, a direct evidence of the radially polarized output beam. Note that 32˚ corresponds to the linear polarizer transmission axis along the vertical direction. Finally it is worthwhile to

note that the fabrication process is CMOS-compatible, and is applicable to fabricate various dielectric metasurfaces to replace conventional bulky optical systems.

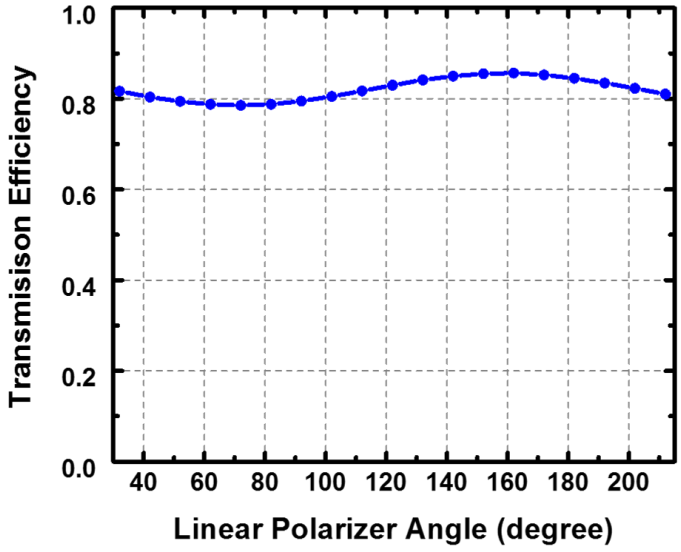

Figure 8.5: Measured transmission intensity through the metasurface with respect to different orientations of the polarizer transmission axis. Note that 32˚ corresponds to the linear polarizer transmission axis along the vertical direction.

8.4 Conclusions

This chapter presents a printed dielectric metasurface for converting a vertically polarized input light into an axially polarized output light. Metasurfaces are sub-wavelength textured surfaces that can be thought of as the two-dimensional equivalent of metamaterials. Such a two-dimension nature of metasurfaces corresponds well with the nanoimprint lithography (NIL), which patterns nanostructures over a plane. NIL has the advantages of simplified fabrication, high resolution, great fidelity, and increased throughput, thus providing an

efficient and cost-effective method to fabricate metasurfaces. The design methodology and fabrication technique developed in this work are applicable to various metasurface structures.

Chapter 9

Ultra-broadband and Highly Sensitive Optical Ultrasonic Detector for Photoacoustic Imaging

9.1 Introduction

Photoacoustic imaging (PAI), an elegant combination of light and sound, has been employed in various areas, such as laser ultrasound inspection [184-186], photoacoustic microscopy/tomography [187, 188], and more recently, pulsed THz detection and imaging[189]. In PAI, a short laser pulse is used to illuminate the light-absorbing objects and ultrasound signals are generated via the thermal-elastic expansion [190]. The signals are subsequently collected by ultrasound detectors and used for either image construction [191, 192] or qualitative analysis [193, 194].

Spatial resolution is one of the key parameters in PAI, in both lateral and axial dimensions. The existing PAI systems have demonstrated lateral resolution comparable to that of optical microscopy on the scale of micron or even sub-micron [195-198] by fine optical focusing. In sharp contrast, the axial resolution remains around 15-20 μm [199, 200], similar to that of high-frequency ultrasound imaging and more than one order of magnitude worse than the lateral spot size of PAI. The resultant asymmetric and severely distorted minimum voxel has a detrimental effect on the 3D imaging capability of PAI. The axial

resolution is essentially determined by the sharpness of the detected acoustic pulse and can be described by the equation: R = 0.88C/BW [201], where R is the axial resolution, C the sound speed, and BW the detector FWHM bandwidth. Since C is a constant in most soft biological tissue, R is primarily determined by the detector's bandwidth.

Conventional ultrasonic transducers almost exclusively use piezoelectric material, either inorganic (e.g., piezoceramic materials) [202, 203] or organic materials (e.g., polyvinyldenefluoride/PVDF) [204]. Piezoelectric transducers are usually operated over a band of frequencies centered at their resonance where the thickness of the piezoelectric crystal equals to half of the acoustic wavelength. Thus high-frequency transducers require thin crystals, which results in demanding fabrication challenges and robustness issues from the fragile films [205]. Moreover, a broad bandwidth covering from nearly DC to very high frequencies is essential to subsequent faithful image reconstructions [206], but it is not easily obtainable with a single piezoelectric transducer due to the above mentioned resonant effect. To overcome such limitations, multiband photoacoustic imaging is developed, where multiple ultrasound detectors with different central frequencies are used to collect signals from the corresponding bands in a broad frequency range [207, 208].

As an alternative to the finite bandwidth limitation on the detector side, researchers have obtained a 7.6 μm axial resolution with a commercial 125 MHz ultrasound transducer by applying the de-convolution method [201]. However, this method is sensitive to noise and therefore, has limited applications. Another approach is to apply slow-sound silicone oil

around the imaging target to improve the axial resolution [209], but the biological compatibility of silicone oil needs to be further evaluated.

Ultrasound detection by optical methods is a promising field, where a structure with certain optical resonances is employed and its resonant behavior is modulated by the ultrasound waves. One popular optical ultrasound detector is the Fabry-Perot polymer film transducer [210-212]. Its cavity length is typically 25-50 μm in order to provide enough finesse (sensitivity), which limits the bandwidth to tens of MHz. Shelton, *et al.* reported a novel approach to use optical nonlinearities to confine the spatial resolution in both the lateral and axial dimensions, and demonstrated an axial resolution of 6 μm [213]. But this technique uses a complicated set-up and has issues with the difficulty of miniaturization, limited imaging speed, and potential tissue damage.

Apart from bandwidth, detector sensitivity is another important factor to consider. Since the attenuation of an ultrasound wave is proportional to the square of its frequency, a high frequency component attenuates strongly with distance, e.g., a 300 MHz acoustic wave attenuates at a rate of ~20 dB/mm in water and ~80 dB/mm in tissues [195]. Unfortunately, noise level increases proportionally with bandwidth at the same time. Therefore, in order to collect high frequency photoacoustic signal effectively, a sensitive ultrasound detector is necessary.

This chapter reports on an ultrasound detector based on nanoimprinted polymer microring resonators with an ultra-broad bandwidth from DC to ~350 MHz at -3dB and an ultra-low noise equivalent detectable pressure (NEP) of 105 Pa over this 350 MHz band. The microring has a high quality factor on the order of 10^5, and such a sharp resonance lays the foundation for sensitive acoustic detection. The minimized thickness of the microring waveguide is responsible for its ultra-broad bandwidth frequency response. An unprecedented sub-3 μm axial resolution is demonstrated experimentally by imaging two closely-spaced Chromium films. This study demonstrates polymer microring resonator as a high performance ultrasound detector for photoacoustic imaging with ultra-broad frequency response and high sensitivity.

9.2 Device fabrication and characterization

The polymer microring was fabricated by nano-imprinting of polystyrene (PS) film using a silicon mold (figure 9.1a). The imprinting process simplifies fabrication, increases throughput, and improves reproducibility [162]. The silicon mold fabrication started with electron beam lithography (E-beam) to define the microring and the bus waveguide patterns on the E-beam resist first. The E-beam resist was polymethyl methacrylate (PMMA). After the E-beam resist development, a thermal reflow process (115 °C, 90 s) was applied to reduce imperfections in PMMA and harden its edge. Then the PMMA was used as the mask in plasma coupled reactive ion etching (RIE) to transfer the pattern onto silicon. At last, the PMMA was removed by acetone which concludes the mold fabrication

process [214]. Then the silicon mold was employed in a thermal imprinting process (180°C for 5 minutes) on polystyrene (PS) film (Nanonex 2000).

The device consists of a ring resonator coupled with a bus waveguide. The ring has a diameter of 60 μm and height of 1.4 μm (figure 9.1c and d). Resonant dips in the transmission spectrum occur when the round-trip phase delay in the ring equals to multiples of 2π radians. Figure 9.1b shows the measured optical transmission spectrum from the device. It has a resonance bandwidth of 6 pm, corresponding to a quality factor (Q factor) of 1.3×10^5. When the probing laser wavelength is fixed at the sharpest slope of the ring resonance curve, the incoming ultrasound signal can be recorded by a varying output light intensity from the microring resonator due to the resonance shift.

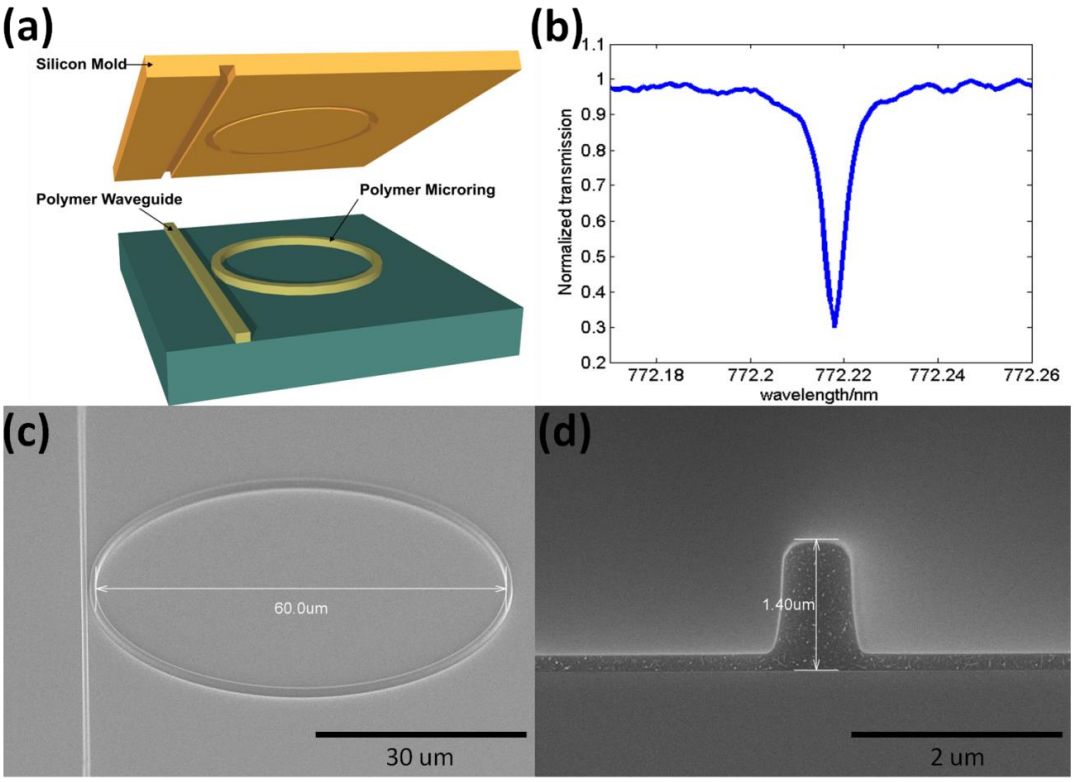

Figure 9.1: (a) Schematics of the polymer microring fabrication by the nano-imprinting lithography. (b) Optical transmission spectrum of the polymer microring resonator. The resonance FWHM is ~6 pm. (c) Angle view scanning electron microscope (SEM) of the microring with a diameter of 60μm. (d) Side view SEM picture of the ring with a height of 1.4μm.

The experimental setup for investigating the device acoustic bandwidth is shown in figure 9.2a. A continuous-wave (CW) 780 nm tunable laser (TLB-6312, New Focus) was fiber coupled into the device's input waveguide and its output power was collected by a multimode fiber, which was connected to a 1×2 coupler with 90:10 split ratio (FCMM50-90A-FC , Thorlabs). The outputs of the coupler were detected by two photo-detectors and finally recorded by a digital oscilloscope (DSO7054A, Agilent). To lock the probing wavelength at the sharp slope of the ring resonance spectrum, output from the 10% channel

of the coupler was monitored (1601, New Focus) and used for feedback control of the tunable laser. The remaining 90% output was collected by a high-speed avalanche photo detector (APD210, Menlo Systems) and used for photoacoustic signal detection. The reason to collect as much output power for photoacoustic detection is because the detection sensitivity is usually proportional to the probing optical power [215]. The device was immersed in de-ionized (DI) water which served as both the top cladding of the microring and the coupling medium for the ultrasonic propagation.

To determine the intrinsic bandwidth of the microring resonator, a narrow (broadband) acoustic pulse was needed. This was accomplished by photoacoustic signal generation, where a 1.5 ns pulse duration, 337 nm laser pulse (GL-3300, Photon Technology International) was used to illuminate a 200 nm thick chromium (Cr) film with ~4 mm spot size. In the case where the laser pulse duration is far longer than the acoustic transient time across the absorber, the generated photoacoustic signal essentially duplicates the incident laser pulse in the time domain [216].

Figure 9.2b shows the time-domain laser pulse and the photoacoustic signal detected by the microring, using the same high speed photodetector. The full width half maximum (FWHM) of the laser pulse is 1.5 ns and that of the photoacoustic signal is 1.8 ns. The photoacoustic signal was obtained from a single laser pulse without any averaging. A ~20 μm water gap between the Cr film and the microring resonator was determined through the propagation time of the generated acoustic signal. The frequency response of the microring

detector is plotted in figure 9.2c, where the compensation for the water acoustic attenuation is taken into account. As can be seen, a flat response stretching from DC to ~350 MHz at -3 dB (0.707) was obtained. Such a wideband and flat spectral characteristic can tremendously enhance the axial resolution in photoacoustic imaging, as shown later. Calculation of the frequency response is described as follows.

The measured photoacoustic signal by the microring detector in the frequency domain can be expressed as follows:

$$F_{signal} = F_{laser} \times F_{water} \times F_{ring} \times F_{detector}$$

In which, F_{signal} is the detected photoacoustic signal, F_{laser} is the laser signal, F_{water} is the water frequency-dependent transfer function and represents different attenuations for different frequency components. F_{ring} is the frequency response of the microring, and $F_{detector}$ is the frequency response of the photo detector. All the parameters are in the frequency domain.

The microring frequency response can be calculated by:

$$F_{ring} = \frac{F_{signal}}{F_{laser} \times F_{detector} \times F_{water}}$$

A 20-μm propagation distance in water, which is the gap between the Cr film and the microring in experiment, was used in the calculation of F_{water}. By measuring the laser signal with the same photo detector, $F_{laser} \times F_{detector}$ as a whole can be determined.

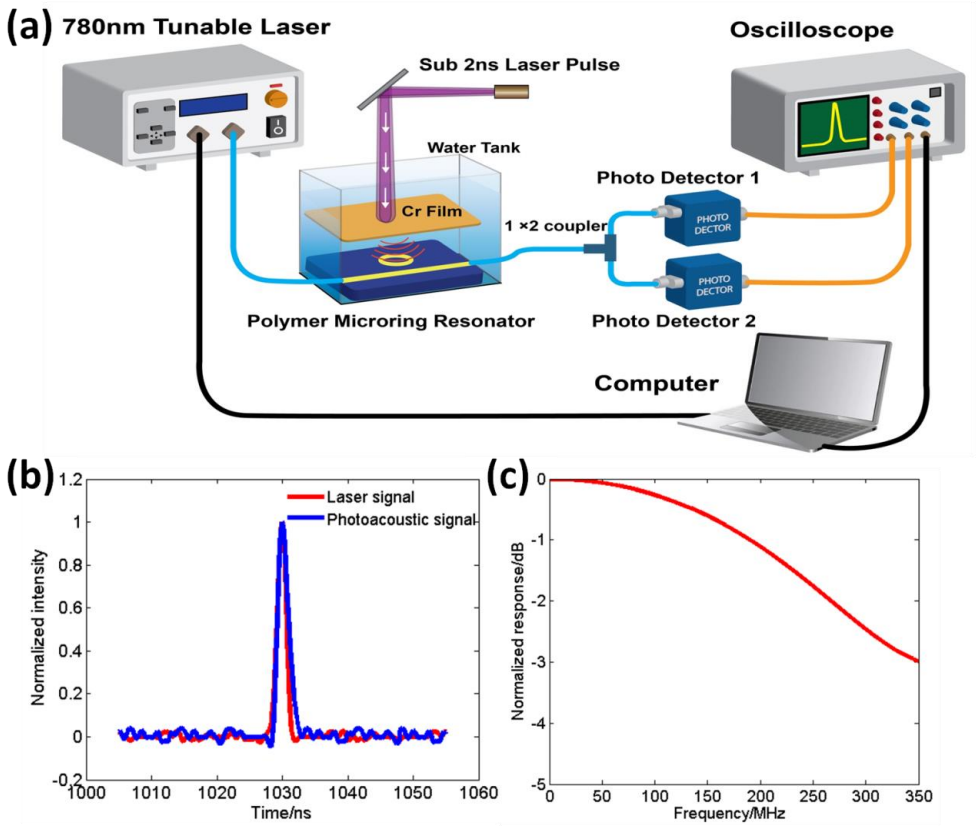

Figure 9.2: (a) Experimental set-up to determine the bandwidth of the ring resonator. (b) Experimentally measured laser signal (FWHM=1.5 ns) and photoacoustic signal (FWHM=1.8 ns) in the time domain. (c) The microring response spectrum in the frequency domain. The ring has -3dB bandwidth at 350 MHz.

The detector's acoustic sensitivity was calibrated using the same set-up but the Cr film was replaced by a pre-calibrated 20 MHz unfocused transducer (V316, Panametrics NDT) as the acoustic source. It was driven by a 2 V peak-to-peak one cycle 20 MHz sinusoidal wave with an output peak pressure of 6 KPa. The device produced an output peak voltage of 120.3 mV without any averaging, corresponding to a sensitivity of 20.05 mV/ KPa. The RMS noise level is 2.1 mV over the 1-350 MHz, leading to a NEP of 105 Pa. To the best

of the author's knowledge, this is the first time that low noise equivalent detectable pressure with a broad bandwidth of up to 350 MHz has been achieved. Further reduction of the NEP is possible by increasing the device Q factor, using higher probe laser power, and increasing the photo detector gain with low noise base.

9.3 Ultrahigh axial resolution

In figure 9.2b, the measured photoacoustic signal has a FWHM of 1.8 ns. Considering the sound speed of 1500 m/s in tissue, a time duration of 1.8 ns translates to a 2.7 μm axial resolution. Since the photoacoustic signals from objects at different locations add to each other in amplitude, objects with a separation less than 2.7 μm could still be distinguished. The system axial resolution could be estimated by shifting and summing the amplitude of two photoacoustic signals detected at a certain time interval, and checking if the peaks can be distinguished (i.e. Rayleigh criterion). Zhang *et al.* define the difference in the signal envelope between the smaller of the two peaks and the valley as the contrast, and the contrast-to-noise ratio (CNR) decreases as the distance between the two signals reduces [201]. The axial resolution is determined when CNR reaches 6 dB. Using this method, the CNR is plotted as a function of shift distance (figure 9.3a), based on the detected photoacoustic signal in figure 9.2b. The CNR reaches 6 dB with a separation of 1.9 μm, showing the potential of <2 μm axial resolution in photoacoustic imaging using the microring detector.

Due to the limited laser pulse width and photo detector bandwidth/sensitivity, the microring response at -6 dB cannot be directly characterized. A Gaussian function is used to extrapolate the ring response spectrum, shown in figure 9.4. The ring is expected to have a -6 dB bandwidth at 470 MHz. This leads to a detector FWHM bandwidth of 940 MHz. Applying the formula R = 0.88C/BW gives an axial resolution of 1.4 μm, which corresponds to the result from the "shift and sum" method.

As an experimental demonstration, the single Cr film was replaced by two Cr films separated by a thin SU8 spacer. The Cr films are of thickness 40 nm and 160 nm respectively, and the SU8 layer is about 5.9 μm. The films are deposited on a Polyethylene terephtalate (PET) substrate, which has a matched acoustic impedance with water [209]. No reflected acoustic wave from the substrate was observed in experiment. The detected signal is shown in figure 9.3b. Clearly two peaks can be distinguished with 1.9 ns separation with a CNR of 15 dB. A 1.9 ns time domain gap directly translates to 2.85 μm axial resolution in biological tissues (sound velocity 1500m/s in tissues), consistent with the previous estimation based on the pulse width of the photoacoustic signal detected by the microring. This value is about a two-fold improvement over the recent reported results [209],[213], but without any signal processing or sample treatment. An initial experiment using the microring in a photoacoustic microscopy system also shows improved axial resolution as compared with a traditional transducer [217].

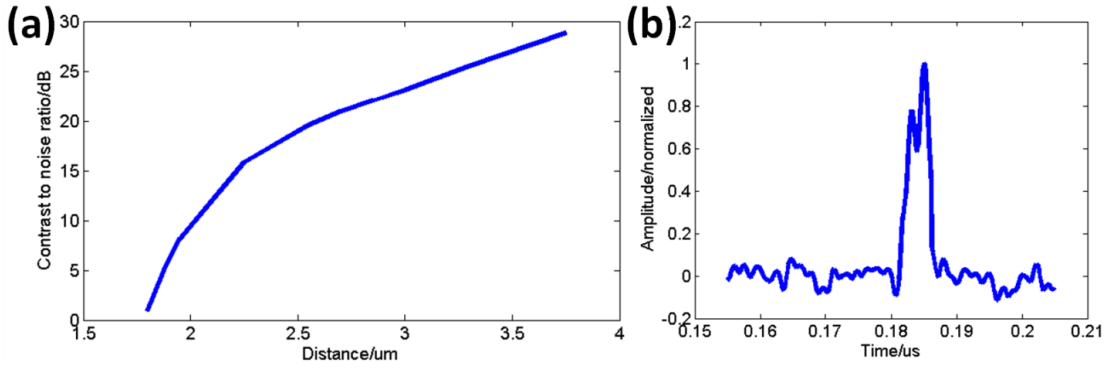

Figure 9.3: (a) Contrast to noise ratio (CNR) as a function of the delay distance. It reaches 6 dB at 1.9um (axial resolution estimation). (b) Photoacoustic signals of two closely spaced Cr films with 1.9 ns separation in time domain, which is a direct experimental demonstration of the super high axial resolution (2.85 um).

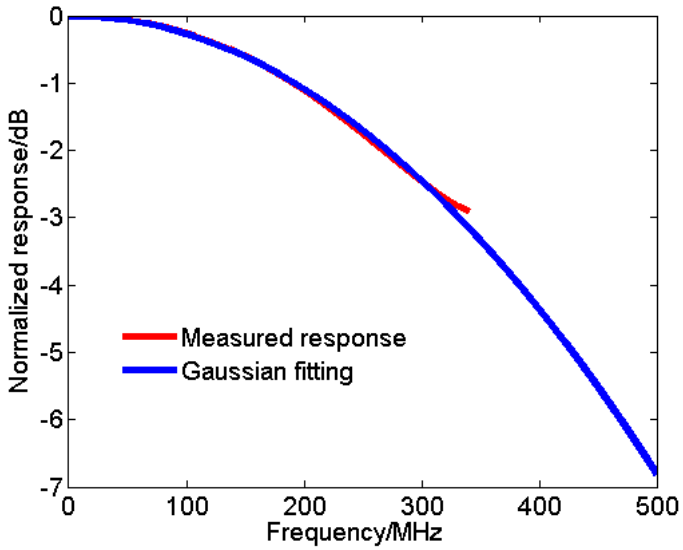

Figure 9.4: Ring frequency response spectrum and its Gaussian functional extrapolation, showing the detector -6 dB response at 470 MHz, and the detector FWHM bandwidth as 940 MHz.

9.4 Theoretical analysis of the frequency response

First of all, the detector acoustic response bandwidth is limited by the cavity optical bandwidth, which is determined by the inverse photon lifetime in the cavity (ν/Q) [218], where ν is the operating frequency and Q the quality factor. This upper frequency limit, calculated to be ~18 GHz in the polymer microring case, is far beyond the frequency range for PAI (a few hundred MHz).

From the acoustic interaction point of view, the microring resonator is modeled as a vertical acoustic Fabry Perot (FP) cavity for the incident acoustic pulse [219]. The active region is the polystyrene (PS) waveguide core bounded by the water and the silicon dioxide (SiO_2) substrate. The microring height is 1.4 μm. In this acoustic cavity, due to the smaller/comparable lateral size of the polystyrene waveguide to the ultrasound wavelength, acoustic scattering effect cannot be neglected. For estimation, plane wave propagation inside the polystyrene (PS) waveguide is assumed. The incoming pressure partially transmits into this FP cavity and bounces back and forth between the two boundaries. This leads to an acoustic wave amplitude distribution inside the PS waveguide region along the vertical direction. Such distribution is integrated over the whole waveguide core area to have an effect in modulating the waveguide property and the ring resonance behavior [219].

Similar to an optical FP cavity, the cavity length of this acoustic FP roughly determines its response bandwidth. The amplitude of the accumulated acoustic field inside the PS

waveguide can be calculated as a function of frequency. The greater acoustic field accumulation, the stronger it would influence the PS waveguide property and the ring resonance behavior. It is worth noting that the distribution of optical field intensity inside the core of the microring optical waveguide is not uniform. For the fundamental optical mode, the field has a high intensity in the center and a low intensity near the boundaries. Therefore, for a more accurate evaluation, the optical field distribution in the PS core was taken into account as a weighting factor in calculating acoustic field accumulation's effect on the PS waveguide property. In other words, optical field distribution acts as a "weighting factor" in analyzing the device acoustic frequency response. However, how the optical field distribution would affect the device acoustic response is a complex problem by itself. In this estimation, the optical field distribution in the vertical direction of the waveguide center is used as the "weighting factor" and this is in line with the plane wave approximation.

Figure 9.5a shows the optical field distribution for TE mode, as in the case of the experiment (TM has similar results). Figure 9.5b shows the simulated and the measured frequency response spectra. The simulated response has a -3 dB response at 315 MHz and the measured one has -3 dB response at 350 MHz. Also, there are differences in their curve shapes. The discrepancy can be attributed to factors, such as the plane wave approximation we used, how the optical filed distribution is taken into account, as well as material parameters used in the simulation.

The acoustic impedances used in the acoustic bandwidth simulation for water, PS and SiO_2 are 1.49×10^6 Kg/(s•m^2), 2.47×10^6 Kg/(s•m^2), and 1.31×10^7 Kg/(s•m^2) [220], respectively. For the optical field profile calculation, the refractive indices for water, PS and SiO_2 are 1.33, 1.578, and 1.46 respectively [221].

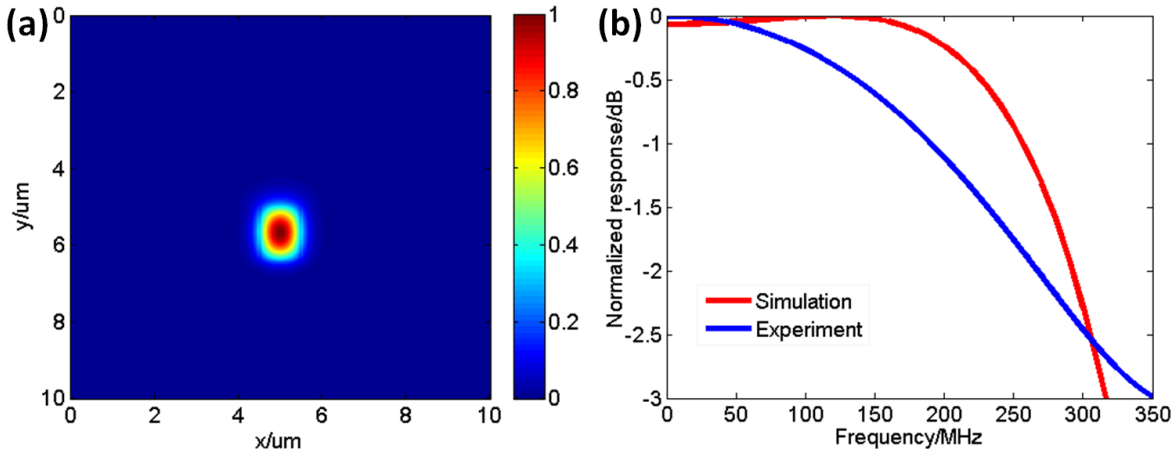

Figure 9.5: (a) Simulated transverse electric (TE) mode distribution; (b) Comparison of simulated and measured frequency response.

In the case of planar Fabry-Perot polymer film ultrasound detectors, the film thickness is typically chosen as 25-50 μm in order to guarantee a high finesse (thus a high detection sensitivity), which limits the detector bandwidth to tens of MHz based on a similar analysis discussed above. In sharp contrast, the microring resonator is able to maintain its high Q factor (high sensitivity) and broad bandwidth simultaneously. Therefore, it possesses both a broad bandwidth and low NEP. The microring is an ideal detector for photoacoustic tomography, where objects of different sizes generate photoacoustic signals with different central frequencies [222]. The microring could effectively collect all signals as a single

element, alleviating the complexity of employing multiply detectors such as in the case of multiband photoacoustic tomography. Therefore, the polymer-based miniature size microring resonance structure provides an advantageous approach for both broadband and sensitive ultrasound detection.

9.5 Real time THz pulse detection

Terahertz (THz) sensing plays an important role in industry, biology, and material science. Most existing techniques for THz detection either require bulky optics or need cryogenic cooling, and the un-cooled thermal detectors usually suffer from a long integration time. A novel scheme based on photoacoustic detection of THz (PADTH) pulse radiation is proposed and experimentally demonstrated [223, 224]. According to the previously mentioned description of the photoacoustic effect (the production of acoustic signals by any forms of electromagnetic radiation), the energy of individual THz pulses can be converted to acoustic waves with a proper absorbing and thermal expansion medium (carbon nanotube-PDMS composite in this case). In PADTH, the transient and localized heating in the carbon nanotube-PDMS composite by the absorption of THz pulse energy produces ultrasound, which is subsequently detected by a highly sensitive microring acoustic sensor (figure 9.6a).

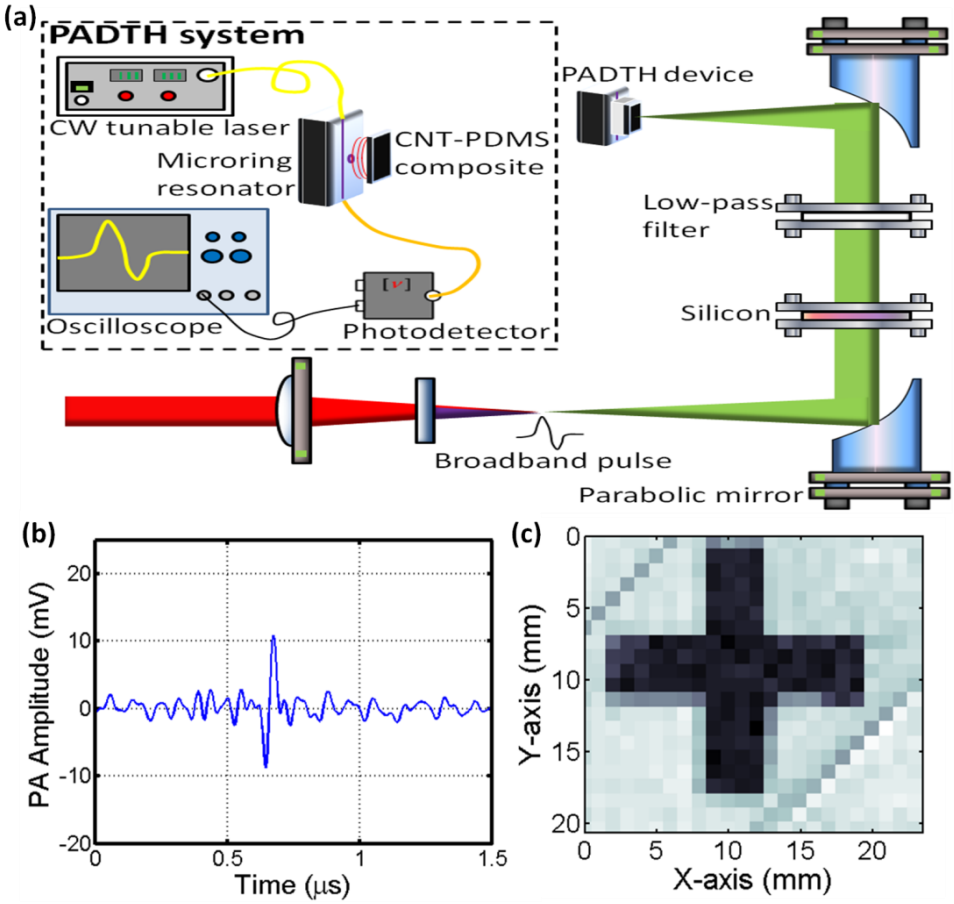

Figure 9.6: (a) Experimental set-up of the PADTH system; (b) Detected photoacoustic signal from signal THz pulse, signifying the system real-time response capability. (c) A THz image by PADTH system.

Different from the conventional thermal detectors utilizing continuous heat integration, this new method of THz detection responds to the energy of each individual THz pulse, enabling real time detection and imaging (figure 9.6b and c). The detection speed of PADTH system is determined by the time to generate a photoacoustic signal and the detected acoustic signal duration. In this case, the detected acoustic pulse duration dominates, resulting in a response time of less than 0.1 μs. In contrast, bolometers reply on

the electric resistance change with respect to the temperature variation and the response time is about 0.1 ms. What is more, bolometer operation usually requires cryogenic cooling that limits their wide applications. Pyroelectric detectors work at room temperature, but their response is even slower (~0.1s) [223]. Electro-optical sampling can detect THz pulse at a fast speed, but the system is bulky [225]. Broadband THz absorption is possible by the extraordinary absorption of CNT-polymer composite across a wide spectrum range [226-228]. Besides, this method offers additional advantages of room-temperature operation, compact system size, robustness against ambient noise, etc.

9.6 Conclusions

This chapter presents an ultra-broadband and highly sensitive acoustic detector using polymer microring resonators. It has a flat frequency response stretching from DC up to 350 MHz at a -3 dB bandwidth. At the same time, the noise equivalent detectable pressure (NEP) is as low as 105 Pa in this broad bandwidth. Such an ultra-broad frequency response and unprecedented sensitivity make it an ideal detector in the high-resolution photoacoustic imaging. Application of such a broadband detector in photoacoustic imaging system leads to an improved axial resolving ability and sub-3 μm axial resolution is experimentally demonstrated without any sample treatment or signal processing, which is a two-fold improvement over the reported record. The device's miniaturized cavity height guarantees its superior broadband response, and at the same time, its high optical quality factor ensures the detection sensitivity. This study shows the polymer microring resonator is a promising

detector for applications in photoacoustic imaging with its ultra-broad bandwidth and high sensitivity.

Chapter 10

Ultrasound Detectors Based on Polymer Filled Silicon Metasurfaces on Fiber Tips

10.1 Introduction

In chapter 9, ultrasound detectors based on imprinted polymer microring resonators are discussed. Compared to conventional ultrasound transducers, the imprinted microrings have the advantages of high sensitivity, broad bandwidth, immunity to electromagnetic interferences, etc. These advantages have facilitated the device's various applications, such as photoacoustic imaging and real time THz pulse detection. However, the microring still need to be connected with optical fibers at its input and output waveguides, which limit the device footprint. In comparison, direct integrating acoustic detectors on fiber tips could enable various applications, especially intravascular photoacoustic/ultrasound imaging [229, 230], remote strain monitoring, and point-of-interest ultrasound inspection, where there is a very limited space for detectors. In this chapter, an acoustic detector based on polymer filled silicon metasurfaces on fiber tips will be discussed.

10.2 Design

The metasurface consists of one dimensional (1D) silicon gratings on a fused silica substrate, and the Si gratings are embedded in a SU8 polymer layer (figure 10.1a). The refractive index of Si (index around 3.5 at 1500 nm) is much higher than those of its surrounding media (index of fused silica is around 1.45 at 1500 nm, and index of SU8 is around 1.58 at 1500 nm), and therefore, such a structure is also termed "high contrast grating (HCG)". With different geometries of the Si gratings, the metasurface has rich optical characteristics, including high reflections, high transmissions, and sharp resonances [231]. In this work, a metasurface with a sharp resonance in reflection is utilized.

The designed metasurface has a period of 660 nm, grating width of 365 nm, and height of 1035 nm. For a normal incident light polarized along the Y axis (along the grating direction), the device demonstrates a sharp resonance in reflection around 1500 nm (Figure 10.1b). Such a resonance is formed by the interference inside the sub-wavelength silicon layer, which are related to the grating refractive index and dimensions, as well as the refractive index of its surrounding media, i.e., fused silica and SU8.

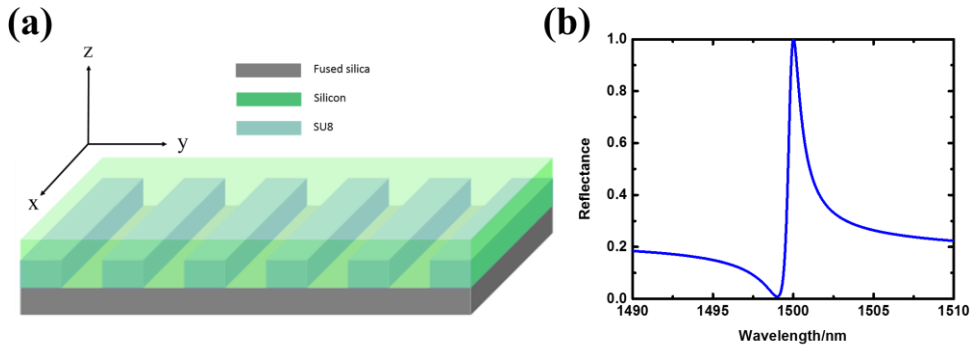

Figure 10.1: (a) Schematic drawing of the polymer filled silicon metasurface. (b) Reflection spectrum of the metasurface with a sharp resonance.

At the resonant wavelength, there is a significant amount of optical field inside the SU8 layer (figure 10.2a). As mentioned in chapter 9, an acoustic wave will modulate the refractive index of the SU8 polymer through the elastic-optic effect [232]. Since the resonant condition of the metasurface is closely correlated to the refractive indices of the Si grating's surrounding media, an acoustic wave will modulate the resonant wavelength of the device. For example, if the refractive index of SU8 changes from 1.58 to 1.585, the resonant wavelength has a shift of ~2 nm (figure 10.2b). If the wavelength of the probe laser is fixed at the slope of the resonant curve, there will be a time-varying output light intensity when an acoustic wave is incident onto the device. It is worth noting that there are advantages of designing the resonant wavelengths around 1500 nm, since there are various choices of light sources, detectors, and amplifiers at this telecommunication range.

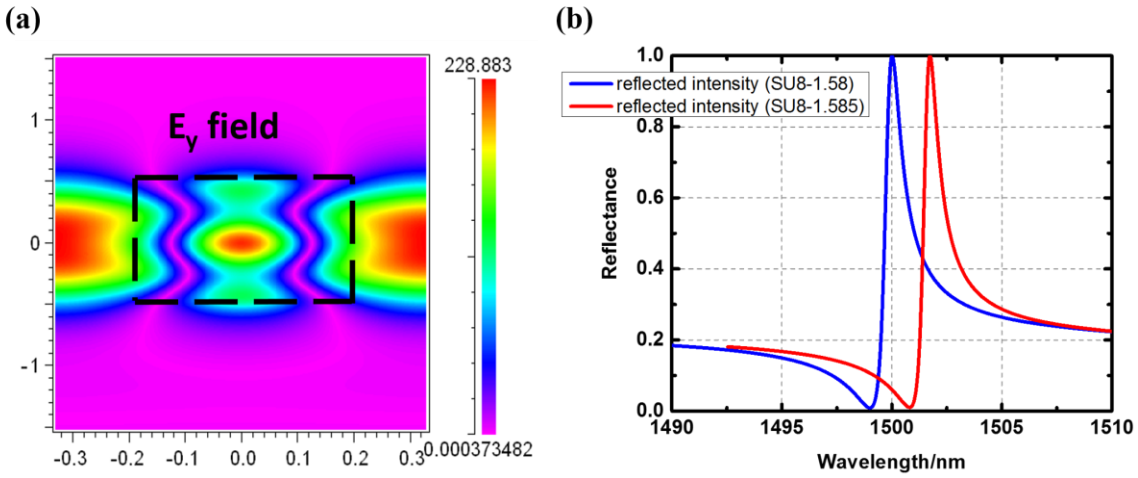

Figure 10.2: (a) Optical field distribution of a unit cell of the metasurface at resonance, and there is a significant optical field inside the SU8 polymer layer. The rectangular box denotes the position of the 1D Si grating. (b) Shift of the resonance wavelength with respect to the refractive index change of SU8.

The design tolerance is also investigated. Figure 10.3a shows the dependence of reflection resonance on the grating width for a fixed grating period (660 nm) and height (1035 nm). Increasing the grating width induces a red shift of the resonance; however, the shift is still within a reasonable range covered by many wavelength-tunable lasers (e.g., 8168F Hewlett Packard, TLB 6326 Newport, etc). Similarly, when the grating height is varied for a given width, the resonant wavelength is also maintained within a reasonable range (figure 10.3b).

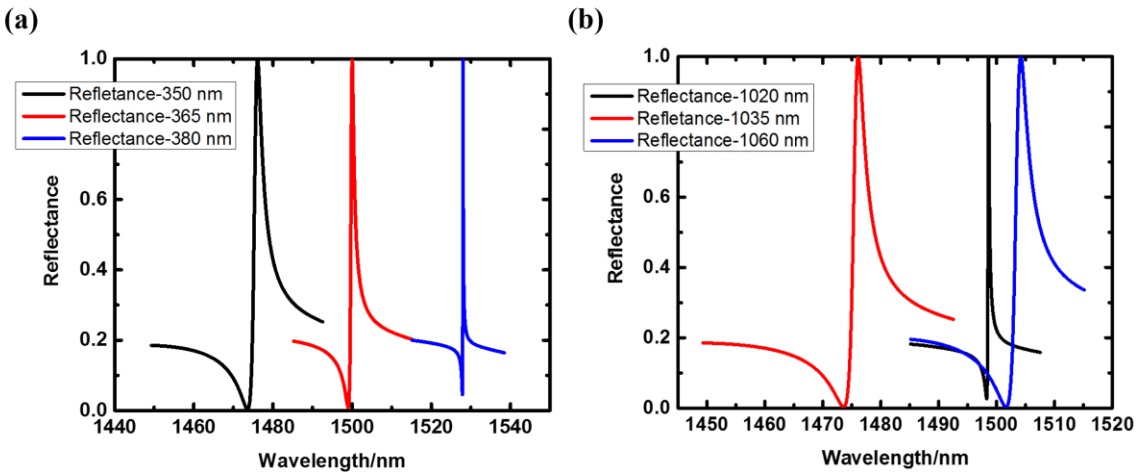

Figure 10.3: (a) Reflection resonances for gratings with different widths. The grating period and height are fixed as 660 nm and 1035 nm, respectively. (b) Reflection resonances for gratings with different heights. The grating period and width are fixed as 660 nm and 365 nm, respectively.

In addition, the metasurface is designed to be probed by an optical fiber and light has a diverging angle when exiting the fibers. For example, the numerical aperture (NA) of a single mode (SM) fiber at 1500 nm (SMF-28, Thorlabs) is 0.14. This leads to a diverging angle of ~ 8° when the light exits from the fiber into air. Figure 10.4 shows the reflection resonance for the probe light with different angles of incidence (5° and 10° in the XZ and YZ plane, respectively). The resonant wavelength varies with different angles of incidence, but is still around 1500 nm. The sensitivity of resonant wavelength to the angle of incidence will result in a decreased quality factor (Q factor) of the device measurement.

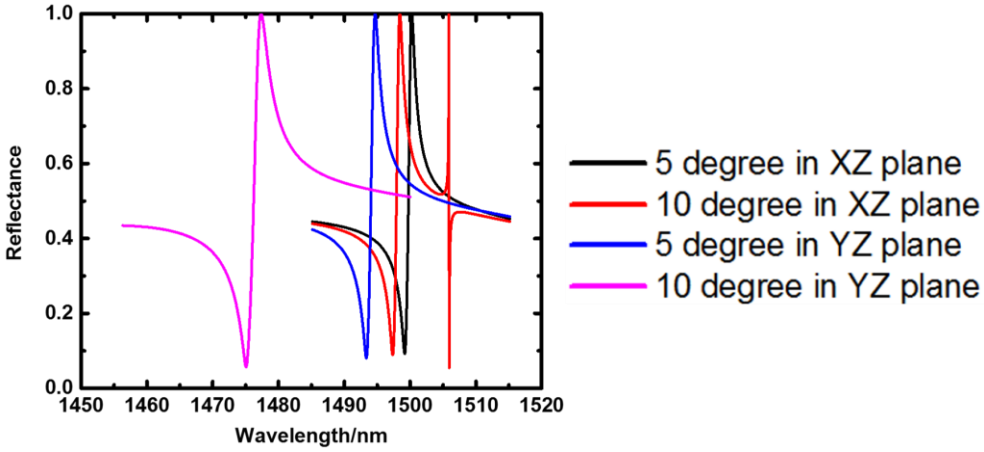

Figure 10.4: Reflection resonance with different angles of incidence. The polarization of the incident light is fixed along the 1D grating direction.

10.3 Fabrication

A novel process was developed to fabricate and transfer the metasurface structure onto fiber tips with preserved functionalities and performance. The metasuface fabrication starts with E-beam lithography and reactive ion etching (RIE) to define grating pattern on the top silicon layer of a silicon-on-insulator (SOI) wafer (Figure 10.5). Then the sample underwent a short-time thermal oxidation (1000 °C in air for 30 minutes), followed by buffered hydrofluoric acid (BHF) etching. This step will remove the native oxide grown during the thermal oxidation step, thus reducing the roughness of the Si grating and increasing the device's quality factor. Subsequently, SU-8 polymer is filled into the grating trenches by a thermal imprinting process followed by UV curing. Figure 10.6 shows the SEM picture of the HCG after BHF acid etching (a) and HCG after SU8 polymer filling (b). A microscope picture of the SU8 filled HCG is shown in figure 10.6c.

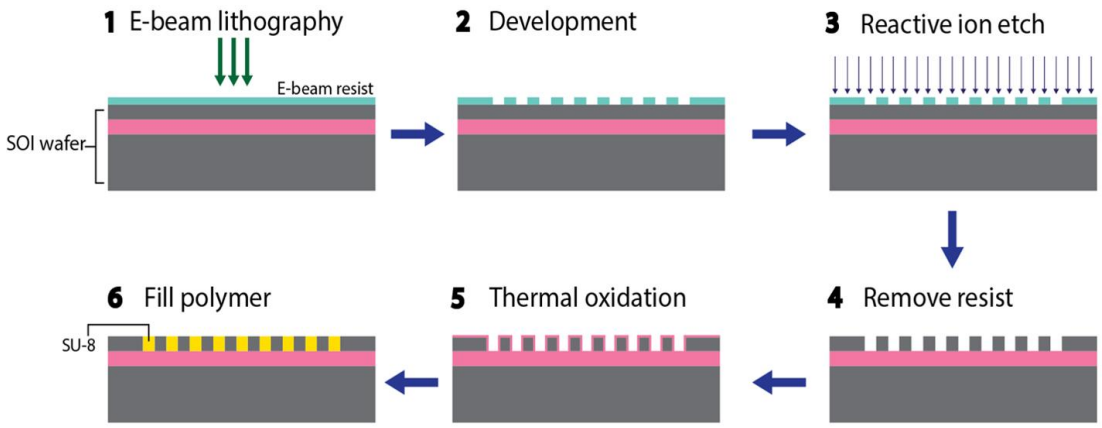

Figure 10.5: Fabrication process of the metasurface membrane.

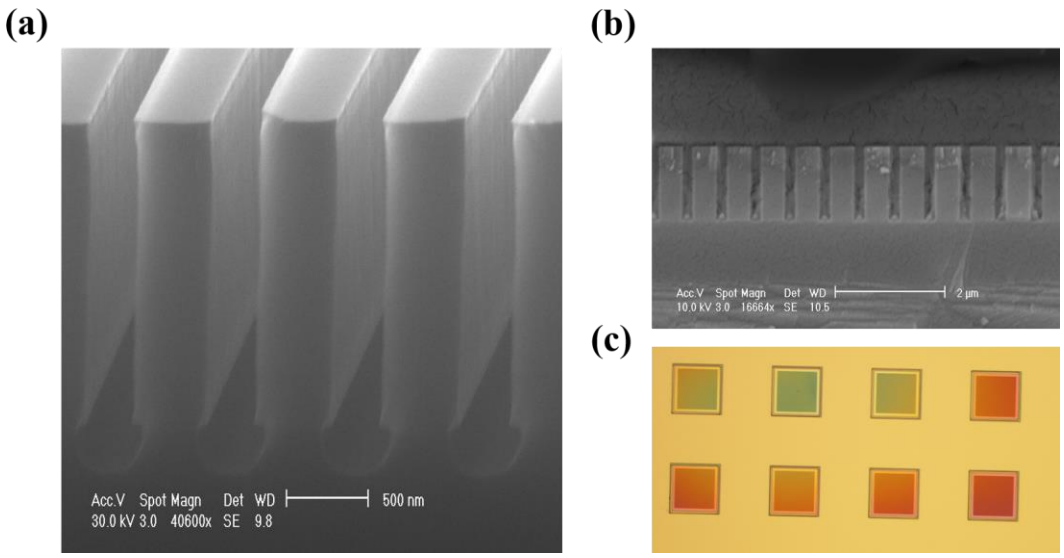

Figure 10.6: (a) SEM of the HCG after BHF etching. (b) SEM of the HCG after SU8 polymer filling. (c) Optical microscope picture of the SU8 filled HCG.

The HCG membrane is transferred onto a fiber tip with the help of a sacrificial release layer (figure 10.7). The sample is flipped over and boned to another fused silica substrate by a PMMA layer through a thermal imprinting process. Afterwards, the thick Si substrate was

removed by RIE. Finally, an optical fiber is mounted with the HCG membrane, and the fused silica substrate was released by dissolving the PMMA bonding layer in acetone. A microscope image of the final acoustic fiber probe is shown in Figure 10.8a.

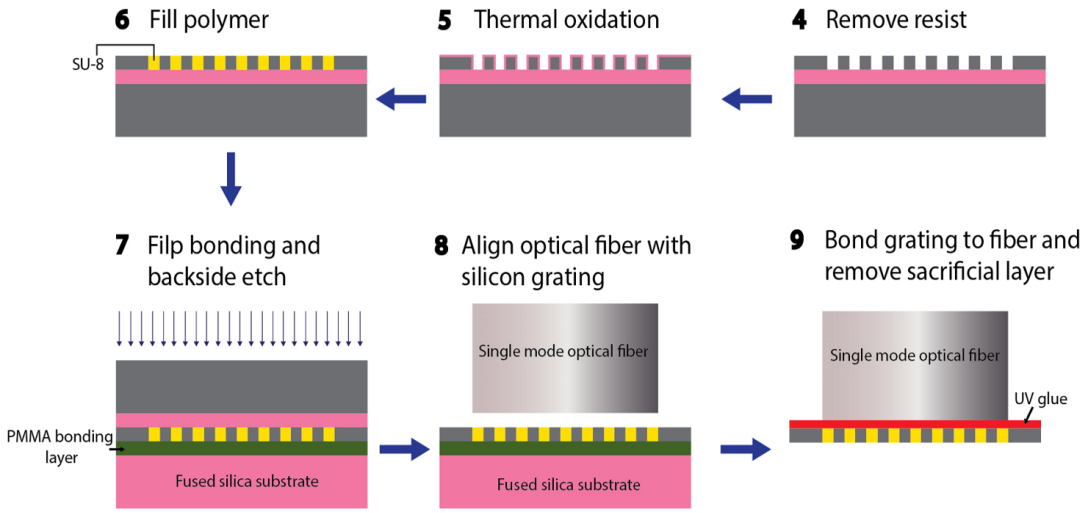

Figure 10.7: Fabrication process of transferring the metasurface membrane onto the tip of an optical fiber.

10.4 Preliminary test

The metasurface's reflection spectrum is characterized by a wavelength tunable laser around 1500 nm (8168F, Hewlett Packard) and the measured spectrum is plotted in Figure 10.8b. The optical Q-factor of the resonance is ~3000. The acoustic response of the probe is measured by using an ultrasound transducer as the acoustic source (figure 10.9).

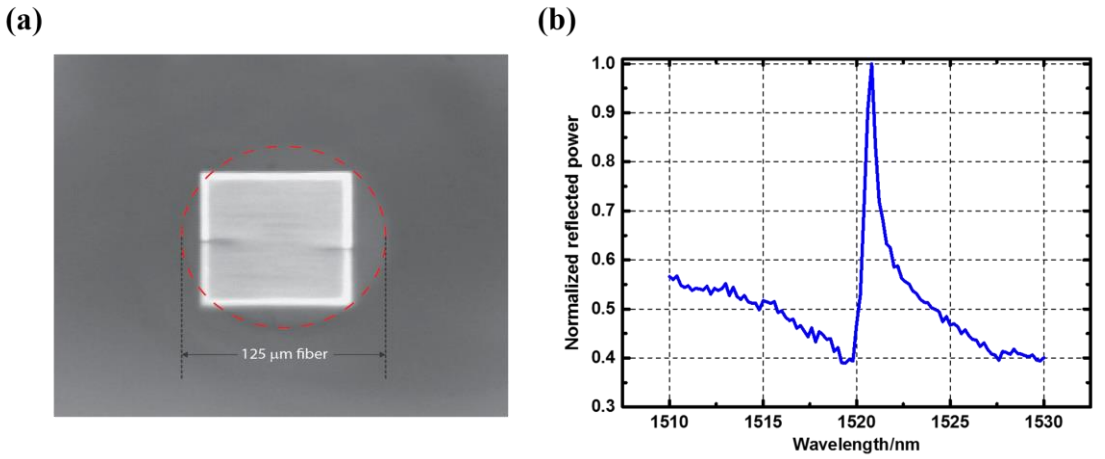

Figure 10.8: (a) An optical microscope picture of a metasurface membrane on the tip of an optical fiber. (b) Measured reflection spectrum of the device with a Q factor around 3000.

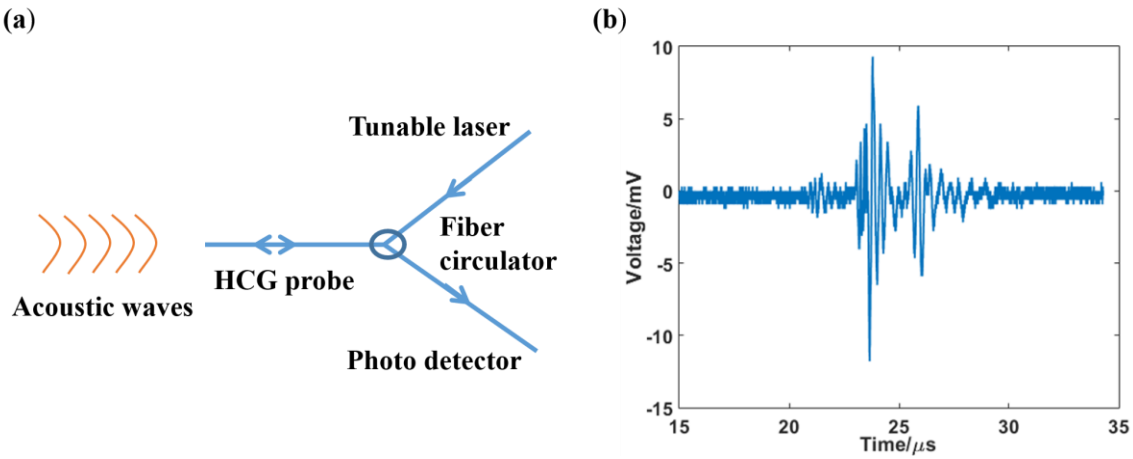

Figure 10.9: (a) Schematic of ultrasound wave detection using the metasurface probe. (b) Measured acoustic waves.

10.5 Conclusions

This chapter presents another kind of ultrasound detectors based on polymer filled metasurfaces on fiber tips. The polymer filled metasurfaces are designed to have sharp reflection resonances, which are prone to be modulated by external ultrasound waves. Direct integrating these devices on the tips of optical fibers further shrink their footprint, and provides viable solutions to applications, such as intravascular photoacoustic imaging, remote strain monitoring, and point-of-interest ultrasound inspection.

Chapter 11

Summary and Future Directions

11.1 Summary

The thesis is categorized into three parts: Doped Ag films and their optoelectronic applications; Metasurfaces for light property manipulations; Ultrasound detectors based on optical resonating structures. These parts are closely correlated with each other, and represent some of the recent developments in the constituent materials and device designs for future optical and optoelectronic device platforms.

In terms of the developments of new materials, a new kind of Ag film: doped Ag has been systematically studied. Compared to pure Ag films, doped Ag films are ultra-thin and smooth. They maintain the good optical and electrical properties of pure Ag films, while at the same time, have a significantly improved long-term and thermal stability, as well as a good adhesion to various substrates. Four kinds of doped Ag have been investigated: Al-doped Ag, Ti-doped Ag, Cr-doped Ag, and Cu-doped Ag. Various techniques have been utilize to characterize their optical and electrical properties, morphology, structural composition, as well as stability.

Thin doped Ag films have facilitated various optoelectronic devices, *i.e.*, organic solar cells and organic light emitting diodes. Organic solar cells using thin doped Ag films as transparent conductors have enhanced power conversion efficiencies (PCEs) thanks to the resonant light harvesting effect; Organic light emitting diodes with thin doped Ag films have enhanced out-coupling efficiencies and improved mechanical flexibilities. In addition, Al-doped Ag films enable a high-performance nanophotonic framework. Hyperbolic metamaterials consisting of doped Ag films have both a low-loss and homogeneous response; Plasmonic waveguides made of doped Ag films exhibit a record-high propagation distance.

In terms of the developments of device design and fabrication, nano-size metamaterials (metasurfaces) are demonstrated for controlling the polarization and propagation direction of light. A 290 nm thick metasurface, which provides asymmetric light transmission, is designed and fabricated. It has a measured transmission efficiency of 80%, an extinction ratio of 13.8 dB around 1.5 μm, and a full width half maximum bandwidth of 1.7 μm. Also, the metasurface has a good performance tolerance against the angle of incidence and constituent nano-structure geometry variations, and is compatible with large-scale manufacturing methods. In addition, a large-area, printed metasurface is designed and fabricated. It is made of lossless dielectric (silicon) materials and offers the functionality of converting a vertically polarized incident light into a radially polarized transmitted light. The design methodology and fabrication technique are applicable to various metasurfaces.

The optical and optoelectronic devices also provide valuable solutions to other problems, such as acoustic wave detection. It is shown that optical resonant structures provide a unique approach for detecting acoustic waves. Nanoimprinted polymer microring resonators are investigated as high-performance ultrasound detectors. They have a good detection sensitivity, broad response bandwidth, and immunity to electromagnetic interferences. These advantages have facilitated various applications of photoacoustic imaging and real-time terahertz (Thz) pulse detection. To further reduce the detector size, polymer filled silicon metasurfaces on fiber tips are also designed. The polymer filled metasurfaces are designed to have sharp reflection resonances, which are prone to be modulated by external ultrasound waves. Direct integrating these devices on the tips of optical fibers further shrink their footprint, and provides viable solutions to applications, such as intravascular photoacoustic imaging, remote strain monitoring, and point-of-interest ultrasound inspection.

11.2 Future directions

(1) Several alternative doped Ag films have been studied in chapter 2. Future work include charactering their thermal and long-term stabilities, applying the films in optical and optoelectronic devices, as well as testing other doping metals for ultra-thin Ag film deposition.

(2) A preliminary explanation of the mechanism of ultra-thin Al-doped Ag formation is provided in chapter 2. Future work include more fundamental “first-principle” studies of

the thin doped Ag formation. Also, such a study can be extended to investigate the mechanism of other alternative doped Ag films.

(3) The design for enhancing the out-coupling efficiencies of OLEDs is given in chapter 5. Future work include fabricating the designed OLEDs and characterizing their performance.

(4) An imprinted metasurface is presented in chapter 8. It can convert a vertically polarized incident light into a radially polarized light upon transmission. Future work include extending the device design methodologies and fabrication techniques to other metasurface structures, such as polarization rotation metasurfaces, “photonic spin-hall effect” metasurfaces, etc.

(5) Ultrasound detectors based on polymer filled metasurfaces on fiber tips are presented in chapter 10. Future work include characterizing the probe’s detection sensitivity, frequency response, angular detection sensitivity, etc. Also, such probes will be applied in the intravascular photoacoustic imaging, ultrasound inspection, etc.

11.3 Contributions

The work in this thesis has been published in the following journals and patents.

Doped Ag films

(1) New Nanophotonic Framework Enabled by Ultra-thin, Low-loss and Stable Al-doped Ag Films," *To be submitted, 2016*

(2) Ultra-thin Doped Noble Metal Films for Optoelectronics and Photonics Applications," *Pending (U.S. Patent Application No. 62/005,169), 2016*

(3) High-performance Ta_2O_5/Al-doped Ag Electrode for Resonant Light Harvesting in Efficient Organic Solar Cells, *Advanced Energy Materials, 5, 17, 2015*

(4) Ultra-thin, Smooth, and Low-loss Al-doped Ag Film and its Application as Transparent Electrode in Organic Photovoltaics, *Advanced Materials, 26, 5696, 2014*

(5) Ultra-smooth and Thermally-stable Ag-based Films with Sub-nanometer Roughness by Al Doping, *ACS Nano, 8, 10343, 2014*

Metamaterials and metasurfaces

(1) Breaking Malus' Law: Highly Efficient, Broadband, and Angular Robust Asymmetric Light Transmitting Metasurface, *Under revision, 2016*

Ultrasound detectors based on optical resonating structures

(1) Printed Photonic Elements: Nanoimprinting and Beyond, *Journal of Materials Chemistry C, In press, 2016*

(2) Imprinted Polymer Microrings as High Performance Ultrasound Detectors in Photoacoustic Imaging, *Journal of Lightwave Technology, 33, 20, 2015*

(3) Review of Imprinted Polymer Microring as Ultrasound Sensor: Design, Fabrication and Characterization, *IEEE Sensors Journal, 15,6, 2015*

(4) Ultra-broad Bandwidth Optical Ultrasound Transducer for Photoacoustic Imaging, *ACS Photonics, 1, 1093, 2014*

(5) New Method for THz Detection and Imaging, *Optics and Photonics News, 29, 45, 2014*

(6) Efficient Real-time Detection of Terahertz Pulse Radiation Based on Photoacoustic Conversion by Carbon Nanotube Nanocomposite, *Nature Photonics, 8,537, 2014*

Bibliography

[1] A. Poddubny, I. Iorsh, P. Belov, and Y. Kivshar, "Hyperbolic metamaterials," Nature Photonics, vol. 7, pp. 948-957, 2013.

[2] N. I. Zheludev, "The Road Ahead for Metamaterials," Science, vol. 328, pp. 582-583, 2010.

[3] C. M. Soukoulis and M. Wegener, "Optical Metamaterials—More Bulky and Less Lossy," Science, vol. 330, pp. 1633-1634, 2010.

[4] R. Maas, J. Parsons, N. Engheta, and A. Polman, "Experimental realization of an epsilon-near-zero metamaterial at visible wavelengths," Nature Photonics, vol. 7, pp. 907-912, 2013.

[5] H. N. S. Krishnamoorthy, Z. Jacob, E. Narimanov, I. Kretzschmar, and V. M. Menon, "Topological Transitions in Metamaterials," Science, vol. 336, pp. 205-209, 2012.

[6] N. P. Sergeant, A. Hadipour, B. Niesen, D. Cheyns, P. Heremans, P. Peumans, et al., "Design of Transparent Anodes for Resonant Cavity Enhanced Light Harvesting in Organic Solar Cells," Advanced Materials, vol. 24, pp. 728-732, 2012.

[7] H. Jin, C. Tao, M. Velusamy, M. Aljada, Y. Zhang, M. Hambsch, et al., "Efficient, Large Area ITO-and-PEDOT-free Organic Solar Cell Sub-modules," Advanced Materials, vol. 24, pp. 2572-2577, 2012.

[8] N. Fang, H. Lee, C. Sun, and X. Zhang, "Sub-Diffraction-Limited Optical Imaging with a Silver Superlens," Science, vol. 308, pp. 534-537, 2005.

[9] Z. Liu, S. Durant, H. Lee, Y. Pikus, N. Fang, Y. Xiong, et al., "Far-Field Optical Superlens," Nano Letters, vol. 7, pp. 403-408, 2007.

[10] T. Xu and H. J. Lezec, "Visible-frequency asymmetric transmission devices incorporating a hyperbolic metamaterial," Nature Communications, vol. 5, p. 4141, 2014.

[11] H. J. Lezec, J. A. Dionne, and H. A. Atwater, "Negative Refraction at Visible Frequencies," Science, vol. 316, pp. 430-432, 2007-04-20 00:00:00 2007.

[12] D. Lu, J. J. Kan, E. E. Fullerton, and Z. Liu, "Enhancing spontaneous emission rates of molecules using nanopatterned multilayer hyperbolic metamaterials," Nature Nanotechnology, vol. 9, pp. 48-53, 2014.

[13] Y.-K. R. Wu, A. E. Hollowell, C. Zhang, and L. J. Guo, "Angle-Insensitive Structural Colours based on Metallic Nanocavities and Coloured Pixels beyond the Diffraction Limit," Scientific Reports, vol. 3, p. 1194, 2013.

[14] B. Zeng, Y. Gao, and F. J. Bartoli, "Ultrathin Nanostructured Metals for Highly Transmissive Plasmonic Subtractive Color Filters," Scientific Reports, vol. 3, p. 2840, 2013.

[15] P. Chaturvedi, W. Wu, V. Logeeswaran, Z. Yu, M. S. Islam, S. Y. Wang, et al., "A smooth optical superlens," Applied Physics Letters, vol. 96, p. 043102, 2010.

[16] G. Subramania, A. J. Fischer, and T. S. Luk, "Optical properties of metal-dielectric based epsilon near zero metamaterials," Applied Physics Letters, vol. 101, p. 241107, 2012.

[17] R. Lazzari and J. Jupille, "Silver layers on oxide surfaces: morphology and optical properties," Surface Science, vol. 482–485, pp. 823-828, 2001.

[18] J. Gao, L. Sun, H. Deng, C. J. Mathai, S. Gangopadhyay, and X. Yang, "Experimental realization of epsilon-near-zero metamaterial slabs with metal-dielectric multilayers," Applied Physics Letters, vol. 103, p. 051111, 2013.

[19] V. J. Logeeswaran, N. P. Kobayashi, M. S. Islam, W. Wu, P. Chaturvedi, N. X. Fang, et al., "Ultrasmooth Silver Thin Films Deposited with a Germanium Nucleation Layer," Nano Letters, vol. 9, pp. 178-182, 2009.

[20] K. Thürmer, E. D. Williams, and J. E. Reutt-Robey, "Dewetting dynamics of ultrathin silver films on Si(111)," Physical Review B, vol. 68, p. 155423, 2003.

[21] H. Krishna, R. Sachan, J. Strader, C. Favazza, M. Khenner, and R. Kalyanaraman, "Thickness-dependent spontaneous dewetting morphology of ultrathin Ag films," Nanotechnology, vol. 21, p. 155601, 2010.

[22] H. C. Kim, T. L. Alford, and D. R. Allee, "Thickness dependence on the thermal stability of silver thin films," Applied Physics Letters, vol. 81, pp. 4287-4289, 2002.

[23] P. Nagpal, N. C. Lindquist, S.-H. Oh, and D. J. Norris, "Ultrasmooth Patterned Metals for Plasmonics and Metamaterials," Science, vol. 325, pp. 594-597, 2009.

[24] H. Liu, B. Wang, E. S. P. Leong, P. Yang, Y. Zong, G. Si, et al., "Enhanced Surface Plasmon Resonance on a Smooth Silver Film with a Seed Growth Layer," ACS Nano, vol. 4, pp. 3139-3146, 2010.

[25] X. Jiao, J. Goeckeritz, S. Blair, and M. Oldham, "Localization of Near-Field Resonances in Bowtie Antennae: Influence of Adhesion Layers," Plasmonics, vol. 4, pp. 37-50, 2009.

[26] T. Siegfried, Y. Ekinci, O. J. F. Martin, and H. Sigg, "Engineering Metal Adhesion Layers That Do Not Deteriorate Plasmon Resonances," ACS Nano, vol. 7, pp. 2751-2757, 2013.

[27] P. Wróbel, T. Stefaniuk, M. Trzcinski, A. A. Wronkowska, A. Wronkowski, and T. Szoplik, "Ge Wetting Layer Increases Ohmic Plasmon Losses in Ag Film Due to Segregation," ACS Applied Materials & Interfaces, vol. 7, pp. 8999-9005, 2015.

[28] V. J. Logeeswaran, M.-L. Chan, Y. Bayam, M. Saif Islam, D. A. Horsley, X. Li, et al., "Ultra-smooth metal surfaces generated by pressure-induced surface deformation of thin metal films," Applied Physics A, vol. 87, pp. 187-192, 2007.

[29] Y. Wu, C. Zhang, N. M. Estakhri, Y. Zhao, J. Kim, M. Zhang, et al., "Intrinsic Optical Properties and Enhanced Plasmonic Response of Epitaxial Silver," Advanced Materials, vol. 26, pp. 6106-6110, 2014.

[30] D.-T. Nguyen, S. Vedraine, L. Cattin, P. Torchio, M. Morsli, F. Flory, et al., "Effect of the thickness of the MoO3 layers on optical properties of MoO3/Ag/MoO3 multilayer structures," Journal of Applied Physics, vol. 112, p. 063505, 2012.

[31] J. N. Hilfiker, N. Singh, T. Tiwald, D. Convey, S. M. Smith, J. H. Baker, et al., "Survey of methods to characterize thin absorbing films with Spectroscopic Ellipsometry," Thin Solid Films, vol. 516, pp. 7979-7989, 2008.

[32] W. A. McGahan, B. Johs, and J. A. Woollam, "Techniques for ellipsometric measurement of the thickness and optical constants of thin absorbing films," Thin Solid Films, vol. 234, pp. 443-446, 1993.

[33] K.-P. Chen, V. P. Drachev, J. D. Borneman, A. V. Kildishev, and V. M. Shalaev, "Drude Relaxation Rate in Grained Gold Nanoantennas," Nano Letters, vol. 10, pp. 916-922, 2010.

[34] P. S. Harsha, "Principles of Vapor Deposition of Thin Films, 1st Edition," Elsevier Science, 2007

[35] R. P. Galhenage, H. Yan, S. A. Tenney, N. Park, G. Henkelman, P. Albrecht, et al., "Understanding the Nucleation and Growth of Metals on TiO2: Co Compared to Au, Ni, and Pt," The Journal of Physical Chemistry C, vol. 117, pp. 7191-7201, 2013.

[36] U. Diebold, J.-M. Pan, and T. E. Madey, "Ultrathin metal film growth on TiO_2(110): an overview," Surface Science, vol. 331–333, pp. 845-854, 1995.

[37] C. T. Campbell, "Ultrathin metal films and particles on oxide surfaces: structural, electronic and chemisorptive properties," Surface Science Reports, vol. 27, pp. 1-111, 1997.

[38] O. Inganas, "Organic photovoltaics: Avoiding indium," Nature Photonics, vol. 5, pp. 201-202, 2011.

[39] Y. Wang, S. W. Tong, X. F. Xu, B. Özyilmaz, and K. P. Loh, "Interface Engineering of Layer-by-Layer Stacked Graphene Anodes for High-Performance Organic Solar Cells," Advanced Materials, vol. 23, pp. 1514-1518, 2011.

[40] Z. Liu, J. Li, and F. Yan, "Package-Free Flexible Organic Solar Cells with Graphene top Electrodes," Advanced Materials, vol. 25, pp. 4296-4301, 2013.

[41] L. Gomez De Arco, Y. Zhang, C. W. Schlenker, K. Ryu, M. E. Thompson, and C. Zhou, "Continuous, Highly Flexible, and Transparent Graphene Films by Chemical Vapor Deposition for Organic Photovoltaics," ACS Nano, vol. 4, pp. 2865-2873, 2010.

[42] D. Liu, M. Zhao, Y. Li, Z. Bian, L. Zhang, Y. Shang, et al., "Solid-State, Polymer-Based Fiber Solar Cells with Carbon Nanotube Electrodes," ACS Nano, vol. 6, pp. 11027-11034, 2012.

[43] Y. Xia, K. Sun, and J. Ouyang, "Solution-Processed Metallic Conducting Polymer Films as Transparent Electrode of Optoelectronic Devices," Advanced Materials, vol. 24, pp. 2436-2440, 2012.

[44] D. Gupta, M. M. Wienk, and R. A. J. Janssen, "Efficient Polymer Solar Cells on Opaque Substrates with a Laminated PEDOT:PSS Top Electrode," Advanced Energy Materials, vol. 3, pp. 782-787, 2013.

[45] W. Zhang, B. Zhao, Z. He, X. Zhao, H. Wang, S. Yang, et al., "High-efficiency ITO-free polymer solar cells using highly conductive PEDOT:PSS/surfactant bilayer transparent anodes," Energy & Environmental Science, vol. 6, pp. 1956-1964, 2013.

[46] M.-G. Kang, H. Joon Park, S. Hyun Ahn, and L. Jay Guo, "Transparent Cu nanowire mesh electrode on flexible substrates fabricated by transfer printing and its application in organic solar cells," Solar Energy Materials and Solar Cells, vol. 94, pp. 1179-1184, 2010.

[47] M.-G. Kang, T. Xu, H. J. Park, X. Luo, and L. J. Guo, "Efficiency Enhancement of Organic Solar Cells Using Transparent Plasmonic Ag Nanowire Electrodes," Advanced Materials, vol. 22, pp. 4378-4383, 2010.

[48] H. Wu, L. Hu, M. W. Rowell, D. Kong, J. J. Cha, J. R. McDonough, et al., "Electrospun Metal Nanofiber Webs as High-Performance Transparent Electrode," Nano Letters, vol. 10, pp. 4242-4248, 2010.

[49] H. Wu, D. Kong, Z. Ruan, P.-C. Hsu, S. Wang, Z. Yu, et al., "A transparent electrode based on a metal nanotrough network," Nature Nanotechnology, vol. 8, pp. 421-425, 2013.

[50] P.-C. Hsu, S. Wang, H. Wu, V. K. Narasimhan, D. Kong, H. Ryoung Lee, et al., "Performance enhancement of metal nanowire transparent conducting electrodes by mesoscale metal wires," Nature Communications, vol. 4, p. 2522, 2013.

[51] J.-Y. Lee, S. T. Connor, Y. Cui, and P. Peumans, "Solution-Processed Metal Nanowire Mesh Transparent Electrodes," Nano Letters, vol. 8, pp. 689-692, 2008.

[52] F. S. F. Morgenstern, D. Kabra, S. Massip, T. J. K. Brenner, P. E. Lyons, J. N. Coleman, et al., "Ag-nanowire films coated with ZnO nanoparticles as a transparent electrode for solar cells," Applied Physics Letters, vol. 99, p. 183307, 2011.

[53] C.-C. Chen, L. Dou, R. Zhu, C.-H. Chung, T.-B. Song, Y. B. Zheng, et al., "Visibly Transparent Polymer Solar Cells Produced by Solution Processing," ACS Nano, vol. 6, pp. 7185-7190, 2012.

[54] M. Reinhard, R. Eckstein, A. Slobodskyy, U. Lemmer, and A. Colsmann, "Solution-processed polymer–silver nanowire top electrodes for inverted semi-transparent solar cells," Organic Electronics, vol. 14, pp. 273-277, 2013.

[55] D. S. Hecht, L. Hu, and G. Irvin, "Emerging Transparent Electrodes Based on Thin Films of Carbon Nanotubes, Graphene, and Metallic Nanostructures," Advanced Materials, vol. 23, pp. 1482-1513, 2011.

[56] M. G. Kang and L. J. Guo, "Nanoimprinted Semitransparent Metal Electrodes and Their Application in Organic Light-Emitting Diodes," Advanced Materials, vol. 19, pp. 1391-1396, 2007.

[57] M.-G. Kang, M.-S. Kim, J. Kim, and L. J. Guo, "Organic Solar Cells Using Nanoimprinted Transparent Metal Electrodes," Advanced Materials, vol. 20, pp. 4408-4413, 2008.

[58] A. Colsmann, A. Puetz, A. Bauer, J. Hanisch, E. Ahlswede, and U. Lemmer, "Efficient Semi-Transparent Organic Solar Cells with Good Transparency Color Perception and Rendering Properties," Advanced Energy Materials, vol. 1, pp. 599-603, 2011.

[59] K.-S. Chen, J.-F. Salinas, H.-L. Yip, L. Huo, J. Hou, and A. K. Y. Jen, "Semi-transparent polymer solar cells with 6% PCE, 25% average visible transmittance and a color rendering index close to 100 for power generating window applications," Energy & Environmental Science, vol. 5, pp. 9551-9557, 2012.

[60] J. You, C.-C. Chen, Z. Hong, K. Yoshimura, K. Ohya, R. Xu, et al., "10.2% Power Conversion Efficiency Polymer Tandem Solar Cells Consisting of Two Identical Sub-Cells," Advanced Materials, vol. 25, pp. 3973-3978, 2013.

[61] D. W. Zhao, X. W. Sun, C. Y. Jiang, A. K. K. Kyaw, G. Q. Lo, and D. L. Kwong, "Efficient tandem organic solar cells with an Al/MoO3 intermediate layer," Applied Physics Letters, vol. 93, p. 083305, 2008.

[62] N. Wang, J. D. Zimmerman, X. Tong, X. Xiao, J. Yu, and S. R. Forrest, "Snow cleaning of substrates increases yield of large-area organic photovoltaics," Applied Physics Letters, vol. 101, p. 133901, 2012.

[63] C. J. Brabec, V. Dyakonov, J. Parisi, and N. S. Sariciftci, "Organic Photovoltaics," Springer-Verlag Berlin Heidelberg, 2003.

[64] S. Bae, H. Kim, Y. Lee, X. Xu, J.-S. Park, Y. Zheng, et al., "Roll-to-roll production of 30-inch graphene films for transparent electrodes," Nature Nanotechnology, vol. 5, pp. 574-578, 2010.

[65] J. Yun, W. Wang, T. S. Bae, Y. H. Park, Y.-C. Kang, D.-H. Kim, et al., "Preparation of Flexible Organic Solar Cells with Highly Conductive and Transparent Metal-Oxide Multilayer Electrodes Based on Silver Oxide," ACS Applied Materials & Interfaces, vol. 5, pp. 9933-9941, 2013.

[66] D. S. Ghosh, L. Martinez, S. Giurgola, P. Vergani, and V. Pruneri, "Widely transparent electrodes based on ultrathin metals," Optics Letters, vol. 34, pp. 325-327, 2009.

[67] D.-S. Leem, A. Edwards, M. Faist, J. Nelson, D. D. C. Bradley, and J. C. de Mello, "Efficient Organic Solar Cells with Solution-Processed Silver Nanowire Electrodes," Advanced Materials, vol. 23, pp. 4371-4375, 2011.

[68] A. Kim, Y. Won, K. Woo, C.-H. Kim, and J. Moon, "Highly Transparent Low Resistance ZnO/Ag Nanowire/ZnO Composite Electrode for Thin Film Solar Cells," ACS Nano, vol. 7, pp. 1081-1091, 2013.

[69] C.-C. Chueh, S.-C. Chien, H.-L. Yip, J. F. Salinas, C.-Z. Li, K.-S. Chen, et al., "Toward High-Performance Semi-Transparent Polymer Solar Cells: Optimization of Ultra-Thin Light Absorbing Layer and Transparent Cathode Architecture," Advanced Energy Materials, vol. 3, pp. 417-423, 2013.

[70] B. O'Connor, C. Haughn, K.-H. An, K. P. Pipe, and M. Shtein, "Transparent and conductive electrodes based on unpatterned, thin metal films," Applied Physics Letters, vol. 93, p. 223304, 2008.

[71] E. H. E. Wu, L. Sheng-Han, C. Chieh-Wei, L. Gang, X. Zheng, and Y. Yang, "Controlling optical properties of electrodes with stacked metallic thin films for polymeric light-emitting diodes and displays," Journal of Display Technology, vol. 1, pp. 105-111, 2005.

[72] S. Auer, W. Wan, X. Huang, A. G. Ramirez, and H. Cao, "Morphology-induced plasmonic resonances in silver-aluminum alloy thin films," Applied Physics Letters, vol. 99, p. 041116, 2011.

[73] C. C. Wu, C. I. Wu, J. C. Sturm, and A. Kahn, "Surface modification of indium tin oxide by plasma treatment: An effective method to improve the efficiency, brightness, and reliability of organic light emitting devices," Applied Physics Letters, vol. 70, pp. 1348-1350, 1997.

[74] A. K. K. Kyaw, X. W. Sun, C. Y. Jiang, G. Q. Lo, D. W. Zhao, and D. L. Kwong, "An inverted organic solar cell employing a sol-gel derived ZnO electron selective layer and thermal evaporated MoO3 hole selective layer," Applied Physics Letters, vol. 93, p. 221107, 2008.

[75] V. Shrotriya, G. Li, Y. Yao, C.-W. Chu, and Y. Yang, "Transition metal oxides as the buffer layer for polymer photovoltaic cells," Applied Physics Letters, vol. 88, p. 073508, 2006.

[76] K. M. Coakley and M. D. McGehee, "Conjugated Polymer Photovoltaic Cells," Chemistry of Materials, vol. 16, pp. 4533-4542, 2004.

[77] P. Yeh, "Optical Waves in Layered Media.," John Wiley & Sons, 2005.

[78] J.-F. Salinas, H.-L. Yip, C.-C. Chueh, C.-Z. Li, J.-L. Maldonado, and A. K. Y. Jen, "Optical Design of Transparent Thin Metal Electrodes to Enhance In-Coupling and Trapping of Light in Flexible Polymer Solar Cells," Advanced Materials, vol. 24, pp. 6362-6367, 2012.

[79] M. A. Green and S. Pillai, "Harnessing plasmonics for solar cells," Nat Photon, vol. 6, pp. 130-132, 2012.

[80] X. Li, W. C. H. Choy, L. Huo, F. Xie, W. E. I. Sha, B. Ding, et al., "Dual Plasmonic Nanostructures for High Performance Inverted Organic Solar Cells," Advanced Materials, vol. 24, pp. 3046-3052, 2012.

[81] L. Müller-Meskamp, Y. H. Kim, T. Roch, S. Hofmann, R. Scholz, S. Eckardt, et al., "Efficiency Enhancement of Organic Solar Cells by Fabricating Periodic Surface Textures using Direct Laser Interference Patterning," Advanced Materials, vol. 24, pp. 906-910, 2012.

[82] B. Niesen, B. P. Rand, P. Van Dorpe, D. Cheyns, L. Tong, A. Dmitriev, et al., "Plasmonic Efficiency Enhancement of High Performance Organic Solar Cells with a Nanostructured Rear Electrode," Advanced Energy Materials, vol. 3, pp. 145-150, 2013.

[83] T. Schwab, S. Schubert, L. Müller-Meskamp, K. Leo, and M. C. Gather, "Eliminating Micro-Cavity Effects in White Top-Emitting OLEDs by Ultra-Thin Metallic Top Electrodes," Advanced Optical Materials, vol. 1, pp. 921-925, 2013.

[84] C. Zhang, D. Zhao, D. Gu, H. Kim, T. Ling, Y.-K. R. Wu, et al., "An Ultrathin, Smooth, and Low-Loss Al-Doped Ag Film and Its Application as a Transparent Electrode in Organic Photovoltaics," Advanced Materials, vol. 26, pp. 5696-5701, 2014.

[85] L.-H. Xu, Q.-D. Ou, Y.-Q. Li, Y.-B. Zhang, X.-D. Zhao, H.-Y. Xiang, et al., "Microcavity-Free Broadband Light Outcoupling Enhancement in Flexible Organic Light-Emitting Diodes with Nanostructured Transparent Metal–Dielectric Composite Electrodes," ACS Nano, vol. 10, pp. 1625-1632, 2016.

[86] Z. B. Wang, M. G. Helander, QiuJ, D. P. Puzzo, M. T. Greiner, Z. M. Hudson, et al., "Unlocking the full potential of organic light-emitting diodes on flexible plastic," Nature Photonics, vol. 5, pp. 753-757, 2011.

[87] W. Gaynor, S. Hofmann, M. G. Christoforo, C. Sachse, S. Mehra, A. Salleo, et al., "Color in the Corners: ITO-Free White OLEDs with Angular Color Stability," Advanced Materials, vol. 25, pp. 4006-4013, 2013.

[88] Y. Qu, M. Slootsky, and S. R. Forrest, "Enhanced light extraction from organic light-emitting devices using a sub-anode grid," Nature Photonics, vol. 9, pp. 758-763, 2015.

[89] M. Jiao, C.-Y. Lu, W.-K. Lee, C.-Y. Chen, and C.-C. Wu, "Simple Planar Indium-Tin-Oxide-Free Organic Light-Emitting Devices with Nearly 39% External Quantum Efficiency," Advanced Optical Materials, vol. 4, pp. 365-370, 2016.

[90] J. Ouyang, C. W. Chu, F. C. Chen, Q. Xu, and Y. Yang, "High-Conductivity Poly(3,4-ethylenedioxythiophene):Poly(styrene sulfonate) Film and Its Application in Polymer Optoelectronic Devices," Advanced Functional Materials, vol. 15, pp. 203-208, 2005.

[91] J. O. Hwang, J. S. Park, D. S. Choi, J. Y. Kim, S. H. Lee, K. E. Lee, et al., "Workfunction-Tunable, N-Doped Reduced Graphene Transparent Electrodes for High-Performance Polymer Light-Emitting Diodes," ACS Nano, vol. 6, pp. 159-167, 2012.

[92] L. Li, J. Liang, S.-Y. Chou, X. Zhu, X. Niu, ZhibinYu, et al., "A Solution Processed Flexible Nanocomposite Electrode with Efficient Light Extraction for Organic Light Emitting Diodes," Scientific Reports, vol. 4, p. 4307, 2014.

[93] K. Celebi, T. D. Heidel, and M. A. Baldo, "Simplified calculation of dipole energy transport in a multilayer stack using dyadic Green's functions," Optics Express, vol. 15, pp. 1762-1772, 2007.

[94] S. A. Maier, "Plasmonics: Fundamentals and Applications," Springer-Verlag, 2007.

[95] W. Cai, Shalaev, Vladimir, "Optical Metamaterials: Fundamentals and Applications," Springer-Verlag, 2010.

[96] J. Valentine, S. Zhang, T. Zentgraf, E. Ulin-Avila, D. A. Genov, G. Bartal, et al., "Three-dimensional optical metamaterial with a negative refractive index," Nature, vol. 455, pp. 376-379, 2008.

[97] V. M. Shalaev, "Optical negative-index metamaterials," Nature Photonics, vol. 1, pp. 41-48, 01//print 2007.

[98] C. Pfeiffer, C. Zhang, V. Ray, L. J. Guo, and A. Grbic, "High Performance Bianisotropic Metasurfaces: Asymmetric Transmission of Light," Physical Review Letters, vol. 113, p. 023902, 2014.

[99] N. Yu, P. Genevet, M. A. Kats, F. Aieta, J.-P. Tetienne, F. Capasso, et al., "Light Propagation with Phase Discontinuities: Generalized Laws of Reflection and Refraction," Science, vol. 334, pp. 333-337, 2011.

[100] T. Xu, Y.-K. Wu, X. Luo, and L. J. Guo, "Plasmonic nanoresonators for high-resolution colour filtering and spectral imaging," Nature Communications, vol. 1, p. 59, 2010.

[101] X. Ni, Z. J. Wong, M. Mrejen, Y. Wang, and X. Zhang, "An ultrathin invisibility skin cloak for visible light," Science, vol. 349, pp. 1310-1314, 2015.

[102] J. B. Pendry, D. Schurig, and D. R. Smith, "Controlling Electromagnetic Fields," Science, vol. 312, pp. 1780-1782, 2006.

[103] P. R. West, S. Ishii, G. V. Naik, N. K. Emani, V. M. Shalaev, and A. Boltasseva, "Searching for better plasmonic materials," Laser & Photonics Reviews, vol. 4, pp. 795-808, 2010.

[104] J. Zhou, A. F. Kaplan, L. Chen, and L. J. Guo, "Experiment and Theory of the Broadband Absorption by a Tapered Hyperbolic Metamaterial Array," ACS Photonics, vol. 1, pp. 618-624, 2014.

[105] C. Guclu, S. Campione, and F. Capolino, "Hyperbolic metamaterial as super absorber for scattered fields generated at its surface," Physical Review B, vol. 86, p. 205130, 2012.

[106] Y. Guo, C. L. Cortes, S. Molesky, and Z. Jacob, "Broadband super-Planckian thermal emission from hyperbolic metamaterials," Applied Physics Letters, vol. 101, p. 131106, 2012.

[107] L. Gu, T. U. Tumkur, G. Zhu, and M. A. Noginov, "Blue shift of spontaneous emission in hyperbolic metamaterial," Scientific Reports, vol. 4, p. 4969, 2014.

[108] G.W.Ford and W. H. Weber, "Electromagnetic interactions of molecules with metal surfaces," Physics Reports, vol. 113, pp. 195-287, 1984.

[109] W. L. Barnes, "Fluorescence near interfaces: the role of photonic mode density.," Journal of Modern Optics, vol. 45, pp. 661-699, 1998.

[110] P. Berini, "Long-range surface plasmon polaritons," Advances in Optics and Photonics, vol. 1, pp. 484-588, 2009.

[111] N. Kinsey, M. Ferrera, V. M. Shalaev, and A. Boltasseva, "Examining nanophotonics for integrated hybrid systems: a review of plasmonic interconnects

and modulators using traditional and alternative materials," Journal of the Optical Society of America B, vol. 32, pp. 121-142, 2015.

[112] S. Park and S. H. Song, "Polymeric variable optical attenuator based on long range surface plasmon polaritons," Electronics Letters, vol. 42, pp. 402-404, 2006.

[113] T. Nikolajsen, K. Leosson, and S. I. Bozhevolnyi, "Surface plasmon polariton based modulators and switches operating at telecom wavelengths," Applied Physics Letters, vol. 85, pp. 5833-5835, 2004.

[114] A. Boltasseva and S. I. Bozhevolnyi, "Directional Couplers Using Long-Range Surface Plasmon Polariton Waveguides," IEEE Journal of Selected Topics in Quantum Electronics, vol. 12, pp. 1233-1241, 2006.

[115] O. Krupin, H. Asiri, C. Wang, R. N. Tait, and P. Berini, "Biosensing using straight long-range surface plasmon waveguides," Optics Express, vol. 21, pp. 698-709, 2013.

[116] N. Kinsey, M. Ferrera, G. V. Naik, V. E. Babicheva, V. M. Shalaev, and A. Boltasseva, "Experimental demonstration of titanium nitride plasmonic interconnects," Optics Express, vol. 22, pp. 12238-12247, 2014.

[117] A. Boltasseva, T. Nikolajsen, K. Leosson, K. Kjaer, M. S. Larsen, and S. I. Bozhevolnyi, "Integrated optical components utilizing long-range surface plasmon polaritons," Lightwave Technology, Journal of, vol. 23, pp. 413-422, 2005.

[118] T. Nikolajsen, K. Leosson, I. Salakhutdinov, and S. I. Bozhevolnyi, "Polymer-based surface-plasmon-polariton stripe waveguides at telecommunication wavelengths," Applied Physics Letters, vol. 82, pp. 668-670, 2003.

[119] J. Jiang, C. L. Callender, S. Jacob, J. P. Noad, S. Chen, J. Ballato, et al., "Long-range surface plasmon polariton waveguides embedded in fluorinated polymer," Applied Optics, vol. 47, pp. 3892-3900, 2008.

[120] P. Berini, R. Charbonneau, N. Lahoud, and G. Mattiussi, "Characterization of long-range surface-plasmon-polariton waveguides," Journal of Applied Physics, vol. 98, p. 043109, 2005.

[121] J. Y. Chin, T. Steinle, T. Wehlus, D. Dregely, T. Weiss, V. I. Belotelov, et al., "Nonreciprocal plasmonics enables giant enhancement of thin-film Faraday rotation," Nature Communications, vol. 4, p. 1599, 2013.

[122] J. L. O'Brien, G. J. Pryde, A. G. White, T. C. Ralph, and D. Branning, "Demonstration of an all-optical quantum controlled-NOT gate," Nature, vol. 426, pp. 264-267, 2003.

[123] E. Knill, R. Laflamme, and G. J. Milburn, "A scheme for efficient quantum computation with linear optics," Nature, vol. 409, pp. 46-52, 2001.

[124] R. Fleury, D. L. Sounas, C. F. Sieck, M. R. Haberman, and A. Alù, "Sound Isolation and Giant Linear Nonreciprocity in a Compact Acoustic Circulator," Science, vol. 343, pp. 516-519, 2014.

[125] R. Singh, E. Plum, C. Menzel, C. Rockstuhl, A. K. Azad, R. A. Cheville, et al., "Terahertz metamaterial with asymmetric transmission," Physical Review B, vol. 80, p. 153104, 2009.

[126] S. Cakmakyapan, A. E. Serebryannikov, H. Caglayan, and E. Ozbay, "Spoof-plasmon relevant one-way collimation and multiplexing at beaming from a slit in metallic grating," Optics Express, vol. 20, pp. 26636-26648, 2012.

[127] C. Menzel, C. Helgert, C. Rockstuhl, E. B. Kley, A. Tünnermann, T. Pertsch, et al., "Asymmetric Transmission of Linearly Polarized Light at Optical Metamaterials," Physical Review Letters, vol. 104, p. 253902, 2010.

[128] V. A. Fedotov, A. S. Schwanecke, N. I. Zheludev, V. V. Khardikov, and S. L. Prosvirnin, "Asymmetric Transmission of Light and Enantiomerically Sensitive Plasmon Resonance in Planar Chiral Nanostructures," Nano Letters, vol. 7, pp. 1996-1999, 2007.

[129] D. Jalas, A. Petrov, M. Eich, W. Freude, S. Fan, Z. Yu, et al., "What is [mdash] and what is not [mdash] an optical isolator," Nature Photonics, vol. 7, pp. 579-582, 2013.

[130] L. Bi, J. Hu, P. Jiang, D. H. Kim, G. F. Dionne, L. C. Kimerling, et al., "On-chip optical isolation in monolithically integrated non-reciprocal optical resonators," Nature Photonics, vol. 5, pp. 758-762, 2011.

[131] A. Cicek, M. B. Yucel, O. A. Kaya, and B. Ulug, "Refraction-based photonic crystal diode," Optics Letters, vol. 37, pp. 2937-2939, 2012.

[132] C. Wang, X.-L. Zhong, and Z.-Y. Li, "Linear and passive silicon optical isolator," Scientific Reports, vol. 2, 2012.

[133] J. K. Gansel, M. Thiel, M. S. Rill, M. Decker, K. Bade, V. Saile, et al., "Gold Helix Photonic Metamaterial as Broadband Circular Polarizer," Science, vol. 325, pp. 1513-1515, 2009.

[134] S. Cakmakyapan, H. Caglayan, A. E. Serebryannikov, and E. Ozbay, "Experimental validation of strong directional selectivity in nonsymmetric metallic gratings with a subwavelength slit," Applied Physics Letters, vol. 98, p. 051103, 2011.

[135] S. Cakmakyapan, A. E. Serebryannikov, H. Caglayan, and E. Ozbay, "One-way transmission through the subwavelength slit in nonsymmetric metallic gratings," Optics Letters, vol. 35, pp. 2597-2599, 2010.

[136] Z. H. Zhu, K. Liu, W. Xu, Z. Luo, C. C. Guo, B. Yang, et al., "One-way transmission of linearly polarized light in plasmonic subwavelength metallic grating cascaded with dielectric grating," Optics Letters, vol. 37, pp. 4008-4010, 2012.

[137] A. E. Minovich, A. E. Miroshnichenko, A. Y. Bykov, T. V. Murzina, D. N. Neshev, and Y. S. Kivshar, "Functional and nonlinear optical metasurfaces," Laser & Photonics Reviews, vol. 9, pp. 195-213, 2015.

[138] N. Yu and F. Capasso, "Flat optics with designer metasurfaces," Nature Materials, vol. 13, pp. 139-150, 2014.

[139] Y. Nanfang, P. Genevet, F. Aieta, M. A. Kats, R. Blanchard, G. Aoust, et al., "Flat Optics: Controlling Wavefronts With Optical Antenna Metasurfaces," Selected Topics in Quantum Electronics, IEEE Journal of, vol. 19, p. 4700423, 2013.

[140] A. V. Kildishev, A. Boltasseva, and V. M. Shalaev, "Planar Photonics with Metasurfaces," Science, vol. 339, p. 6125, 2013.

[141] C. Pfeiffer and A. Grbic, "Metamaterial Huygens' Surfaces: Tailoring Wave Fronts with Reflectionless Sheets," Physical Review Letters, vol. 110, p. 197401, 2013.

[142] A. Shaltout, J. Liu, V. M. Shalaev, and A. V. Kildishev, "Optically Active Metasurface with Non-Chiral Plasmonic Nanoantennas," Nano Letters, vol. 14, pp. 4426-4431, 2014.

[143] Y. Yang, W. Wang, P. Moitra, I. I. Kravchenko, D. P. Briggs, and J. Valentine, "Dielectric Meta-Reflectarray for Broadband Linear Polarization Conversion and Optical Vortex Generation," Nano Letters, vol. 14, pp. 1394-1399, 2014.

[144] N. K. Grady, J. E. Heyes, D. R. Chowdhury, Y. Zeng, M. T. Reiten, A. K. Azad, et al., "Terahertz Metamaterials for Linear Polarization Conversion and Anomalous Refraction," Science, vol. 340, pp. 1304-1307, 2013.

[145] C. Pfeiffer and A. Grbic, "Bianisotropic Metasurfaces for Optimal Polarization Control: Analysis and Synthesis," Physical Review Applied, vol. 2, p. 044011, 2014.

[146] C. Pfeiffer, C. Zhang, V. Ray, L. Jay Guo, and A. Grbic, "Polarization rotation with ultra-thin bianisotropic metasurfaces," Optica, vol. 3, pp. 427-432, 2016.

[147] D. Lin, P. Fan, E. Hasman, and M. L. Brongersma, "Dielectric gradient metasurface optical elements," Science, vol. 345, pp. 298-302, 2014.

[148] X. Ni, S. Ishii, A. V. Kildishev, and V. M. Shalaev, "Ultra-thin, planar, Babinet-inverted plasmonic metalenses," Light Science & Applications, vol. 2, p. e72, 2013.

[149] C. Pfeiffer, N. K. Emani, A. M. Shaltout, A. Boltasseva, V. M. Shalaev, and A. Grbic, "Efficient Light Bending with Isotropic Metamaterial Huygens' Surfaces," Nano Letters, vol. 14, pp. 2491-2497, 2014.

[150] C. Pfeiffer and A. Grbic, "Controlling Vector Bessel Beams with Metasurfaces," Physical Review Applied, vol. 2, p. 044012, 2014.

[151] P. R. West, J. L. Stewart, A. V. Kildishev, V. M. Shalaev, V. V. Shkunov, F. Strohkendl, et al., "All-dielectric subwavelength metasurface focusing lens," Optics Express, vol. 22, pp. 26212-26221, 2014.

[152] R. Czaplicki, H. Husu, R. Siikanen, J. Mäkitalo, M. Kauranen, J. Laukkanen, et al., "Enhancement of Second-Harmonic Generation from Metal Nanoparticles by Passive Elements," Physical Review Letters, vol. 110, p. 093902, 2013.

[153] J. A. H. van Nieuwstadt, M. Sandtke, R. H. Harmsen, F. B. Segerink, J. C. Prangsma, S. Enoch, et al., "Strong Modification of the Nonlinear Optical Response of Metallic Subwavelength Hole Arrays," Physical Review Letters, vol. 97, p. 146102, 2006.

[154] G. Li, S. Chen, N. Pholchai, B. Reineke, P. W. H. Wong, E. Y. B. Pun, et al., "Continuous control of the nonlinearity phase for harmonic generations," Nat Mater, vol. 14, pp. 607-612, 2015.

[155] F. Monticone, N. M. Estakhri, and A. Alù, "Full Control of Nanoscale Optical Transmission with a Composite Metascreen," Physical Review Letters, vol. 110, p. 203903, 2013.

[156] C. Pfeiffer and A. Grbic, "Millimeter-Wave Transmitarrays for Wavefront and Polarization Control," IEEE Transactions on Microwave Theory and Techniques, vol. 61, pp. 4407-4417, 2013.

[157] C. Menzel, C. Rockstuhl, and F. Lederer, "Advanced Jones calculus for the classification of periodic metamaterials," Physical Review A, vol. 82, p. 053811, 2010.

[158] C. Lu and R. H. Lipson, "Interference lithography: a powerful tool for fabricating periodic structures," Laser & Photonics Reviews, vol. 4, pp. 568-580, 2010.

[159] W. Srituravanich, N. Fang, C. Sun, Q. Luo, and X. Zhang, "Plasmonic Nanolithography," Nano Letters, vol. 4, pp. 1085-1088, 2004.

[160] L. Pan, Y. Park, Y. Xiong, E. Ulin-Avila, Y. Wang, L. Zeng, et al., "Maskless Plasmonic Lithography at 22 nm Resolution," Scientific Reports, vol. 1, p. 175, 2011.

[161] X. Chen, F. Yang, C. Zhang, J. Zhou, and L. J. Guo, "Large-Area High Aspect Ratio Plasmonic Interference Lithography Utilizing a Single High-k Mode," ACS Nano, vol. 10, pp. 4039-4045, 2016.

[162] L. J. Guo, "Nanoimprint Lithography: Methods and Material Requirements," Advanced Materials, vol. 19, pp. 495-513, 2007.

[163] C. Zhang, S. Chen, T. Ling, and L. Jay Guo, "Review of Imprinted Polymer Microrings as Ultrasound Detectors: Design, Fabrication, and Characterization," Sensors Journal, IEEE, vol. 15, pp. 3241-3248, 2015.

[164] C. Zhang, H. Subbaraman, Q. Li, Z. Pan, J. G. Ok, T. Ling, et al., "Printed photonic elements: nanoimprinting and beyond," Journal of Materials Chemistry C, In press, 2016.

[165] C. Mack, "Introduction to Semiconductor Lithography," in Fundamental Principles of Optical Lithography, John Wiley & Sons, Ltd, 2007.

[166] M. Totzeck, W. Ulrich, A. Gohnermeier, and W. Kaiser, "Semiconductor fabrication: Pushing deep ultraviolet lithography to its limits," Nature Photonics, vol. 1, pp. 629-631, 2007.

[167] B. Wu and A. Kumar, "Extreme ultraviolet lithography: A review," Journal of Vacuum Science & Technology B, vol. 25, pp. 1743-1761, 2007.

[168] M. C. Peckerar and J. R. Maldonado, "X-ray lithography-an overview," Proceedings of the IEEE, vol. 81, pp. 1249-1274, 1993.

[169] X. Chen, F. Yang, C. Zhang, J. Zhou, and L. J. Guo, "Large-Area High Aspect Ratio Plasmonic Interference Lithography Utilizing a Single High-k Mode," ACS Nano, vol. 10, pp. 4039-4045, 2016.

[170] Y. Chen, "Nanofabrication by electron beam lithography and its applications: A review," Microelectronic Engineering, vol. 135, pp. 57-72, 2015.

[171] M. Altissimo, "E-beam lithography for micro-/nanofabrication," Biomicrofluidics, vol. 4, p. 026503, 2010.

[172] K. Arshak, M. Mihov, A. Arshak, D. McDonagh, and D. Sutton, "Focused ion beam lithography-overview and new approaches," in Microelectronics, 2004. 24th International Conference on, vol.2, pp. 459-462, 2004,.

[173] S. Alom Ruiz and C. S. Chen, "Microcontact printing: A tool to pattern," Soft Matter, vol. 3, pp. 168-177, 2007.

[174] A. Perl, D. N. Reinhoudt, and J. Huskens, "Microcontact Printing: Limitations and Achievements," Advanced Materials, vol. 21, pp. 2257-2268, 2009.

[175] M. Deubel, G. von Freymann, M. Wegener, S. Pereira, K. Busch, and C. M. Soukoulis, "Direct laser writing of three-dimensional photonic-crystal templates for telecommunications," Nature Materials, vol. 3, pp. 444-447, 2004.

[176] K. Salaita, Y. Wang, and C. A. Mirkin, "Applications of dip-pen nanolithography," Nature Nanotechnology, vol. 2, pp. 145-155, 2007.

[177] R. D. Piner, J. Zhu, F. Xu, S. Hong, and C. A. Mirkin, ""Dip-Pen" Nanolithography," Science, vol. 283, pp. 661-663, 1999.

[178] R. Garcia, A. W. Knoll, and E. Riedo, "Advanced scanning probe lithography," Nature Nanotechnology, vol. 9, pp. 577-587, 2014.

[179] G. A. Ozin, K. Hou, B. V. Lotsch, L. Cademartiri, D. P. Puzzo, F. Scotognella, et al., "Nanofabrication by self-assembly," Materials Today, vol. 12, pp. 12-23, 2009.

[180] C. A. Ross, K. K. Berggren, J. Y. Cheng, Y. S. Jung, and J.-B. Chang, "Three-Dimensional Nanofabrication by Block Copolymer Self-Assembly," Advanced Materials, vol. 26, pp. 4386-4396, 2014.

[181] S. Y. Chou, P. R. Krauss, and P. J. Renstrom, "Imprint of sub-25 nm vias and trenches in polymers," Applied Physics Letters, vol. 67, pp. 3114-3116, 1995.

[182] S. Y. Chou, P. R. Krauss, and P. J. Renstrom, "Imprint Lithography with 25-Nanometer Resolution," Science, vol. 272, pp. 85-87, 1996.

[183] F. Susumu, "Fine Pattern Fabrication by the Molded Mask Method (Nanoimprint Lithography) in the 1970s," Japanese Journal of Applied Physics, vol. 48, p. 06FH01, 2009.

[184] H.-C. Wang, S. Fleming, Y.-C. Lee, M. Swain, S. Law, and J. Xue, "Laser ultrasonic evaluation of human dental enamel during remineralization treatment," Biomedical Optics Express, vol. 2, pp. 345-355, 2011.

[185] O. Balogun, R. Huber, D. Chinn, and J. B. Spicer, "Laser ultrasonic inspection of the microstructural state of thin metal foils," The Journal of the Acoustical Society of America, vol. 125, pp. 1437-1443, 2009.

[186] K. Sridhar, "Theory and Applications of Laser-Ultrasonic Techniques," in Ultrasonic Nondestructive Evaluation, CRC Press, 2003.

[187] M. Xu and L. V. Wang, "Photoacoustic imaging in biomedicine," Review of Scientific Instruments, vol. 77, p. 041101, 2006.

[188] L. V. Wang and S. Hu, "Photoacoustic Tomography: In Vivo Imaging from Organelles to Organs," Science, vol. 335, pp. 1458-1462, 2012.

[189] S.-L. Chen, Y.-C. Chang, C. Zhang, J. G. Ok, T. Ling, M. T. Mihnev, et al., "Efficient real-time detection of terahertz pulse radiation based on photoacoustic conversion by carbon nanotube nanocomposite," Nature Photonics, vol. 8, p. 537–542, 2014.

[190] V. E. Gusev and A. A. Karabutov, Laser optoacoustics. New York: American Institute of Physics, 1993.

[191] S.-L. Chen, H. Sheng-Wen, L. Tao, S. Ashkenazi, and L. J. Guo, "Polymer microring resonators for high-sensitivity and wideband photoacoustic imaging," Ultrasonics, Ferroelectrics and Frequency Control, IEEE Transactions on, vol. 56, pp. 2482-2491, 2009.

[192] L. Xiang, B. Wang, L. Ji, and H. Jiang, "4-D Photoacoustic Tomography," Scientific Reports, vol. 3, p. 1113, 2013.

[193] Eric M. Strohm, E. S. L. Berndl, and Michael C. Kolios, "Probing Red Blood Cell Morphology Using High-Frequency Photoacoustics," Biophysical journal, vol. 105, pp. 59-67, 2013.

[194] G. Xu, Z.-X. Meng, J. D. Lin, J. Yuan, P. L. Carson, B. Joshi, et al., "The Functional Pitch of an Organ: Quantification of Tissue Texture with Photoacoustic Spectrum Analysis," Radiology, vol. 271, p. 130777, 2014

[195] K. Maslov, H. F. Zhang, S. Hu, and L. V. Wang, "Optical-resolution photoacoustic microscopy for in vivo imaging of single capillaries," Optics Letters, vol. 33, pp. 929-931, 2008.

[196] C. Zhang, K. Maslov, S. Hu, R. Chen, Q. Zhou, K. K. Shung, et al., "Reflection-mode submicron-resolution in vivo photoacoustic microscopy," Journal of Biomedical Optics, vol. 17, pp. 0205011-0205014, 2012.

[197] C. Zhang, K. Maslov, and L. V. Wang, "Subwavelength-resolution label-free photoacoustic microscopy of optical absorption in vivo," Optics Letters, vol. 35, pp. 3195-3197, 2010.

[198] Z. Xie, S. Jiao, H. F. Zhang, and C. A. Puliafito, "Laser-scanning optical-resolution photoacoustic microscopy," Optics Letters, vol. 34, pp. 1771-1773, 2009.

[199] L. Wang, K. Maslov, J. Yao, B. Rao, and L. V. Wang, "Fast voice-coil scanning optical-resolution photoacoustic microscopy," Optics Letters, vol. 36, pp. 139-141, 2011.

[200] W. Yu, K. Maslov, K. Chulhong, H. Song, and L. V. Wang, "Integrated Photoacoustic and Fluorescence Confocal Microscopy," Biomedical Engineering, IEEE Transactions on, vol. 57, pp. 2576-2578, 2010.

[201] C. Zhang, K. Maslov, J. Yao, and L. V. Wang, "In vivo photoacoustic microscopy with 7.6-μm axial resolution using a commercial 125-MHz ultrasonic transducer," Journal of Biomedical Optics, vol. 17, p. 116016, 2012.

[202] J. W. Hunt, M. Arditi, and F. S. Foster, "Ultrasound Transducers for Pulse-Echo Medical Imaging," Biomedical Engineering, IEEE Transactions on, vol. BME-30, pp. 453-481, 1983.

[203] R. E. Davidsen and S. W. Smith, "Two-dimensional arrays for medical ultrasound using multilayer flexible circuit interconnection," Ultrasonics, Ferroelectrics and Frequency Control, IEEE Transactions on, vol. 45, pp. 338-348, 1998.

[204] F. S. Foster, K. A. Harasiewicz, and M. D. Sherar, "A history of medical and biological imaging with polyvinylidene fluoride (PVDF) transducers," Ultrasonics, Ferroelectrics and Frequency Control, IEEE Transactions on, vol. 47, pp. 1363-1371, 2000.

[205] A. A. Oraevsky and A. A. Karabutov, "Ultimate sensitivity of time-resolved optoacoustic detection," Proc. SPIE 3916, Biomedical Optoacoustics, pp. 228-239, 2000.

[206] X. Minghua, X. Yuan, and L. V. Wang, "Time-domain reconstruction algorithms and numerical simulations for thermoacoustic tomography in various geometries," Biomedical Engineering, IEEE Transactions on, vol. 50, pp. 1086-1099, 2003.

[207] K. Geng, W. Xueding, S. George, and V. W. Lihong, "Multiple-bandwidth photoacoustic tomography," Physics in Medicine and Biology, vol. 49, p. 1329, 2004.

[208] J. Gateau, A. Chekkoury, and V. Ntziachristos, "Ultra-wideband three-dimensional optoacoustic tomography," Optics Letters, vol. 38, pp. 4671-4674, 2013.

[209] C. Zhang, Y. Zhou, C. Li, and L. V. Wang, "Slow-sound photoacoustic microscopy," Applied Physics Letters, vol. 102, p. 163702, 2013.

[210] E. Zhang, J. Laufer, and P. Beard, "Backward-mode multiwavelength photoacoustic scanner using a planar Fabry-Perot polymer film ultrasound sensor for high-resolution three-dimensional imaging of biological tissues," Applied Optics, vol. 47, pp. 561-577, 2008.

[211] E. Zhang and P. Beard, "Broadband ultrasound field mapping system using a wavelength tuned, optically scanned focused laser beam to address a Fabry Perot polymer film sensor," Ultrasonics, Ferroelectrics and Frequency Control, IEEE Transactions on, vol. 53, pp. 1330-1338, 2006.

[212] P. Hajireza, K. Krause, M. Brett, and R. Zemp, "Glancing angle deposited nanostructured film Fabry-Perot etalons for optical detection of ultrasound," Optics Express, vol. 21, pp. 6391-6400, 2013.

[213] R. L. Shelton and B. E. Applegate, "Ultrahigh resolution photoacoustic microscopy via transient absorption," Biomedical Optics Express, vol. 1, pp. 676-686, 2010.

[214] T. Ling, S.-L. Chen, and L. J. Guo, "High-sensitivity and wide-directivity ultrasound detection using high Q polymer microring resonators," Applied Physics Letters, vol. 98, p. 204103, 2011.

[215] S.-W. Huang, S.-L. Chen, T. Ling, A. Maxwell, M. O'Donnell, L. J. Guo, et al., "Low-noise wideband ultrasound detection using polymer microring resonators," Applied Physics Letters, vol. 92, p. 193509, 2008.

[216] G. J. Diebold, T. Sun, and M. I. Khan, "Photoacoustic monopole radiation in one, two, and three dimensions," Physical Review Letters, vol. 67, pp. 3384-3387, 1991.

[217] Z. Xie, C. Tian, S.-L. Chen, T. Ling, C. Zhang, L. J. Guo, et al., "3D high resolution photoacoustic imaging based on pure optical photoacoustic microscopy with microring resonator," Proc. SPIE 8943, Photons Plus Ultrasound: Imaging and Sensing, p. 894314, 2014.

[218] D. K. Armani, T. J. Kippenberg, S. M. Spillane, and K. J. Vahala, "Ultra-high-Q toroid microcavity on a chip," Nature, vol. 421, pp. 925-928, 2003.

[219] P. C. Beard, F. Perennes, and T. N. Mills, "Transduction mechanisms of the Fabry-Perot polymer film sensing concept for wideband ultrasound detection," Ultrasonics, Ferroelectrics and Frequency Control, IEEE Transactions on, vol. 46, pp. 1575-1582, 1999.

[220] M. Sinha and D. Buckley, "Acoustic Properties of Polymers," in Physical Properties of Polymers Handbook, J. Mark, Ed., Springer New York, 2007.

[221] J. Brandrup, E. H. Immergut, E. A. Grulke, A. Abe, and D. R. Bloch, "Polymer Handbook (4th Edition)," John Wiley & Sons, 2003.

[222] S.-L. Chen, T. Ling, and L. J. Guo, "Low-noise small-size microring ultrasonic detectors for high-resolution photoacoustic imaging," Journal of Biomedical Optics, vol. 16, p. 056001, 2011.

[223] S.-L. Chen, Y.-C. Chang, C. Zhang, J. G. Ok, T. Ling, M. T. Mihnev, et al., "Efficient real-time detection of terahertz pulse radiation based on photoacoustic conversion by carbon nanotube nanocomposite," Nature Photonics, vol. 8, p. 537, 2014.

[224] S.-L. Chen, C. Zhang, Y.-C. Chang, J. G. Ok, T. Ling, M. T. Mihnev, et al., "Efficient Real-time Detection of Terahertz Pulse Radiation by ?Listening to? Photoacoustic Generation," in Frontiers in Optics, Tucson, Arizona, 2014.

[225] C. Winnewisser, P. U. Jepsen, M. Schall, V. Schyja, and H. Helm, "Electro-optic detection of THz radiation in LiTaO3, LiNbO3 and ZnTe," Applied Physics Letters, vol. 70, pp. 3069-3071, 1997.

[226] H. Shi, J. G. Ok, H. Won Baac, and L. Jay Guo, "Low density carbon nanotube forest as an index-matched and near perfect absorption coating," Applied Physics Letters, vol. 99, p. 211103, 2011.

[227] H. Won Baac, J. G. Ok, H. J. Park, T. Ling, S.-L. Chen, A. J. Hart, et al., "Carbon nanotube composite optoacoustic transmitters for strong and high frequency ultrasound generation," Applied Physics Letters, vol. 97, p. 234104, 2010.

[228] H. W. Baac, J. G. Ok, A. Maxwell, K.-T. Lee, Y.-C. Chen, A. J. Hart, et al., "Carbon-Nanotube Optoacoustic Lens for Focused Ultrasound Generation and High-Precision Targeted Therapy," Scientific Reports, vol. 2, p. 989, 2013.

[229] K. Jansen, G. van Soest, and A. F. W. van der Steen, "Intravascular Photoacoustic Imaging: A New Tool for Vulnerable Plaque Identification," Ultrasound in Medicine & Biology, vol. 40, pp. 1037-1048, 2014.

[230] P. Wang, T. Ma, M. N. Slipchenko, S. Liang, J. Hui, K. K. Shung, et al., "High-speed Intravascular Photoacoustic Imaging of Lipid-laden Atherosclerotic Plaque Enabled by a 2-kHz Barium Nitrite Raman Laser," Scientific Reports, vol. 4, p. 6889, 2014.

[231] C. J. Chang-Hasnain and W. Yang, "High-contrast gratings for integrated optoelectronics," Advances in Optics and Photonics, vol. 4, pp. 379-440, 2012.

[232] B. E. A. Saleh and T. Malvin Carl, Fundamentals of photonics: Wiley-interscience, 2007.